QUANTUM FLUCTUATIONS IN SMALL LASERS

by

Kaushik Roy Choudhury

A Dissertation Presented to the
FACULTY OF THE GRADUATE SCHOOL
UNIVERSITY OF SOUTHERN CALIFORNIA
In Partial Fulfillment of the
Requirements for the Degree
DOCTOR OF PHILOSOPHY
(PHYSICS)

August 2011

Dedication

I dedicate this thesis to my family and closest friends. My work would not be possible without their support.

Acknowlegements

I am grateful to my advisor Professor Anthony F. J. Levi for guiding me through these years of my PhD. I would like to thank him for his guidance, patience, support and encouragement during the course of my graduate studies at USC. This dissertation could not have been completed without his help.

I would like to thank Professor Stephan Haas for his help during the years of my graduate study at USC.

Apart from my advisor, I would like to thank the members of my guidance committee Stephan Haas, Paolo Zanardi, Moh. El Naggar and Chunming Wang for their helpful comments. I would like to thank Professor Aiichiro Nakano for helpful discussions regarding computing in HPC.

Through the years of my PhD, it has been my pleasure to have insightful discussions with fellow graduate students. For this, I thank Neelakshi Hudda, Ramakrishnan Iyer, Arnab Kundu, Aditya Raghavan, Kelly Macgruder and Philip Seliger.

Finally, I would like to express immense gratitude and love to my father and mother for their understanding and support.

Table of Contents

List of Figures

Abstract

Quantum fluctuations play a critical role in determining the steady-state and transient response of a laser. Such fluctuations can dominate behavior when there is a small number of particles in the system. Correlations between n discrete excited electronic states and s discrete photons can create non-Poisson probability distributions and damp the average dynamic response of laser emission. In this thesis a quantum mechanical treatment of fluctuations and saturable absorption in meso-scale lasers is presented. Time evolution of the density matrix is obtained from numerical integration and field-field and intensity-intensity correlations are calculated to obtain steady-state line width and photon statistics. Inclusion of a saturable absorber in the otherwise homogeneous medium is shown to suppress lasing, increase fluctuations, and enhance spontaneous emission near threshold. Methods to connect between quantum, meso-scale and classical systems is also developed.

Chapter 1

Introduction- review of semi-classical laser theory

1.1 Introduction

Coherent electromagnetic radiation in the microwave range was first observed in ammonia in 1954 by Gordon, Zieger and Townes [Ref.[1]]. The idea to extend the concept to optical frequencies was suggested by Schawlow and Townes [Ref.[2]], creating a device called the laser (light amplification by stimulated emission of radiation). The laser essentially consists of an ensemble of excited atoms interacting with electromagnetic radiation inside a low-loss optical cavity. Only certain distinct frequencies of electromagnetic radiation attain appreciable intensity inside the optical cavity. The active atoms are in resonance with one of these cavity modes. An inverted medium converts energy to the optical field whose intensity can increase greatly. The optical field stimulates transitions in the form of stimulated emission which leads to lasing light. Maiman demonstrated the first pulsed laser operation in Ruby [Ref.[3]] and the first continuous wave operation of a He-Ne gas laser was achieved by Javan [Ref.[4]]. Since then, other systems capable of lasing have been developed. An important example is the semiconductor laser, where the inverted medium is created by electrons in the conduction band and holes in the valence band. Transitions between these states can produce lasing photons. Semiconductor laser diodes are employed in diverse and important applications.

They are used in fiber-optic communication systems for the internet, they are essential for all optical storage, and they enable high-quality low-cost printing.

Widespread use of laser requires low threshold pump powers and high efficiency. The issue of low threshold can be addressed in part by reducing device size. An important advancement was made in this field by developing high-Q optical cavities following an idea by Purcell [Ref. [5]]. He showed that the spontaneous emission rate of a medium can be enhanced by coupling it to the resonant mode of an electromagnetic cavity. The reverse is also true, when the medium is out of resonance. This is called the cavity QED effect in which the radiative property of a medium is strongly influenced by its surrounding environment. Enhancement of spontaneous emission was experimentally demonstrated by Drexhage in dye atoms [Ref. [6]]. In the case of a laser, the total spontaneous emission of the inverted medium is divided amongst the lasing mode and non-lasing mode by fraction β and $(1-\beta)$ respectively. Inhibiting emission into optical modes other than the lasing mode lowers lasing threshold. The cavity QED effect can also be utilised to achieve this criteria. Minimizing device sizes was accompanied by development of high-Q microcavities such as microdisk, microsphere, photonic crystal cavities which can lead to lasers with high β values [Ref. [7]]. Creating devices of smaller dimension is a subject of both practical and theoretical interest. Smaller devices may cost less. These systems may also show new physical effects, different from a bulk medium. The ultimate microscopic limit is the idea of single atom lasers or masers. The gain medium in this case consists effectively of a single atom. Coupled to high Q superconducting cavities, micromasers can be used for studying fundamental atom-field interactions. Purely quantum mechanical effects like squeezing, production of number states and trapped states are observed in micromasers. These model systems have been experimentally realised [Ref. [8, 9]].

Lasing is a specific example among a rich variety of phenomena associated with light-matter interaction. Other interesting phenomena include bistability, resonance fluorescence, inelastic light scattering, etc.. Theoretical treatments of light-matter interactions have led to the development of several theories, treating the system under different approximations. The semi-classical theory of lasers developed by Lamb [Ref.[10]] uses Maxwell-Schrödinger equations. It treats the atoms quantum mechanically and light classically. This essentially led to continnum mean-field rate equation theories used widely in the study of large systems. Description of the role of inherent quantum mechanical processes such as spontaneous emission in lasing required extension of these models to a more complete quantum description. Pioneering work in this area was done by Lax [Ref.[11]], H. Haken [Ref.[12]] and Scully and Lamb [Ref.[13, 14]]. The quantum theories carry information about particle and phase fluctuations, which are absent in the continnum mean-field description. For example the Poisson distribution of coherent light far above threshold and the Schawlow-Townes formula for line-width was verified by these theories.

The solution to the full quantum theory is either obtained under approximations of large systems or in the case of a single atom. General solution under any operating condition is difficult. For large systems with small fluctuations, the equations reduce to the standard Fokker-Plank equations which is solvable [Ref.[15, 16]]. Hence, the approximations under which these equations are solved somehow restricts them from explaining the behavior of meso-scale systems which involves a few particles. An attempt towards an exact solution was made in the maser case by Elk [Ref. [17]]. Other general treatments of N emitters requires further approximations which influences the final conclusions [Ref. [18]]. In this work we have tried to address this intermediate regime of operation, by developing different theoretical models. We have made an attempt to computationally solve these problems in a way which is not constrained by the approximations

required for analytical techniques. This work provides a brief review of standard laser theories and developments of new techniques required for treating meso-scale lasers. A clear comparison can be made as the equations are solved without the general approximations used in laser theories. The techniques developed follow the density matrix treatment of Scully and Lamb [Ref.[13, 14]]. An alternate approach using operators in the Hiesenberg picture [Ref.[11, 15]] is not considered in the current work.

The work in this thesis is organized as follows. The semi-classical theory of laser developed by Lamb is reviewed in this chapter following the work of Scully and Zubairy [Ref. [15]]. The atom-field interaction Hamiltonian is derived which is used extensively in the later chapters. All the approximations made in the process of obtaining the laser rate equations are explicitly considered. The conclusions and the limitations of the semi-classical model is discussed. The rate equations for the atomic gain medium is modified to explain the behavior of the semiconductor gain medium in Chapter 2. The semi-classical nature of the model remains valid. However, discrete levels are now replaced by band structure, which effectively modifies the rates appearing in the rate equations. Differences between the semiconductor and atomic theory is reviewed [Ref. [24]]. Numerical simulation of these rate equations are performed to explain the static and dynamic characteristics of semiconductor lasers. A discussion of noise processes and fluctuations is included to illustrate the limitations of the semi-classical rate equation treatment in explaining fluctuation-driven phenomena in lasers. Chapters 3 introduces the semi-classical master equations, which are solved numerically to explain the properties of meso-scale lasers. Both steady-state and transient behavior in the meso-scale are studied and compared with the results obtained using rate equations. Particular choices of parameters produce strong bi-stable behavior around threshold in these meso-scale systems leading to novel effects like lasing suppression, carrier de-pinning and bimodal distributions. This contradicts the usual threshold properties of large lasers

predicted using rate equations. The difference is explained by accounting for the underlying difference between the probabilistic and mean-field continuum rate equation models. Chapter 4 reviews the quantum theory of atom-field interaction following the work of Scully and Zubairy [Ref. [15]]. The Jaynes-Cummings Hamiltonian, which is the starting point of most problems in quantum optics is derived. The idea of open quantum systems is introduced with a discussion on reservoirs. A brief review of the quantum theory of the laser is given and a comparison is made with the semi-classical predictions. This review allows us to critically analyze the approximations which break down in the meso-scale limit of a few emitters. Chapter 5 discusses the full quantum theory of meso-lasers using a density matrix treatment. Comparisons are made with the semi-classical predictions of Chapter 3 and the novel predictions of lasing suppression and carrier de-pinning are recovered by adding a saturable absorber. The physical meaning of the parameter β, which is solely responsible for producing these new effects in the semi-classical theory, is realized using the full quantum theory. A summary of the current work is presented in Chapter 6 along with discussions on future applications of the developed theory.

As mentioned above, we present a brief review of the semi-classical theory of laser in this chapter, which happens to be one of the earliest theories for explaining behavior of lasers. This theory treats the emitters or atoms as quantum mechanical systems and light as a classical field. From a quantum mechanical perspective, a classical field is an approximation for large photon numbers. Surprisingly, the semi-classical theory valid for large systems is able to theoretically explain the behavior of most small lasers realized experimentally to date [Ref. [7, 40, 49]]. This fact alone makes a discussion of this theory necessary as one needs to clearly understand the reasons for its validity in

these small systems. We start with the derivation of the Hamiltonian for this emitter-field system which is used extensively as a starting point in our work. The mathematical notations are similar to the work of Scully and Zubiary [Ref. [15]].

1.2 Dipole approximation and r.E Hamiltonian

The Hamiltonian describing the interaction of an electron with an electromagnetic field is given by,

$$H = \frac{1}{2m}[\mathbf{p} - e\mathbf{A}(\mathbf{r},t)]^2 + eU(\mathbf{r},t) + V(r) \tag{1.2.1}$$

where e and m denotes the charge and mass of the electron respectively. $\mathbf{p}$ is the canonical momentum. $\mathbf{A}$ and U are the vector and scalar potentials describing the electromagnetic field. $V(r)$ is the potential describing the interaction of the electron and nucleus (located at $\mathbf{r_0}$). The dipole approximation, ignores the variation of the electromagnetic field over the size of the atom. Hence the vector potential can be expanded in the limit, $\mathbf{k}.\mathbf{r} \ll 1$, as

$$\mathbf{A}(\mathbf{r}_0 + \mathbf{r}, t) = \mathbf{A}(t)\exp[i\mathbf{k}.(\mathbf{r}_0 + \mathbf{r})]$$
$$= \mathbf{A}(t)\exp(i\mathbf{k}.\mathbf{r}_0)(1 + i\mathbf{k}.\mathbf{r} + ..) = A(t)\exp(i\mathbf{k}.\mathbf{r}_0) = \mathbf{A}(\mathbf{r}_0, t) \tag{1.2.2}$$

The Schrödinger equation for this problem is,

$$[-\frac{\hbar^2}{2m}[\nabla - \frac{ie}{\hbar}\mathbf{A}(\mathbf{r}_0,t)]^2 + V(r)]\psi(r,t) = i\hbar\frac{\partial\psi(\mathbf{r},t)}{\partial t} \tag{1.2.3}$$

$U(\mathbf{r},t)$ = 0 and $\nabla.\mathbf{A}$ = 0, in the radiation gauge. Using these properties and by defining a new wave function $\phi(\mathbf{r},t)$

$$\psi(\mathbf{r},t) = \exp[\frac{ie}{\hbar}\mathbf{A}(\mathbf{r}_0,t).\mathbf{r}]\phi(\mathbf{r},t) \tag{1.2.4}$$

Eq.(1.2.3) is simplified to give,

$$i\hbar\dot{\phi}(\mathbf{r},t) = [H_0 - e\mathbf{r}.\mathbf{E}(\mathbf{r}_0,t)]\phi(\mathbf{r},t) \tag{1.2.5}$$

where

$$H_0 = [\frac{p^2}{2m} + V(r)] \tag{1.2.6}$$

is the unperturbed Hamiltonian of the electron and nucleus. The expression, $\mathbf{E} = -\dot{\mathbf{A}}$ is used to write the equation in terms of the gauge independent field $\mathbf{E}$. The new wave function $\phi(\mathbf{r},t)$ differs by a phase factor which does not modify the final results.
The total Hamiltonian is

$$H = H_0 + H_1 \tag{1.2.7}$$

with

$$H_1 = -e\mathbf{r}.\mathbf{E}(\mathbf{r}_0,t) \tag{1.2.8}$$

We shall use this Hamiltonian in our subsequent studies. Solution to this problem for a two-level atom shows Rabi oscillations involving periodic energy transfer between

atom and field. In this case, in terms of the states $|a\rangle$ and $|b\rangle$, for a two-level atom, the Hamiltonian (Eq.(1.2.7)) reduces to

$$\begin{aligned} H_0 &= \hbar\omega_a |a\rangle \langle a| + \hbar\omega_b |b\rangle \langle b| \\ H_1 &= -exE(t) = -(\mathcal{P}_{ab} |a\rangle \langle b| + \mathcal{P}_{ba} |b\rangle |a\rangle)E(t) \end{aligned} \tag{1.2.9}$$

where $\mathcal{P}_{ab} = \mathcal{P}^*_{ba} = e \langle a| x |b\rangle$ is the matrix element of the electric dipole moment. The completeness relation $|a\rangle \langle a| + |b\rangle \langle b| = 1$ is used in the above derivation.

1.3 Density matrix

In general, a state vector $|\psi\rangle$ contains all information about a system. The expectation value of any operator O is given by

$$\langle O \rangle_{QM} = \langle \psi| O |\psi\rangle \tag{1.3.1}$$

In many situations however, exact knowledge of $|\psi\rangle$ may be missing; only the probability $P_{|\psi\rangle}$, that the system is in state $|\psi\rangle$ is known. Calculation of expectation value of any operator O in such situations require not only quantum mechanical averaging but also statistical averaging over similarly prepared identical systems. Thus we have

$$\left\langle \langle O \rangle_{QM} \right\rangle_{ensemble} = Tr(O\rho) \tag{1.3.2}$$

where ρ is the density operator, defined by

$$\rho = \sum_{\psi} P_\psi |\psi\rangle \langle \psi| \tag{1.3.3}$$

From the properties of trace we have,

$$Tr(O\rho) = Tr(\rho O) \tag{1.3.4}$$

For the case of a pure state, all P_ψ are zero except the one for a state $|\psi_0\rangle$ and we have

$$\rho = |\psi_0\rangle \langle\psi_0| \tag{1.3.5}$$

From the conservation of probability $Tr(\rho) = 1$. Also, for a pure state, $Tr(\rho^2) = 1$. The equation of motion of the density matrix can be obtained using the Schrödinger equation

$$\left|\dot{\psi}\right\rangle = -\frac{i}{\hbar} H |\psi\rangle \tag{1.3.6}$$

The time derivative of ρ (Eq.(1.3.3)) gives

$$\dot{\rho} = \sum_\psi P_\psi (|\dot{\psi}\rangle \langle\psi| + |\psi\rangle \langle\dot{\psi}| \tag{1.3.7}$$

where P_ψ is time independent. Eq.(1.3.6) is used to replace $\left|\dot{\psi}\right\rangle$ and $\left\langle\dot{\psi}\right|$ and we get

$$\dot{\rho} = -\frac{i}{\hbar}[H, \rho] \tag{1.3.8}$$

Eq.(1.3.8) is called the Liouville or Von Neumann equation of motion of the density matrix. This equation gives statistical as well as quantum mechanical information.

The finite lifetime of the atomic levels due to excited-state decay can be included by adding phenomenological decay terms to the density operator equation. This is done by adding by relaxation matrix Γ, defined as

$$\langle n| \Gamma |m\rangle = \gamma_n \delta_{nm} \tag{1.3.9}$$

The density matrix equation now becomes

$$\begin{aligned} \dot{\rho} &= -\frac{i}{\hbar}[\mathcal{H}, \rho] - \frac{1}{2}(\Gamma, \rho) \\ (\Gamma, \rho) &= \Gamma\rho + \rho\Gamma. \end{aligned} \tag{1.3.10}$$

For the case of the two-level atom, the state of the system $|\psi\rangle$ can be written as $|\psi\rangle = C_a |a\rangle + C_b |b\rangle$. The density matrix operator written in terms of states $|a\rangle$ and $|b\rangle$ is,

$$\begin{aligned} \rho = |\psi\rangle \langle\psi| = [C_a |a\rangle + C_b |b\rangle][C_a^* \langle a| + C_b^* \langle b|] \\ = |C_a|^2 |a\rangle \langle a| + C_a C_b^* |a\rangle \langle b| + C_b C_a^* |b\rangle \langle a| + |C_b|^2 |b\rangle \langle b| \end{aligned} \tag{1.3.11}$$

where the matrix elements for the operator is,

$$\begin{aligned} \rho_{aa} &= \langle a| \rho |a\rangle = |C_a(t)|^2 \\ \rho_{ab} &= \langle a| \rho |b\rangle = C_a(t) C_b^*(t) \\ \rho_{ba} &= \rho_{ab}^* \\ \rho_{bb} &= \langle b| \rho |b\rangle = |C_b(t)|^2 \end{aligned} \tag{1.3.12}$$

ρ_{aa} and ρ_{bb} are the occupation probabilities for state $|a\rangle$ and $|b\rangle$ respectively. The off-diagonal elements are related to the definition of atomic polarization for an atom.

$$P(z,t) = \langle\psi| er |\psi\rangle = C_a C_b^* \mathcal{P}_{ba} + C_a^* C_b \mathcal{P}_{ab} = \rho_{ab}\mathcal{P}_{ba} + \rho_{ba}\mathcal{P}_{ab} \tag{1.3.13}$$

where $\mathcal{P}_{ba} = \langle b| er |a\rangle$ is the matrix element of the electric dipole moment. The semi-classical problem of a two-level atom interacting with a electromagnetic field can be described using the density matrix. Using the Hamiltonian given by Eq.(1.2.9), the equations of motion for the density matrix elements of the atom can be determined. The equations are

$$\dot{\rho}_{aa} = -\gamma_a \rho_{aa} + \frac{i}{\hbar}[\mathcal{P}_{ab} E \rho_{ba} - \mathcal{P}_{ba} E \rho_{ab}] \tag{1.3.14}$$

$$\dot{\rho}_{bb} = -\gamma_b \rho_{bb} - \frac{i}{\hbar}[\mathcal{P}_{ab} E \rho_{ba} - \mathcal{P}_{ba} E \rho_{ab}] \tag{1.3.15}$$

$$\dot{\rho}_{ab} = -(i\omega + \gamma_{ab})\rho_{ab} - \frac{i}{\hbar}\mathcal{P}_{ab} E[\rho_{aa} - \rho_{bb}] \tag{1.3.16}$$

where $\gamma_{ab} = (\gamma_a + \gamma_b)/2$ with γ_a and γ_b defined by Eq.(1.3.9) and $E(t) = Ecos(\nu t)$.

1.4 Maxwell-Schrödinger equations

1.4.1 Population matrix for the atoms

The problem of a single atom interacting with a single cavity mode can be extended to realistic systems like lasers where multiple atoms are interacting with the field. Self-consistent solution to equations describing matter and field is required in describing these more complicated systems. In a semi-classical picture, this problem can be solved in the following way. The classical field induces dipole-moments in the atoms of the medium which are treated quantum mechanically. The density matrix is required to perform statistical summations over the atoms, in order to obtain macroscopic polarization from the individual dipole moments. This induced polarization in turn drives the electromagnetic field. Such a procedure makes the formalism self-consistent.
The density operator for individual atoms in terms of its basis states ($|a\rangle$, $|b\rangle$) is given by (Eq.(1.3.12))

$$\rho(z,t,t_i) = \sum_{\alpha,\beta} \rho_{\alpha\beta}(z,t,t_i)\,|\alpha\rangle\,\langle\beta| \tag{1.4.1}$$

where $\alpha,\beta = a,b$. The coordinate z, denotes the position of an atom at time t. t_i denotes the injection time of the i^{th} atom and is random by nature. At time t_i,

$$\begin{aligned} \rho(z,t_i,t_i) &= \sum_{\alpha,\beta} \rho^{(0)}_{\alpha\beta}\,|\alpha\rangle\,\langle\beta| \\ \rho_{\alpha\beta}(z,t_i,t_i) &= \rho^{(0)}_{\alpha\beta} \end{aligned} \tag{1.4.2}$$

The atoms are pumped into the cavity at rate $r_a(z,t_0)$ per second per unit volume. Macroscopic polarization of the medium is obtained by averaging over all atoms. A population matrix is defined at this point to perform the averaging. The population

matrix acts as a density operator for the medium and describes its average behavior. This is given by,

$$\rho(z,t) = \int_{-\infty}^{t} dt_i r_a(z,t_i)\rho(z,t,t_i)$$
$$= \sum_{\alpha,\beta} \int_{-\infty}^{t} dt_i r_a(z,t_i)\rho_{\alpha\beta}(z,t,t_i)\left|\alpha\right\rangle\left\langle\beta\right| \tag{1.4.3}$$

where the effect of the individual atoms are included by averaging over the inital times. The slow variation of the pump, $r_a(z,t_0)$ can be ignored. Macroscopic polarization of the medium, $P(z,t)$ is obtained by adding the effect of all atoms at z at time t,

$$\begin{aligned} P(z,t) &= \int_{-\infty}^{t} dt_0 r_a(z,t_i) Tr[\hat{\mathcal{P}}\rho(z,t,t_i)] \\ &= \sum_{\alpha,\beta} \int_{-\infty}^{t} dt_0 r_a(z,t_i)\rho_{\alpha\beta}(z,t,t_i)\mathcal{P}_{\beta\alpha} \end{aligned} \tag{1.4.4}$$

where $\hat{\mathcal{P}}$ is the dipole moment operator. The expression of $\rho(z,t,t_i)$ from Eq.(1.4.1) is used for performing the trace. Only the off-diagonal terms exist after the summation due to parity of the states. Integration over the initial time, t_i in Eq.(1.4.5) effectively averages over all atoms. For a two-level atom, with $\mathcal{P}_{ab} = \mathcal{P}_{ba} = \mathcal{P}$, we obtain

$$P(z,t) = \mathcal{P}[\rho_{ab}(z,t) + \rho_{ba}(z,t)] \tag{1.4.5}$$

Similar to the off-diagonal elements of single atoms (Eq.(1.3.13)), the off-diagonal terms of the population matrix determine macroscopic polarization.

As stated at the begining of this section, interaction with an electromagnetic field induces polarization in the medium. The equation of motion of the population matrix of the medium, $\rho(z,t)$ interacting with the electromagnetic field is obtained using equations of individual atoms, Eqns.(1.3.14-1.3.16). The atoms are initially incoherently

pumped to levels $|a\rangle$ and $|b\rangle$ at constant rate r_a. This sets the initial off-diagonal terms to zero ($\rho_{ab}^{(0)} = \rho_{ba}^{(0)} = 0$). We then have,

$$\dot{\rho}_{aa} = \lambda_a - \gamma_a \rho_{aa} + \frac{i}{\hbar}(\mathcal{P}E\rho_{ba} - \mathcal{P}E\rho_{ab}), \tag{1.4.6}$$

$$\dot{\rho}_{bb} = \lambda_b - \gamma_b \rho_{bb} - \frac{i}{\hbar}(\mathcal{P}E\rho_{ba} - \mathcal{P}E\rho_{ab}), \tag{1.4.7}$$

$$\dot{\rho}_{ab} = -(i\omega + \gamma)\rho_{ab} - \frac{i}{\hbar}\mathcal{P}E(\rho_{aa} - \rho_{bb}), \tag{1.4.8}$$

where $\lambda_a = r_a \rho_{aa}^{(0)}$ and $\lambda_b = r_b \rho_{bb}^{(0)}$. The equations for the medium are coupled to the field E. Self-consistency requires that the induced polarization of the medium be the driving term for the electromagnetic field. In the following section, we introduce the equations governing the behavior of the classical field from Maxwell's equations.

1.4.2 Maxwell's equations for the field

Classical electromagnetic fields in a material medium are described by Maxwell's equations. The energy loss processes in realistic systems like lasers is accounted for in this problem through inclusion of material conductivity σ which causes linear losses. Lasing emission occurs in certain discrete electromagnetic modes of an optical cavity. To simplify the problem the modes of a unidirectional ring cavity is considered. The electric field $\mathbf{E}$ is given by

$$\mathbf{E}(\mathbf{r}, t) = E(z, t)\hat{\mathbf{x}} \tag{1.4.9}$$

where transverse variations in field are assumed to be small on the scale of an optical wavelength. The unidirectional running wave nature of the mode at frequency ν is expressed by writing

$$E(z,t) = \frac{1}{2}[\mathcal{E}(z,t)e^{-i[\nu t - kz + \phi(z,t)]} + \mathcal{E}(z,t)e^{i[\nu t - kz + \phi(z,t)]}] \tag{1.4.10}$$

Assuming the response of the medium to be linear, the polarization P induced by this field is

$$P(z,t) = \frac{1}{2}[\mathcal{P}(z,t)e^{-i[\nu t - kz + \phi(z,t)]} + \mathcal{P}(z,t)e^{i[\nu t - kz + \phi(z,t)]}] \tag{1.4.11}$$

where $\mathcal{E}(z,t)$, $\mathcal{P}(z,t)$ and $\phi(z,t)$ are slowly varying functions of position and time. The wave vector, $k = \nu/c$. For the laser problem $k = \nu_c/c$, where ν_c represents the cavity frequency. $E(z,t)$ is assumed to be real.

For satisfying the condition of self-consistency, the complex polarization $\mathcal{P}(z,t)$ can be related to the polarization of the medium written in terms of the population matrix elements (Eq.(1.4.5))

$$\mathcal{P}(z,t) = 2\mathcal{P}[\rho_{ab}e^{i[\nu t - kz + \phi(z,t)]} + \rho_{ba}e^{-i[\nu t - kz + \phi(z,t)]}] \tag{1.4.12}$$

The behavior of the electric field and polarization in a material medium is described by the classical electromagnetic wave equations which can be derived using Maxwell's equation. Using the expressions of field $E(z,t)$ and polarization $P(z,t)$ the final form of the wave equation in the medium is

$$\frac{\partial \mathcal{E}}{\partial z} + \frac{1}{c}\frac{\partial \mathcal{E}}{\partial t} = -\mathcal{C}\mathcal{E} - \frac{1}{2\epsilon_0}k\mathrm{Im}\mathcal{P} \tag{1.4.13}$$

$$\frac{\partial \phi}{\partial z} + \frac{1}{c}\frac{\partial \phi}{\partial t} = k - \frac{\nu}{c} - \frac{1}{2\epsilon_0} k \mathcal{E}^{-1} \mathrm{Re}\mathcal{P} \tag{1.4.14}$$

where $\mathcal{C} = \sigma/(2\epsilon_0 c)$ is the linear loss coefficient. The derivatives of the slowly varying amplitude ($\mathcal{E}(z,t)$, $\mathcal{P}(z,t)$) and phase function ($\phi(z,t)$) are ignored in the derivation of the final field equations. The medium polarization given by Eq.(1.4.5) enters the electromagnetic field equations as a source term.

Eqs.(1.4.6-1.4.8) and Eqs.(1.4.13-1.4.14) form the self-consistent set of equations. These equations are applied to construct the semiclassical theory of laser.

1.5 Semi-classical laser theory

The self-consistent Maxwell-Schrödinger equations developed in the previous section (Eqs.(1.4.6-1.4.8) and Eqs.(1.4.13-1.4.14)) are used to derive the semi-classical equations describing the operation of a laser.

The frequency of the resonant modes of a ring cavity are given by,

$$\nu_m = \frac{m\pi c}{S} = k_m c \tag{1.5.1}$$

where S is the circumference of the ring and m is a large integer, typically of the order of 10^6, and k_m is the corresponding wave number. A single mode of a unidirectional ring cavity with traveling waves of the form $\exp(ikz)$ is considered. The Maxwell-Schrödinger equations are solved under the adiabatic elimination of atomic variables. The source term, $\mathcal{P}(z,t)$, for the field equations Eqs.(1.4.13-1.4.14)) requires solution of the population density matrix elements ρ_{ab} (Eq.(1.4.12)). These are solved assuming the population difference $\rho_{aa} - \rho_{bb}$ and the $\mathcal{E}(t)$ do not vary appreciably in the time scale of $1/\gamma$, where $\gamma = (\gamma_a + \gamma_b)/2$ is the decay rate of the atomic levels. The polarization,

$\mathcal{P}(z,t)$, solved using the values of the population density matrix in the steady state, is substituted in the equation of the field so that,

$$\dot{n} = -\kappa n + \frac{\mathcal{A}n}{1+\frac{\mathcal{B}}{\mathcal{A}}n} \tag{1.5.2}$$

$$\nu + \dot{\phi} = \nu_c + \frac{\mathcal{A}(\omega-\nu)}{2\gamma(1+\frac{\mathcal{B}}{\mathcal{A}}n} \tag{1.5.3}$$

and

$$\begin{aligned} \mathcal{A} &= (\frac{\mathcal{P}^2\nu\gamma}{\epsilon_0\hbar})\frac{N_0}{\gamma^2+(\omega-\nu)^2} \\ \mathcal{B} &= (\frac{4\mathcal{P}^2}{\hbar^2})\frac{\gamma^2}{\gamma_a\gamma_b}\frac{\mathcal{A}}{\gamma^2+(\omega-\nu)^2}\frac{\hbar\nu}{2\epsilon_0 V} \end{aligned} \tag{1.5.4}$$

where V is the volume of the cavity. Here $\mathcal{A}$ is the linear gain parameter and $\mathcal{B}$ is the saturation parameter. The equations are written in terms of a dimensionless intensity, $n = \frac{\epsilon_0\mathcal{E}^2V}{2\hbar\nu}$, which corresponds to the number of photons in the lasing mode ($\epsilon_0\mathcal{E}^2V/2$ is the total energy in the laser beam and $\hbar\nu$ is the energy of the photon) instead of the field $\mathcal{E}$. ν_c is the cavity frequency. In the Eqn.(1.4.13) $\mathcal{C}$ has been replaced by $\kappa/2c$, where $\mathcal{C} = \nu_c/Q$ (Q is the quality factor of the cavity) to account for field losses through the mirrors of the cavity. N_0 is the unsaturated inversion given by $\lambda_a\gamma_a^{-1} - \lambda_b\gamma_b^{-1}$. The steady state inversion is given by,

$$\rho_{aa} - \rho_{bb} = \frac{N_0}{1+R/R_S} \tag{1.5.5}$$

where $R_s = \gamma_a\gamma_b/2\gamma$ and $R = \frac{1}{2}(\frac{\mathcal{P}\mathcal{E}}{\hbar})^2\frac{\gamma}{\gamma^2+(\omega-\nu)^2}$ The population difference is N_0 at zero field and increases as the intensity of the electric field increases because of the R/R_S term in the denominator.

For small excitations ($\mathcal{B}n/\mathcal{A} \ll 1$) the denominator in Eqs.(1.5.2-1.5.3) may be expanded to give

$$\dot{n} = (\mathcal{A} - \kappa)n - \mathcal{B}n^2 \tag{1.5.6}$$

$$\nu + \dot{\phi} = \nu_c + \frac{(\omega - \nu)}{2\gamma}(\mathcal{A} - \mathcal{B}n) \tag{1.5.7}$$

Eqs.(1.5.6-1.5.7) are the semi-classical laser equations and many of the physical characteristics of laser operation are explained by these equations. An important characteristic is the lasing threshold condition. To understand this note the steady-state solution ($\dot{n} = 0$) to Eqn.(1.5.6), gives $n = 0$, unless $\mathcal{A} > \kappa$. The steady state intensity is finite for $\mathcal{A} > \kappa$ and is given by

$$n_0 = n = \frac{\mathcal{A} - \kappa}{\mathcal{B}} \tag{1.5.8}$$

Thus the system switches from zero to finite intensity when $\mathcal{A} = \kappa$ and this defines the lasing threshold. Physically, at threshold the gain is equal to cavity losses. The frequency determining Eqn.1.5.7 predicts a pulling of the oscillation frequency from the passive cavity frequency towards line center. In steady-state ($\dot{\phi} = 0$)

$$\nu = \frac{\nu_c + \mathcal{L}\omega}{1 + L} \tag{1.5.9}$$

where $\mathcal{L} = \frac{\kappa}{2\gamma}$. The oscillation frequency ν is equal to an average value of ν_c and ω is pulled closer to the atomic frequency ω. This is called mode-pulling.

In summary the semi-classical theory of laser, solved under the adiabatic approximation, explains the threshold behavior of the mean field and accounts for mode-pulling of cavity frequency. Eq.(1.5.6) requires the presence of photons in the cavity, which can

be amplified by the gain term $\mathcal{A}$. It can not evolve from an initially empty cavity. The quantum mechanical version of this equation contains an extra term $\mathcal{A}$ which accounts for spontaneous emission into the cavity mode (see Chapter 4). This term arises due to vacuum fluctuations appearing in the quantum theory of light and produces the first photon for amplification. In the following chapter we extend this semi-classical theory to explain the behavior of semiconductor lasers. The spontaneous emission into the lasing mode is included in the rate equations as an additional rate. The predictions of the equivalent semiconductor rate equations is considered in detail by performing numerical simulations.

Chapter 2

Rate equation analysis of semiconductor lasers

2.1 Introduction

Similar to an excited electron in a free two-level atom, an electron in the conduction band of a solid can make a transition to an empty state in the valence band emitting a photon in the process. When coupled to a resonant cavity this type of semiconductor emitter can produce lasing behavior. Instead of an excited gas of atoms in a cavity, electrons are injected into the conduction band and holes into the valence band by electrical current. Lasing action was first observed in a current driven GaAs $p-n$ diode maintained at liquid nitrogen temperature (77 K) [Ref.[19]]. Room-temperature operation and other improvements soon followed [Ref.[20]]. The potential use of these devices in commutation systems led to rapid developments in the field of semiconductor lasers. Minimizing the size of these devices for low threshold and high efficiency operation led to the development of microdisk lasers [Ref. [7]] and nano scale lasers [Ref. [40, 49]]. Typically, semi-classical rate equation theories are used to study semiconductor lasers. Future development of smaller devices with smaller particle number [Ref. [31]] necessitates new theories accounting for fluctuations and finite system size. Just how to extend the description of lasers to this fluctuation dominated small particle number limit is the subject of this thesis.

The theory of semiconductor lasers is reviewed in this chapter [Ref. [24]]. The semi-classical rate equations used in describing lasers is discussed and numerical simulation is performed to study the static and dynamic characteristics of these lasers. The origin of the various rates appearing in these equations is explained along with a comparison with the rates appearing for the two-level atomic gain medium. Noise is accounted for by adding noise terms. The limitations of this mean-field model in describing strong fluctuation driven behavior in meso-scale systems is discussed. These equations form a starting point for our master equation treatments of meso-scale lasers in Chapter 3.

2.2 Semiconductor rate equations

The semiconductor rate equations can be constructed by accounting for all the processes occurring in the active region of the gain medium. Instead of active atoms, we have n excited electrons in the conduction band which can transition to the valence band and emit photons into the lasing mode. Thus the excited carrier number n and the lasing photon number s are the quantities of interest and the rate equation for these two quantities are developed. The injection current (pump) I supplies electrons. The excited electrons n can decay to the valence band by radiative or non-radiative processes. The radiative process, involving emission of photons, can occur by spontaneous or stimulated transitions. Spontaneous emission accounts for both emission in the lasing and the non-lasing optical modes. Stimulated emission can only occur in a single lasing mode. Putting all these loss processes together, one can include a term in the rate equation of the form n/τ_n, where τ_n is the lifetime of the excited electron. The rate n/τ_n is equal to $A_{nr}n + Bn^2 + Cn^3$, where A_{nr} accounts for non-radiative processes like collisions. Bn^2 accounts for total spontaneous emission. A fraction β of total spontaneous emission feeds into the lasing mode and produces the first photons in an otherwise empty

cavity (at $T = 0$ K) to be amplified. C is a nonlinear recombination constant. Stimulated emission and absorption is accounted for by adding Gs, where the rate of optical gain G for a bulk medium is given by,

$$G = \Gamma a(n - n_0)(1 - \epsilon s) \tag{2.2.1}$$

in which the confinement factor Γ accounts for the overlap of the field mode with the gain medium. The differential optical gain with respect to carrier density is a and a linear gain model is assumed. The gain saturation term ϵs is important at high intensities. The carrier number at transparency is n_0. Putting all these together, the rate equations for the electrons and the photons are

$$\begin{aligned} \frac{dn}{dt} &= \frac{I}{e} - \frac{n}{\tau_n} - Gs \\ \frac{ds}{dt} &= Gs + \beta B n^2 - \kappa s \end{aligned} \tag{2.2.2}$$

where κ accounts for photon losses due to transmission and absorption and e is electronic charge.

These coupled equations can be solved using the fourth-order Runge Kutta ($RK4$) technique described in Appendix B and transient and steady state behavior can be studied. Figure (2.1) plots typical steady-state and transient characteristics. Calculated steady-state behavior shows the standard threshold behavior of large lasers along with pinning of carriers. The temporal behavior in response to a step change in current shows relaxation oscillations before steady-state is attained. The photon response follows that of the electrons.

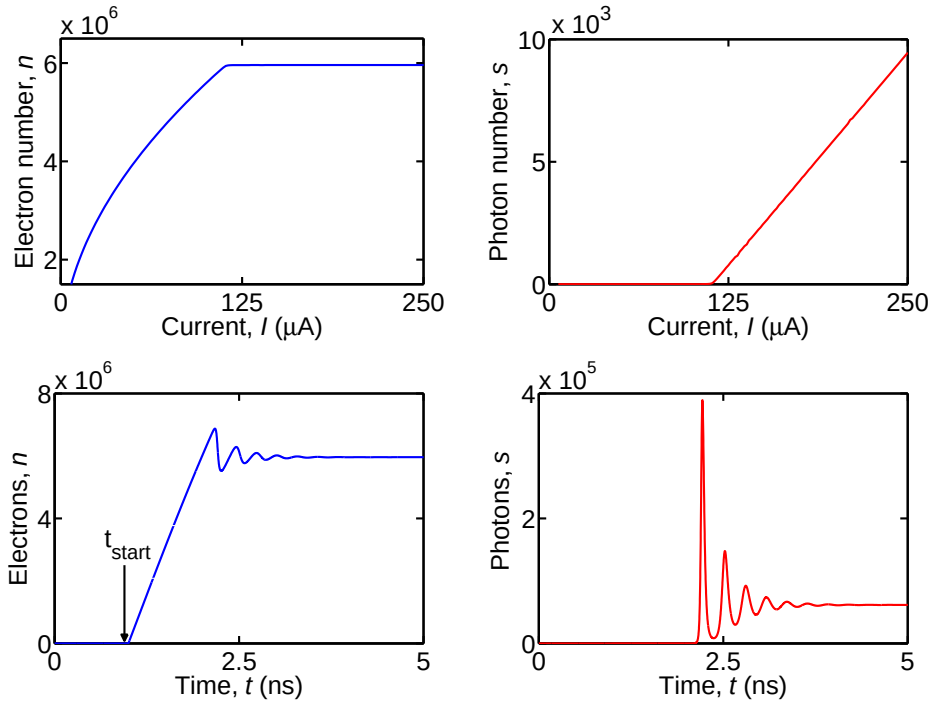

Figure 2.1: Steady state and transient behavior from semiconductor laser rate equations. Steady-state behavior : (a) electron number, n, as a function of injection current, I. (b) photon number, s, as a function of injection current, I. System shows carrier pinning and lasing threshold behavior. Transient response above threshold: Time evolution of (c) electrons, n (d) photons, s to a step change in current. The current of 1 mA is switched on at 1 ns denoted by t_{start}. The system performs relaxation oscillation. Parameters: $V = (5\ \mu\text{m} \times 1\ \mu\text{m} \times 1\ \mu\text{m})$, $\Gamma = 0.25$, $a = 2.5 \times 10^{-16}\ \text{cm}^2\ \text{s}^{-1}$, $B' = 10^{-10}\ \text{cm}^3\ \text{s}^{-1}$, $n_0 = 10^{18}\ \text{cm}^{-3}$, $\alpha_i = 10\ \text{cm}^{-1}$, $n_\text{r} = 4$, $r = 0.999$.

2.3 Gain and spontaneous emission in semiconductor lasers

Typically the different rates used in the rate equations are derived using Fermi's Golden rule. The system is treated semi-classically, in the sense that the electrons are treated quantum mechanically and the light classically. Full quantum treatments involving quantization of the light field Ref.[[45]] produce similar results for large number of particles. The photon rate equation can be compared with the rate equations derived

for the atomic gain medium in the last chapter (Eq.(1.5.6)). The spontaneous emission term, $\mathcal{A}$, is proportional to the inversion and not n^2. The quadratic dependence of the spontaneous emission rate in a semiconductor comes from the band structure.

In thermal equilibrium, the Einstein relation can be written for two level atoms interacting with radiation. Since steady-state transition rates between two levels 1 and 2 are equal, we can write,

$$N_2(B_{21}U(\omega) + A) = N_1 B_{12}.U(\omega) \tag{2.3.1}$$

where N_2 (N_1) are populations of levels 2 (1), B_{21} and B_{12} are stimulated emission and absorption rates between the two levels, A is the spontaneous emission rate and $U(\omega)$ is the background electromagnetic energy density. Einstein's relations in thermal equilibrium are,

$$\begin{aligned} B_{12} &= B_{21} \\ A &= \frac{\hbar\omega^3}{\pi^2 c^3} B_{12} \end{aligned} \tag{2.3.2}$$

where,

$$B_{12} = \frac{\pi e^2}{3\epsilon_0 \hbar^2} \left|\langle 2| \, \mathbf{r} \, |1\rangle\right|^2 \tag{2.3.3}$$

is obtained by using Fermi's Golden rule, for an atom interacting with radiation Ref.[[24]]. Thus the rate of spontaneous emission for two-level atoms is given by AN_2, where A is determined from the above equations.

In contrast, in a semiconductor laser electrons make transitions from the conduction band to the valence band of a direct band-gap semiconductor. In a direct band-gap semiconductor, the maxima of the valence band and the minima of the conduction band

line up. The occupation of the levels in each parabolic band is given by the Fermi-Dirac distribution function f. So a vertical transition is possible, only if there is an occupied state (f) in the conduction band and an unoccupied state in the valence band (1-f). Hence probability of transition is the product $Af(1-f)$. Also instead of each state in a two-level atom (being either excited or not), here we will have to sum over free electron wave-vector states k, in order to get the total transition probability. For an intrinsic semiconductor, this final summation over states produces the n^2 dependence in the expression of spontaneous emission.

For the sake of clarity, this expression is explicitly derived. Assuming a parabolic band, the energy of an electron in the conduction band measured from the top of the valence band is $E_2 = E_g + \frac{\hbar^2 k^2}{2m_e^*}$ and the energy of an electron in the valence band is $E_1 = -\frac{\hbar^2 k^2}{2m_{hh}^*}$ where E_g is the band-gap energy, m_e^* is the effective electron mass and m_{hh}^* is the effective heavy-hole mass. The energy due to a vertical electronic transition from the conduction to valence band is

$$\hbar\omega = E_2 - E_1 = \frac{\hbar^2 k^2}{2}(\frac{1}{m_e^*} + \frac{1}{m_{hh}^*}) + E_g = \frac{\hbar^2 k^2}{2m_r} + E_g \tag{2.3.4}$$

where $\frac{1}{m_r} = (\frac{1}{m_e^*} + \frac{1}{m_{hh}^*})$ and m_r is the effective reduced electron mass. It follows, that the 3-dimensional density of states coupled by optical transition of energy $\hbar\omega$ is

$$D_3(\hbar\omega) = \frac{1}{2\pi^2}(\frac{2m_r}{\hbar^2})^{\frac{3}{2}}(\hbar\omega - E_g)^{\frac{1}{2}} \tag{2.3.5}$$

The same value of k in the valence and conduction band is required for momentum conservation. This is because the linear dispersion of light is almost vertical ($\omega = ck_{opt}/n_r$) compared to the quadratic dispersion of electrons in a band and so the photon carries off negligible momentum. A clearer explanation can be found by deriving the

exact form of the matrix elements between the transition states Ref.[[24]]. The Fermi-Dirac distribution of a band α is

$$f_{\alpha\mathbf{k}} = \frac{1}{e^{\beta(E_{\alpha\mathbf{k}}-\mu_\alpha)}+1} \tag{2.3.6}$$

where β is $1/k_BT$, the chemical potential is μ_a, electron energy is $E_\alpha = \frac{\hbar^2k^2}{2m_\alpha}$ for a band with effective electron mass m_α. If the chemical potential is large and negative, then $E_{\alpha\mathbf{k}} - \mu_\alpha \gg k_BT$ and in this limit we obtain the Maxwell-Boltzmann distribution, $f_{\alpha\mathbf{k}} \simeq e^{\beta\mu_\alpha}e^{-\beta E_{\alpha\mathbf{k}}}$. Letting $\epsilon = \frac{\beta\hbar^2}{2m_\alpha}$, the carrier density in the band is given by,

$$n_\alpha = 4\pi\int_0^\infty 2f_\alpha k^2\frac{dk}{(2\pi)^3} = \frac{e^{\beta\mu_\alpha}}{\pi^2}\int_0^\infty e^{-\epsilon k^2}k^2dk = -\frac{e^{\beta\mu_\alpha}}{\pi^2}\frac{\partial}{\partial\epsilon}(\int_0^\infty e^{-\epsilon k^2}dk) = \frac{1}{4}(\frac{2m_\alpha k_BT}{\pi\hbar^2})^{\frac{3}{2}}e^{\beta\mu_\alpha} \tag{2.3.7}$$

where one makes use of the standard integral

$$\int_0^\infty e^{-ax^2}dx = \frac{1}{2}\sqrt{\frac{\pi}{a}} \tag{2.3.8}$$

For total spontaneous emission, we have to calculate,

$$r_{spon-total} = \int r_{spon}(\hbar\omega)d\omega = r_0\int D_3(\hbar\omega)f_ef_{hh}d\omega = r_0\sum_{\mathbf{k}} f_{e\mathbf{k}}f_{hh\mathbf{k}} \tag{2.3.9}$$

We let, $\epsilon = \frac{\beta\hbar^2}{2m_r}$, and calculate the sum of all vertical transitions,

$$\sum_{\mathbf{k}} f_{e\mathbf{k}}f_{hh\mathbf{k}} = \frac{e^{\beta\mu_e}e^{\beta\mu_{hh}}}{\pi^2}\int_0^\infty e^{-\epsilon k^2}k^2dk = e^{\beta\mu_e}e^{\beta\mu_{hh}}\frac{1}{4}(\frac{2m_rk_BT}{\pi\hbar^2})^{\frac{3}{2}} \tag{2.3.10}$$

From our previous calculation,

$$e^{\beta\mu_\alpha} = 4n_\alpha(\frac{\pi\hbar^2}{2m_\alpha k_B T})^{\frac{3}{2}} \tag{2.3.11}$$

and because, from charge neutrality, n_e = n_{hh} = n, we have,

$$\sum_{\mathbf{k}} f_{e\mathbf{k}} f_{hh\mathbf{k}} = n^2 4(\frac{\pi\hbar^2 m_r}{2m_e m_{hh} k_B T})^{\frac{3}{2}} \tag{2.3.12}$$

from which we may conclude that the total spontaneous emission is proportional to n^2. For low temperatures or high n, the spontaneous emission increases slower than n^2, because the requirement $f \leq 1$ becomes important. The expression for optical gain can be similarly obtained using Einstein's relations and Fermi's golden rule. If we consider transition between two discrete levels 1 and 2 in the valence and conduction band respectively, then the net absorption in presence of photons of energy $\hbar\omega$ =$(E_2 - E_1)$ is

$$\alpha = \frac{R_{12}^{stim} - R_{21}^{stim}}{P(\hbar\omega)\frac{c}{n_r}} = \frac{B_{12}P(\hbar\omega)f_1(1-f_2) - B_{21}P(\hbar\omega)f_2(1-f_1)}{P(\hbar\omega)\frac{c}{n_r}} \tag{2.3.13}$$

The equation is written in analogy with the two-level system and $P(\hbar\omega)\frac{c}{n_r}$ represents the net photon flux, where n_r is the refractive index. B_{12} is determined by Fermi's golden rule in terms of the matrix elements as

$$B_{21} = \frac{2\pi}{\hbar}\left|\langle 2|\, e\mathbf{r}\,|1\rangle\right|^2 = \frac{2\pi}{\hbar}\left|W_{21}\right|^2 \tag{2.3.14}$$

On summing Eq.(2.3.13) over allowed transition states k, using density of states $D_3(\hbar\omega)$, one can obtain the expression for semiconductor gain as,

$$g(\hbar\omega) = -\alpha(\hbar\omega) = \frac{2\pi n_r}{c\hbar}\left|W_{21}\right|^2 \frac{1}{2\pi^2}(\frac{2m_r}{\hbar^2})^{\frac{3}{2}}(\hbar\omega - E_g)^{\frac{1}{2}}(f_e + f_{hh} - 1) \tag{2.3.15}$$

The condition of lasing or positive optical gain requires,

$$\mu_2 - \mu_1 > E_{21} \tag{2.3.16}$$

which is known as the Bernard-Duraffourg condition. The expression of $g(\hbar\omega)$ can be plotted against energy, $\hbar\omega$. From figure (2.2 b) we see the maxima of the gain increases with electron density and the dependence is found to be linear. It is this maximum gain energy which coincides with the cavity mode frequency. This is the reason for using a linear model of gain the rate equation for electrons, n and photons, s.

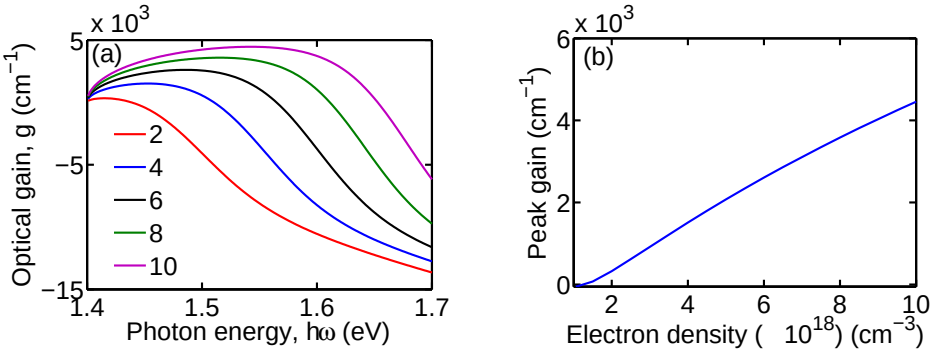

Figure 2.2: (a) Behavior of gain function with energy, $\hbar\omega$ for different carrier densities. The factors in the legend multiplied by 1×10^{18} gives the carrier density. (b) Peak gain versus carrier density. Parameters m_e = 0.07, m_{hh} = 0.5, T = 300 K, E_g = 1.4 eV.

2.4 Noise in semiconductor lasers

The semiconductor laser rate equations can be modified slightly to Langevin form

$$\begin{aligned} \frac{dn}{dt} &= \frac{I}{e} - \frac{n}{\tau_n} - Gs + F_e(t) \\ \frac{ds}{dt} &= Gs + \beta Bn^2 - \kappa s + F_s(t) \end{aligned} \tag{2.4.1}$$

by adding external Gaussian random noise terms $F_e(t)$ and $F_s(t)$, which are described by the following correlation functions,

$$\begin{aligned}
\langle F_e(t)F_e(t')\rangle &= (\frac{I}{e} + \frac{n}{\tau_n} + Gs)\delta(t-t') \\
\langle F_s(t)F_s(t')\rangle &= (Gs + \beta Bn^2 + \kappa s)\delta(t-t') \\
\langle F_e(t)F_s(t')\rangle &= -(Gs + \beta Bn^2)\delta(t-t')
\end{aligned} \tag{2.4.2}$$

where the cross-correlation in the last term indicates that the equations of n and s are coupled and negative sign means they are anticorrelated. The prefactors in front of the correlations are the variances of these Gaussian noise sources which are Markovian in nature because of the delta function, $\delta(t-t')$. The original rate equations (Eq.(2.2.2)) do not account for noise in the laser output due to fluctuations. Thus noise properties of the system is studied by imposing external noise. The Fourier transform of the temporal behavior, $s(t)$, shows a peak at a characteristic frequency which increases with increasing pump, similar to the relaxation oscillation frequency.

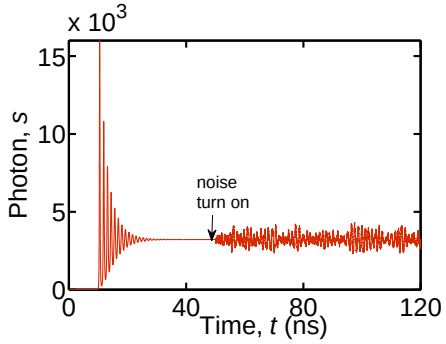

Figure 2.3: Transient response in presence of noise above threshold: Time evolution of photons, s . The current of 1 mA is switched on at 1 ns. Noise introduced after system attains steady-state. Parameters: same as in Figure 1.

The approach to the study of noise by adding external Gaussian noise is valid in the presence of large particle numbers. The treatment is not valid in the presence of a small

number of photons near threshold. Thus the behavior of fluctuations around threshold in meso-scale lasers considered in Chapter 3 can not be explained by this technique. Small systems dominated by fluctuations is the physical scenario where the continnum mean-field theories break down. To overcome this limitation, we develop a semi-classical master equation theory in Chapter 3 which accounts for system probabilities and is better suited to the study of fluctuation-driven behavior in small quantum systems.

Chapter 3

Semi-classical treatment of meso-scale lasers

3.1 Introduction

The physics determining operation of a conventional laser is quite well understood in the thermodynamic limit. In this case there is a large number of excited states in the system, the fraction of spontaneous emission, β, feeding into the lasing optical mode is small ($\beta \sim 10^{-4}$), and there is a well-defined threshold between incoherent non-lasing photon emission and coherent lasing photon emission. The approximate behavior of these systems may be described using continuum mean-field rate equations. Beyond these relatively crude models, quantum statistical theories of laser operation exist. When evaluated in the large particle number limit they successfully reproduce the continuum mean-field results and may be used to model particle number fluctuations and statistics in the thermodynamic limit. Well established models of this type include Fokker-Plank equations developed by Haken [Ref.[12]] and a density matrix approach by Scully and Lamb [Ref.[13, 14, 15]]. The ensemble averages used in these models cannot be applied to small systems involving a few particles. However, they do highlight the importance of quantum fluctuations in relatively large lasers. For example, experiments show that fluctuations in photon number play an essential role in determining the temperature dependence of conventional laser diodes [Ref.[55, 56, 57]]. In these devices, and in agreement with the Landau-Ginzburg theory of phase transitions, fluctuations enhance

photon emission below threshold and suppress spontaneous emission. This behavior occurs because the devices are large and operate in the thermodynamic limit. The situation is expected to be qualitatively different when the laser is small and the discrete quantum nature of the particles in the system influences device behavior. It is this change in the physics determining laser operation that we set out to address.

Recently a considerable amount of research has focussed on developing small lasers with ultra-low threshold values [Ref.[7, 21, 22, 23]]. One idea employs the cavity-QED effect [Ref.[5]] in which optical emission from an atom may be modified by changing its electromagnetic environment. The threshold of single-mode lasers may be reduced if the fraction of spontaneous emission, β, feeding into the lasing mode is increased. This is achieved by inhibiting emission into non-lasing optical modes using high-Q microcavities. The limiting case is $\beta = 1$ in which all the spontaneous emission feeds into the lasing mode.

Typically, continuum mean-field rate equations have been employed to describe laser diode behavior. The equations used are of the form (Eq.(2.2.2))

$$\frac{d\langle n\rangle}{dt} = -B\langle n\rangle^2 - \frac{a\Gamma c}{Vn_{\rm r}}\langle(n-n_0)\rangle\langle s\rangle + \frac{I}{e}, \tag{3.1.1}$$

$$\frac{d\langle s\rangle}{dt} = \beta B\langle n\rangle^2 + \frac{a\Gamma c}{Vn_{\rm r}}\langle(n-n_0)\rangle\langle s\rangle - \kappa\langle s\rangle, \tag{3.1.2}$$

where $\langle n\rangle$ is the mean carrier number in the active volume V and $\langle s\rangle$ is the mean photon number in the optical cavity. In the equations, $\frac{a\Gamma c}{Vn_{\rm r}}\langle(n-n_0)\rangle\langle s\rangle$ is the stimulated emission term for a bulk active region, c is the speed of light in vacuum, n_0 is the carrier number at optical transparency, a is the optical gain slope coefficient, Γ is the optical confinement factor, and $n_{\rm r}$ is the refractive index of the medium. The term $-B\langle n\rangle^2$

describes spontaneous emission where $B = B'/V$ and B' is the spontaneous emission coefficient. Other contributions to the carrier recombination are often included in Eq.(3.1.1). For example $-A_{\rm nr}\langle n\rangle$ can be used to describe non-radiative recombination and $-(C/V^2)\langle n\rangle^3$ is a nonlinear contribution to recombination. The term $\kappa\langle s\rangle$ denotes cavity loss rate of photons where $\kappa = \frac{c}{n_{\rm r}}(\alpha_i + \frac{1}{2L_{\rm c}} ln(\frac{1}{r_1 r_2}))$, cavity length is $L_{\rm c}$, mirror reflectivity is $r_1 = r_2 = r$, and α_i is the internal optical loss. The injection current is I and e is the electron charge. As shown in Fig. 3.1, calculations using Eq.(3.1.1) predict the threshold behavior in mean photon number $< s >$ with injection current I smoothes with increasing β and disappears entirely for $\beta = 1$.

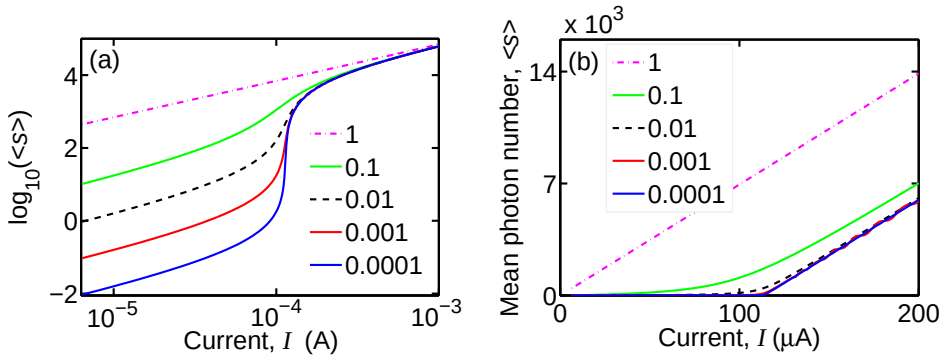

Figure 3.1: Continuum mean-field rate equation calculation of mean photon number, $< s >$, as a function of injection current, I, for the indicated values of β showing transition to "threshold-less" lasing in the limit $\beta = 1$. (a) $\log_{10} < s >$ as a function of $\log_{10} I$. (b) $< s >$ as a function of I. Parameters: $V = (5\,\mu{\rm m}\times 1\,\mu{\rm m}\times 1\,\mu{\rm m})$, $\Gamma = 0.25$, $a = 2.5\times 10^{-16}\,{\rm cm}^2\,{\rm s}^{-1}$, $B' = 10^{-10}\,{\rm cm}^3\,{\rm s}^{-1}$, $n_0 = 10^{18}\,{\rm cm}^{-3}$, $\alpha_i = 10\,{\rm cm}^{-1}$, $n_{\rm r} = 4$, $r = 0.999$.

Figure 3.2 shows images of semiconductor lasers where continuum mean-field rate equations can be applied. Figure 3.2 (a) is a photograph of a conventional Fabry-Perot laser diode. Cavity length is $L_{\rm c} = 300\ \mu{\rm m}$, $\beta = 5 \times 10^{-5}$, and the active volume is $15\ \mu{\rm m}^3$. The horizontal metal stripe makes contact to p-type semiconductor, the substrate is n-type, and six quantum wells form the active volume at the diode p-n junction. The device parameters are that of an InGaAsP laser with emission at 1310 nm wavelength [Ref.[24]]. Figure 3.2 (b) shows a microdisk laser [Ref.[25]] which has an active

volume approximately 100 times smaller compared to the Fabry-Perot laser. The much larger value of $\beta = 10^{-1}$ for this device is achieved by reducing optical cavity size.

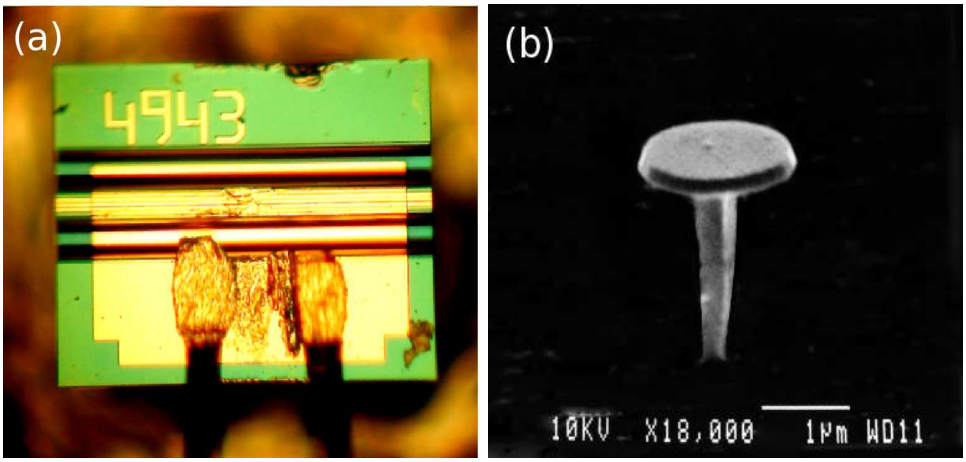

Figure 3.2: (a) Photograph from the top surface of a typical Fabry-Perot laser diode with $L_{\mathrm{c}} = 300\ \mu\mathrm{m}$ and $I_{\mathrm{th}} = 3\ \mathrm{mA}$. Photon cavity round-trip time in the device is $8\ \mathrm{ps}$. The horizontal metal stripe makes electrical contact to p-type semiconductor. Gold wire bonds connect to the anode of the current supply driving the laser. The n-type semiconductor contact is made via the backside of the semiconductor substrate. (b) Scanning electron microscope image of an optically-pumped microdisk laser. Image from [Ref.[25]]. Disk diameter is $1.6\ \mu\mathrm{m}$ and the photon cavity round-trip time is $0.06\ \mathrm{ps}$.

The continuum mean-field rate equations, useful for large and intermediate-size systems, is an approximate calculation of the first moment in the distribution of n and s. A description using only the first moment $< n >$ and $< s >$ is not sufficient to describe the behavior of lasers scaled to have small active volumes. Any model of very small lasers should explicitly include fluctuations and be able to calculate higher-order moments in the distribution of n and s.

In principle, a quantum theory of laser operation can incorporate these higher-order effects. However, the approximations typically employed constrain them to either large-scale systems or single atoms. The problem of a single two-level atom in an optical cavity is solvable and has been extensively studied in quantum optics [Ref.[12, 15, 26, 27]].

In fact, theoretical predictions for light emission from single atoms and single quantum dots [Ref.[30, 31, 32]] in optical micro-cavities exhibit interesting features such as self-quenching and squeezed light emission. Extension of this approach to include multi-atom effects requires numerical computation. Unfortunately, the number of system states scales as $(2^n)s$, where n is the number of two-level atoms present and s is the number of cavity photons. Thus, the problem becomes computationally challenging with increasing number of atoms inside the cavity because the coefficient matrix is of order $(4^n)s \times (4^n)s$. Cases studied so far involve 1 or 2 atoms and solutions are obtained numerically by truncating the coupled density matrix equations [Ref.[32]]. Treatments involving arbitrary number of excited states include approximations of a reservoir level, which excludes important phenomena appearing in the small-scale limit [Ref.[18]]. Systematic studies have also been performed for micro-masers where bulk and single particle effects (trapped states) have been investigated [Ref.[17]] but the maximum number of atoms simultaneously present in the cavity was limited to 5. By modifying the injection technique [Ref.[33]], up to 100 atoms have been included in the cavity.

In this chapter we develop a description that quantizes particle energy and allows study of meso-scale systems. Our approach captures the most significant quantum effects in these small-scale systems. In particular, it allows exploration of quantum fluctuations and its impact on the behavior of small laser diodes.

This chapter is organized as follows. In Section 3.2 we explore the behavior of small lasers using a technique based on a random walk method. Description of the method is followed by calculation of the steady-state characteristics of meso-scale devices. Convergence with continuum mean-field rate equation results is achieved for large systems. Section 3.3 discusses the use of master equations to study similar systems. This approach gives predictions in agreement with those of Section 3.2. Section 3.4 applies

the methods of Section 3.2 and 3.3 to the study of transient characteristics. The algorithm used in computation of this problem is discussed in detail. Section 3.5 addresses aspects of experimental design and Section 3.6 is a summary and describes possible future directions.

3.2 Random walk trajectory

To capture the physics dominating the meso-scale behavior of laser diode operation when there is only a small number of excited states in the system we have used a technique based on a biased random walk or Monte-Carlo trajectory [Ref.[34]]. Quantization of n discrete excited electronic states and s discrete photons is achieved by assuming the system may be described by the state (n, s).

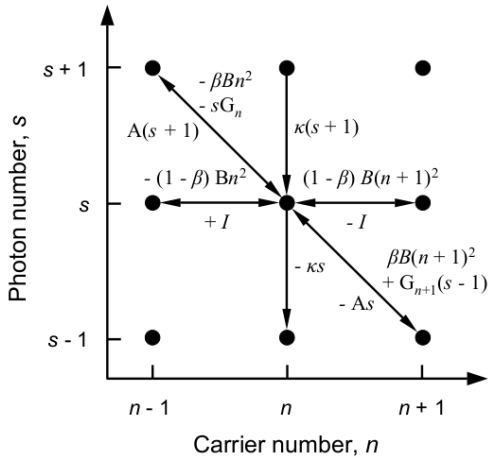

Figure 3.3: Transition rates in and out of quantum state (n, s). Positive signs indicate flow into the state and negative signs flow out of the state. B is the spontaneous emission coefficient, $-G_n s = (a\Gamma cn/Vn_{\rm r})s$ is the stimulated emission rate in the system at photon energy $\hbar\omega$, $-As = (a\Gamma cn_0/Vn_{\rm r})s$ is the stimulated absorption rate, n_0 is the transparency carrier number, c is the speed of light in vacuum, Γ is the overlap of the optical field intensity with the gain medium, a is the gain slope coefficient, and $n_{\rm r}$ is the refractive index of the active volume V. The total optical loss rate from the Fabry-Perot cavity is $\kappa s = \frac{c}{n_{\rm r}}(\alpha_i + \frac{1}{2L_{\rm c}} ln(\frac{1}{r_1 r_2}))s$, where $r_1 = r_2$ is the mirror reflectivity, α_i is the internal loss, and $L_{\rm c}$ is the cavity length. I is the injection (pump) current and e is the electron charge.

Consider the system at time t = 0 containing n excited two-level electronic states each separated in energy by $\hbar\omega$ and s photons each of energy $\hbar\omega$. Figure 3.3 illustrates the transitions in and out of state (n, s). The term $-\beta Bn^2$ describes the spontaneous emission of photons involving transitions from state (n, s) to state $(n-1, s+1)$ where $B = B'/V$ and B' is the spontaneous emission coefficient. $-sG_n$ describes stimulated emission of photons from state (n, s) to state $(n-1, s+1)$ where G_n is the stimulated emission coefficient. $-(1-\beta)Bn^2$ is the decay of electrons into non-lasing photons via transitions from state (n, s) to state $(n-1, s)$. Current $+I$ denotes injection of electrons causing transitions from state (n, s) to state $(n+1, s)$. $-As$ is stimulated absorption of photons involving transitions from state (n, s) to state $(n+1, s-1)$ where A is the stimulated absorption coefficient. $-\kappa s$ describes the decay of cavity photons in which transitions from state (n, s) to state $(n, s-1)$ occur, where κ is the optical loss coefficient.

The system evolves by transitioning between neighboring states via the processes indicated in Fig. 3.3. The time constants, τ_i, of all possible independent transitions involving the state (n, s) are calculated. The next time step is calculated using $t_i = -\tau_i ln(\mathrm{RAND})$ where the subscript labels the channel and RAND is a uniformly distributed random number between zero and one. The transition with the lowest t_i is chosen and the system makes a move to the new state in time t_i. The process involves a series of biased random transitions on a grid whose trajectories sample the continuous probability function $P_{n,s}$ for each state (n, s). Steady-state probability distribution for a particular injection current is obtained by averaging over multiple trajectories where each trajectory consists of millions of time steps. The probability of state (n, s) is $P_{n,s}$. This probability is estimated from the relative time spent in state (n, s). This technique is ideal for parallel computing as it mostly involves repeated sampling without any large

memory requirements. Each processor can independently perform calculations for each pump current and produce the entire steady-state characteristic in the end.

Fluctuations and correlations are expected to have a strong effect on the behavior of small lasers. Figure 3.4 shows steady-state characteristics for lasers with different active volumes. Continuum mean-field rate-equation results are compared with those obtained from the biased random walk technique. All the devices considered operate in the limit where strong coherent effects, such as Rabi oscillations, are absent [Ref.[15, 39]].

Figures 3.4 (a) and (b) show results for a Fabry-Perot laser diode with $\beta = 5 \times 10^{-5}$ and active volume $V = 33.6\ \mu\mathrm{m}^3$. The expected classical laser threshold behavior and carrier pinning above threshold is observed. Total optical output power in mW at an operating emission wavelength of 1310 nm can be determined by multiplying the photon number by 5.2×10^{-5}.

Figures 3.4 (c) and (d) give results for a micro-disk laser with active volume $V = 0.12\ \mu\mathrm{m}^3$. Optical output power in μW at 1310 nm wavelength is obtained by multiplying the photon number by 7.1×10^{-3}. The steady-state characteristics show that the change in slope of $< s >$ around the phase transition region is considerably smoothed due to the large value of $\beta = 0.1$.

Figures 3.4 (e) and (f) give the steady-state characteristics of a laser where the active volume has been reduced to $V = 10^{-4}\ \mu\mathrm{m}^3$ and $\beta = 10^{-4}$. Suppression of lasing is observed along with de-pinning of carriers in the limit of small active volume and small β values. Optical output power in nW at a wavelength of 800 nm is obtained by multiplying the photon number by 0.186. Increasing β for this small cavity as shown in Figures 3.4 (g) and (h), provides a better agreement with mean-field predictions. The mean photon number matches closely. The mean carrier number however deviates by a small amount around the threshold region.

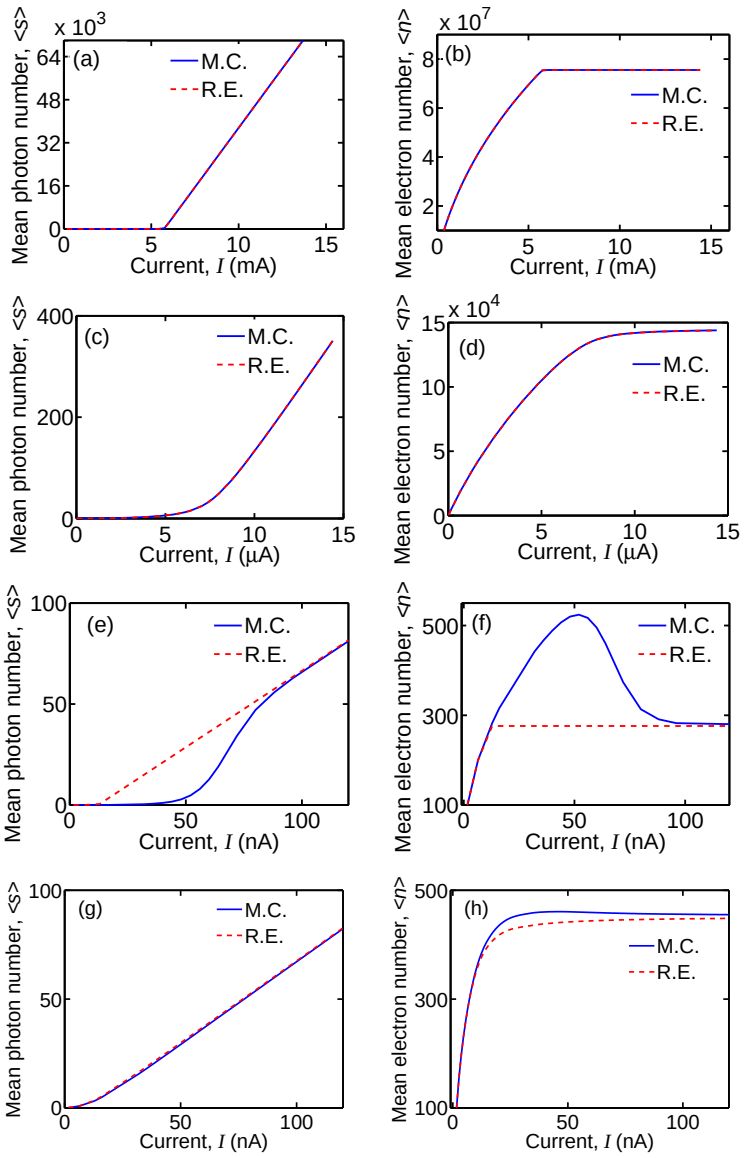

Figure 3.4: Steady-state characteristics. Mean photon and electron number in the device plotted as a function of injection current. Continuum mean-field rate equation calculation (dashed line - R.E.) compared with results from our random trajectory Monte-Carlo technique (solid line - M.C.). (a, b) Fabry - Perot laser. (c, d) Microdisk laser. (e, f) Laser with meso-scale active volume. Parameters for (a) and (b): $V = (300\ \mu\text{m} \times 0.8\ \mu\text{m} \times 0.14\ \mu\text{m})$, $\Gamma = 0.25$, $a = 2.5 \times 10^{-16}\ \text{cm}^2\ \text{s}^{-1}$, $B' = 10^{-10}\ \text{cm}^3\ \text{s}^{-1}$, $A_{\text{nr}} = 2 \times 10^8\ \text{s}^{-1}$, $C = 10^{-29}\ \text{cm}^6\ \text{s}^{-1}$, $n_0 = 10^{18}\ \text{cm}^{-3}$, $\alpha_i = 40\ \text{cm}^{-1}$, $n_{\text{r}} = 3.3$, $r = 0.32$, $\beta = 5 \times 10^{-5}$. Parameters for (c) and (d): $V = (\pi \times (0.8\ \mu\text{m})^2 \times 0.06\ \mu\text{m})$, $\Gamma = 0.25$, $a = 2.5 \times 10^{-16}\ \text{cm}^2\ \text{s}^{-1}$, $B' = 10^{-10}\ \text{cm}^3\ \text{s}^{-1}$, $A_{\text{nr}} = 2 \times 10^8\ \text{s}^{-1}$, $C = 10^{-29}\ \text{cm}^6\ \text{s}^{-1}$, $n_0 = 10^{18}\ \text{cm}^{-3}$, $\alpha_i = 10\ \text{cm}^{-1}$, $n_{\text{r}} = 4$, $r = 0.999$, $\beta = 10^{-1}$. Parameters for (e) , (f), (g) and (h): $V = (0.1\ \mu\text{m} \times 0.1\ \mu\text{m} \times 10\ \text{nm})$, $\Gamma = 0.25$, $a = 2.5 \times 10^{-18}\ \text{cm}^2\ \text{s}^{-1}$, $B' = 10^{-10}\ \text{cm}^3\ \text{s}^{-1}$, $n_0 = 10^{18}\ \text{cm}^{-3}$, $\alpha_i = 1\ \text{cm}^{-1}$, $n_{\text{r}} = 4$, $r = 1 - 10^{-6}$, $\beta = 10^{-4}$ for (e) and (f) and $\beta = 10^{-1}$ for (g) and (h).

Carrier de-pinning near threshold may be investigated further by accounting for spontaneous emission of photons into a non-lasing channel. The $(1-\beta)$ term (Figure 3.3) populates another channel containing s'' photons which decay at the same rate as the cavity photons. This channel does not participate in any stimulated photon processes.

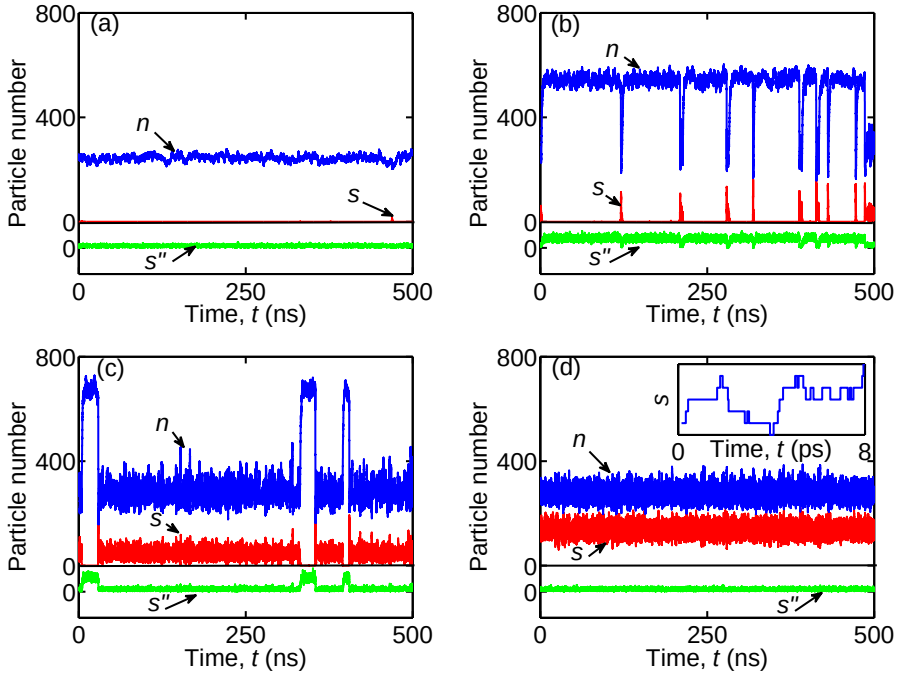

Figure 3.5: Time evolution of electrons and photons calculated by a random trajectory. (a) Current, I = 9.6 nA. (b) I = 48 nA. (c) I = 72 nA. (d) I = 192 nA. The inset shows discrete step changes in photon number with time. Parameters are as in Fig. 3.4 (e) and (f) : $V = (0.1\ \mu\text{m} \times 0.1\ \mu\text{m} \times 10\ \text{nm})$, $\Gamma = 0.25$, $a = 2.5 \times 10^{-18}\ \text{cm}^2\ \text{s}^{-1}$, $B' = 10^{-10}\ \text{cm}^3\ \text{s}^{-1}$, $n_0 = 10^{18}\ \text{cm}^{-3}$, $\alpha_i = 1\ \text{cm}^{-1}$, $n_\text{r} = 4$, $r = 1 - 10^{-6}$, $\beta = 10^{-4}$.

Figure 3.5 shows trajectories calculated in the time-domain for different injection currents for a very small active volume laser with parameters as in Figs. 3.4 (e) and (f). The spontaneous emission terms are also included in the calculation. The calculated time-domain data in Figs. 3.5 (a) and (b) show bursts of photons because of the presence of large fluctuations and the injection current is not great enough to sustain continuous

lasing. With increasing injection current, longer lasting photon bursts result in a double-peaked average electron distribution. This is well illustrated by the data in Fig. 3.5 (c). For operation near threshold switching occurs between two different characteristic system states. Figure 3.5 (d) is an example of strong lasing with quantized photon fluctuations about a mean value $\langle s \rangle = 136$. This trajectory compares closely to the Langevin trajectories generated by adding Gaussian noise to the continuum mean-field rate equations (Eq. 2.4.1). This analogy is considered in greater detail in Section 1.5 B. The average output power from both cavity mirrors is around 25 nW at an operating wavelength of 0.8 μm. In this case $s'' = 9.5$.

There is less noise in carrier number n in Fig. 3.5 (a) when there are essentially only electrons in the system and very few lasing photons. As illustrated in Fig. 3.5 (c), when both photons and electrons are in the system the electron noise is enhanced because photon noise couples into the electron distribution. When the cavity empties of photons the number of electrons increases but the noise decreases. This is because noise coupled into the electron system from the photons is no longer present.

The Fano-factor, F may be used to quantify photon fluctuations.

$$F = {\sigma_s}^2 / < s > \tag{3.2.1}$$

where σ_s is the standard deviation in photon number. The phase transition in a conventional laser is accompanied by large photon fluctuations and this quantity peaks sharply near lasing threshold, $I_{\rm th}$. For large injection currents, $I \gg I_{\rm th}$, the Fano-factor approaches unity, corresponding to a Poisson distribution. For small active volumes the sharp transition is replaced by a broad peak in the Fano-factor in the vicinity of the threshold and $F > 1$, indicating a non-Poisson distribution.

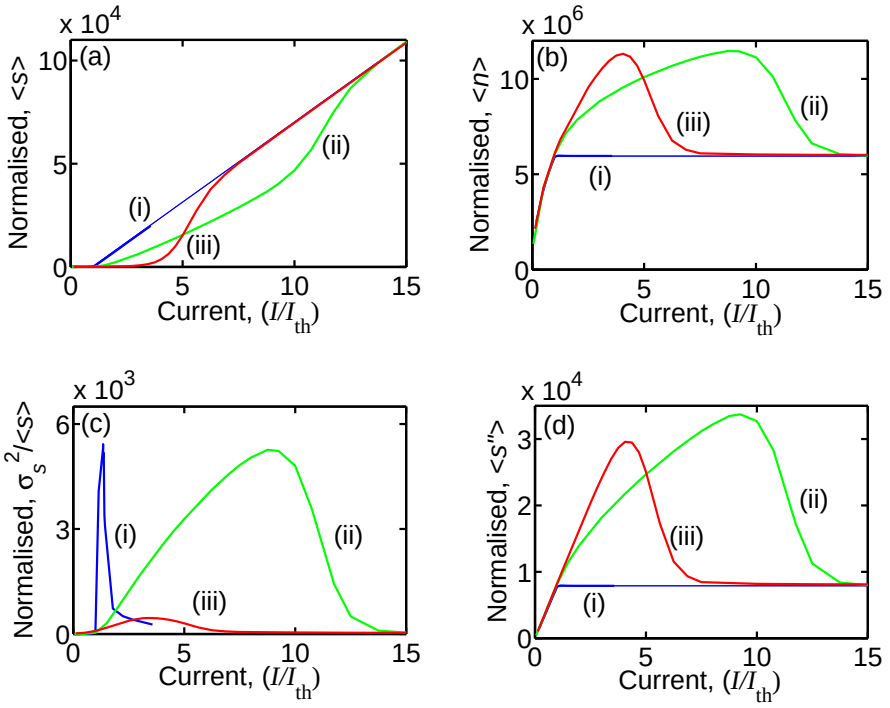

Figure 3.6: Comparison of steady-state laser characteristics for three different active volumes. (a) Normalized mean photon number versus current. (b) Normalized mean electron number versus current. (c) Normalized Fano-factor versus current. (d) Normalized spontaneous emission photon number versus current. (i) Results for a large active volume, (ii) an intermediate sized active volume, (iii) a small active volume (Fig. 3.5). The calculations for the large active volume device matches the continuum mean-field rate equations data closely. The current values are normalized by dividing by the respective threshold currents predicted by continuum mean-field rate equations ($I_{\mathrm{th-i}} = 112\ \mu$A, $I_{\mathrm{th-ii}} = 320$ nA, $I_{\mathrm{th-iii}} = 12.8$ nA). Normalization constants, N are: Mean photon number, $\mathrm{N}s_{\mathrm{i}} = 1$, $\mathrm{N}s_{\mathrm{ii}} = 350$, $\mathrm{N}s_{\mathrm{iii}} = 800$. Mean electron number, $\mathrm{N}n_{\mathrm{i}} = 1$, $\mathrm{N}n_{\mathrm{ii}} = 607$, $\mathrm{N}n_{\mathrm{iii}} = 21594$. Mean spontaneous emission photon number, $\mathrm{N}s''_{\mathrm{i}} = 1$, $\mathrm{N}s''_{\mathrm{ii}} = 370$, $\mathrm{N}s''_{\mathrm{iii}} = 855$. Fano factor, $\mathrm{N}F_{\mathrm{i}} = 1$, $\mathrm{N}F_{\mathrm{ii}} = 1$, $\mathrm{N}F_{\mathrm{iii}} = 10$. Parameters: $V_{\mathrm{i}} = (5\ \mu\mathrm{m} \times 1\ \mu\mathrm{m} \times 1\ \mu\mathrm{m})$, $V_{\mathrm{ii}} = (5\ \mu\mathrm{m} \times 0.1\ \mu\mathrm{m} \times 10$ nm), $V_{\mathrm{iii}} = (0.1\ \mu\mathrm{m} \times 0.1\ \mu\mathrm{m} \times 10$ nm), $\Gamma_{\mathrm{i,iii}} = 0.25$, $\Gamma_{\mathrm{ii}} = 0.05$, $a_{\mathrm{i,ii}} = 2.5 \times 10^{-16}$ cm^2 s^{-1}, $a_{\mathrm{iii}} = 2.5 \times 10^{-18}$ cm^2 s^{-1}, $B' = 10^{-10}$ cm^3 s^{-1}, $n_0 = 10^{18}$ cm^{-3}, $\alpha_i = 10$ cm^{-1} for (i,ii), $\alpha_i = 1$ cm^{-1} for (iii), $n_{\mathrm{r}} = 4$, $r_{\mathrm{i,ii}} = 0.999$, $r_{\mathrm{iii}} = 1 - 10^{-6}$ and $\beta = 10^{-4}$.

In Fig. 3.6 the steady-state laser characteristics of (i) a large active volume device ($V = 5\ \mu\mathrm{m}^3$), (ii) an intermediate volume ($V = 5 \times 10^{-3}\ \mu\mathrm{m}^3$), and (iii) a small volume ($V = 10^{-4}\ \mu\mathrm{m}^3$) are shown. The data are normalized to the large active volume device

continuum mean-field rate-equation predictions for $\langle n \rangle$ and $\langle s \rangle$. Figure 3.6 (a) compares $\langle s \rangle$ as a function of I between different cavities and convergence with the continuum mean-field rate equations is achieved for the largest cavity. Lasing is increasingly suppressed with the reduction of active volume. The normalized Fano-factor as a function of normalized current exhibits a peak around the threshold region. As expected, the largest active volume device exhibits the sharpest threshold behavior. In general, the peak identifies the presence of strong fluctuations and non-Poisson photon statistics around threshold. Carrier de-pinning accompanies photon fluctuations as demonstrated by Fig. 3.6 (b). Figure 3.6 (d) shows enhanced spontaneous emission across threshold resulting from the extra carriers contributed by carrier de-pinning. An explanation of lasing suppression, enhanced spontaneous emission and de-pinning of carriers may be found in the time-domain data illustrated in Fig. 3.5 (c). The system fails to lase continuously in this region and switches between the lasing and non-lasing state. Once the system shuts down, it waits for the next spontaneous emission event to re-initiate lasing. Lasing, being predominantly a stimulated process, requires the presence of photons in the cavity. A larger active volume with a larger number of electrons has more spontaneous emission events which prevents lasing shut down. A smaller active volume, with lesser likelihood of such events, experiences suppression of continuous lasing. Lasing shut down is accompanied by de-pinning of carriers which in turn enhances spontaneous emission.

3.3 Master equations

The predictions of the biased random walk technique can be verified independently by use of coupled deterministic differential equations that quantize particle number. Previously, such master equations have been solved to explore steady-state behavior in the

limit of cavity quantum electrodynamics for which $\beta = 1$ [Ref.[36, 16]]. Biased random walk trajectories in (n, s) space can be used to sample solutions of master equations.

The equation describing time evolution of probability $P_{n,s}$ of states (n, s) in a single-mode semiconductor laser diode with photon emission at energy $\hbar\omega$ is of the form

$$\begin{aligned}\frac{dP_{n,s}}{dt} = & - \kappa(sP_{n,s} - (s+1)P_{n,s+1}) - (sG_nP_{n,s} - (s-1)G_{n+1}P_{n+1,s-1}) \\ & - (sAP_{n,s} - (s+1)AP_{n-1,s+1} - \beta B(n^2P_{n,s} - (n+1)^2P_{n+1,s-1}) \\ & - (1-\beta)B(n^2P_{n,s} - (n+1)^2P_{n+1,s}) - \frac{I}{e}(P_{n,s} - P_{n-1,s})\end{aligned}$$

where the active volume is V and the device is driven by current I. The term $-\beta Bn^2P_{n,s}(t)$ describes spontaneous emission of photons involving transitions from state (n, s) to state $(n-1, s+1)$ where $B = B'/V$ and B' is the spontaneous emission coefficient. $-sG_nP_{n,s}(t)$ describes stimulated emission of photons from state (n, s) to state $(n-1, s+1)$ where G_n is the stimulated emission coefficient. $-(1-\beta)Bn^2P_{n,s}(t)$ is the decay of electrons into non-lasing photons via transitions from state (n, s) to state $(n-1, s)$. $-IP_{n,s}(t)$ corresponds to injection of electrons causing transitions from state (n, s) to state $(n+1, s)$. $-AsP_{n,s}(t)$ is stimulated absorption of photons involving transitions from state (n, s) to state $(n+1, s-1)$ where A is the stimulated absorption coefficient. $-\kappa sP_{n,s}(t)$ describes the decay of cavity photons in which transitions from state (n, s) to state $(n, s-1)$ occur, where κ is the optical loss coefficient.

The time evolution of $P_{n,s}$ can be solved by integrating Eq.(3.3.1). $P_{n,s}$ may also be solved under steady-state conditions by truncating the system at values of n and s which are much larger than the steady-state mean values predicted by the continuum mean-field rate equations [Ref.[36, 16]]. The equations governing the mean behavior are derived by averaging the master equations over all possible states, after multiplying by n and s. This gives

$$\frac{d\langle n\rangle}{dt} = -B\langle n^2\rangle - \frac{a\Gamma c}{Vn_{\rm r}}\langle (n-n_0)s\rangle + \frac{I}{e}, \tag{3.3.1}$$

$$\frac{d\langle s\rangle}{dt} = \beta B\langle n^2\rangle + \frac{a\Gamma c}{Vn_{\rm r}}\langle (n-n_0)s\rangle - \kappa\langle s\rangle, \tag{3.3.2}$$

which reduces to the standard continuum mean-field rate equations if the correlations factorize such that $\langle (n-n_0)s\rangle = \langle (n-n_0)\rangle\langle s\rangle$ and $\langle n^2\rangle = \langle n\rangle^2$. The second approximation is valid in the case of narrow symmetric single peaked distributions in n. A system involving a small number of particles, experiences strong fluctuations in particle number and correlations between n and s are significant. Hence, such mean-field approximations are not valid, leading to predictions of mean behavior that are different from a more complete probabilistic picture.

Figure 3.7 illustrates some of the essential differences by showing the results of calculating the steady-state characteristics with master equations (M.E.) and continuum mean-field rate equations (R.E). The $\langle ns\rangle$ correlation differs most from its factorized product $\langle n\rangle\langle s\rangle$ around threshold (Fig. 3.7 (d)) and the master equations accounting for these correlations differs significantly in its predictions. In particular it leads to suppression of lasing by increasing the apparent threshold current (Fig. 3.7 (a)) and de-pinning of carriers (Fig. 3.7 (b)). Assuming the value of current at the Fano-factor peak may be used as a measure of laser threshold [Ref.[39]], Fig. 3.7 (c) gives a threshold $I_{\rm th} = 45\ {\rm nA}$ which is 4.5 times greater than the value of $I_{\rm th} = 10\ {\rm nA}$ predicted by continuum mean-field rate equations. The differences reduce as one scales to a larger number of particles in the limit of conventional laser operation and this was indeed verified by master equation calculations performed for a system with parameters similar to Fig. 3.7 but with a higher value of β. Figures 3.7 (e) and (f) show the probability distribution of photons P_s and electrons P_n for different stages of laser operation. At low injection currents P_s is

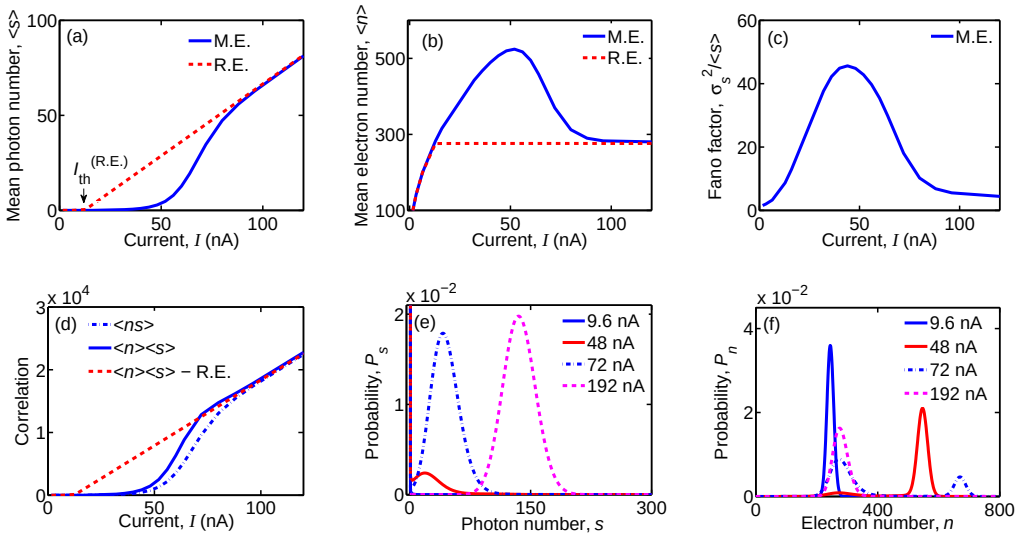

Figure 3.7: Steady-state characteristics. (a) Calculated mean photon number as a function of current showing that master equations (M.E.) predict suppression of lasing threshold relative to continuum mean-field rate equation (R.E.) calculations. Suppression in lasing is due to quantum fluctuations. (b) Calculated mean electron number as a function of current. M.E. show carrier de-pinning due to quantum fluctuations. (c) Fano-factor $F = \sigma_s^2 / < s >$ as a function of current, I. (d) Electron-photon correlation and product of means versus current. (e) Probability of photons for different currents. (f) Probability of electrons for different currents. Parameters as in Fig. 5.

bimodal with a large probability for occupation of the photon ground-state, $s = 0$. This indicates that quantum fluctuations cause lasing emission to turn off. The probability distribution for P_s and P_n near $I_{\rm th}$ is bimodal confirming the existence of the two characteristic system states. Only when $I \gg I_{\rm th}$ do P_s and P_n become single-peaked. The probability distribution for these injection currents obtained from the master equations are in agreement with results of the trajectory method shown in Fig. 3.5. In the long-time limit, trajectories in the (n, s) plane are found to converge to the predictions of the master equations (Fig. 3.8).

Computational convenience dictates the choice of parameters used for solving the master equations. Realistic parameters increase number of particles which in turn leads to a large number of probability states. For total number of particles N, the number of

probability states is $D = (N+1)(N+2)/2$ and this grows as N^2 for large N. For $N = 1000$ the probability vector has a length 0.5×10^6 . Matrix inversion for steady-state calculation and multiplication for time evolution becomes difficult when the size of the coefficient matrix (D^2) increases significantly beyond this value.

Despite the use of small values of n and s, the underlying physics in which quantum fluctuations suppress lasing and carriers are de-pinned remain. This is confirmed by calculations using the trajectory method which was developed to connect with large systems described by realistic parameters. The technique verifies master equation results and predicts similar behavior in small systems with experimentally accessible parameters (see Section 3.5).

Similar to the trajectory method, the master equations can be modified to include spontaneous emission of photons into a non-lasing channel. The spontaneous emission channel does not participate in any stimulated processes and so avoids the correlation effects that strongly influences lasing emission. The master equation for probability $P_{n,s,s''}(t)$ is (4) with additional terms $(1-\beta)Bn^2P_{n,s,s''}$ corresponding to decay of electrons into photons of the non-lasing channel, causing a transition from state (n, s, s'') to $(n-1, s, s''+1)$ and $\kappa s'' P_{n,s,s''}$ denoting decay of non-lasing photons, causing a transition from state (n, s, s'') to $(n, s, s''-1)$. The average value for n and s obtained using $P_{n,s,s''}(t)$ gives equations Eqs.(3.3.1) respectively. The average for s'' is

$$\frac{d\langle s''\rangle}{dt} = (1-\beta)B\langle n^2\rangle - \kappa\langle s''\rangle \tag{3.3.3}$$

Large fluctuations and correlations in particle number in the finite sized quantum system lead to carrier de-pinning near threshold and the increased average number of carriers results in enhanced spontaneous emission because of the $(1-\beta)Bn^2$ dependence. This

is verified by the trajectory method (Fig. 3.6 (d)). A similar plot using master equation calculations is avoided for numerical reasons. The system has a larger number of probability states due to the presence of this additional channel of spontaneously emitted photons. However a similar idea may be demonstrated by studying the role of β in distributing the total emission between two modes. Larger β enhances spontaneous emission into the lasing mode and prevents lasing shut down. Reducing β has the opposite effect. Figure 3.8 demonstrates this for a small active volume. As β is reduced, while keeping the current constant, the emission switches from being dominated by lasing to spontaneous emission. This leads to lasing suppression. The peak at higher electron number in the bimodal distribution corresponding to zero lasing photons gives rise to enhanced spontaneous emission. The distribution of spontaneous emission as shown in Figs. 3.8 (c) and (d) is symmetric in the absence of diagonal processes illustrated in the state diagram shown in Fig. 3.3. The active volumes used for calculations whose results are shown in Figs. 3.8 (a - d) are chosen for computational convenience. The same calculations have been repeated using the trajectory method for a larger system and a similar behavior is observed with change of β.

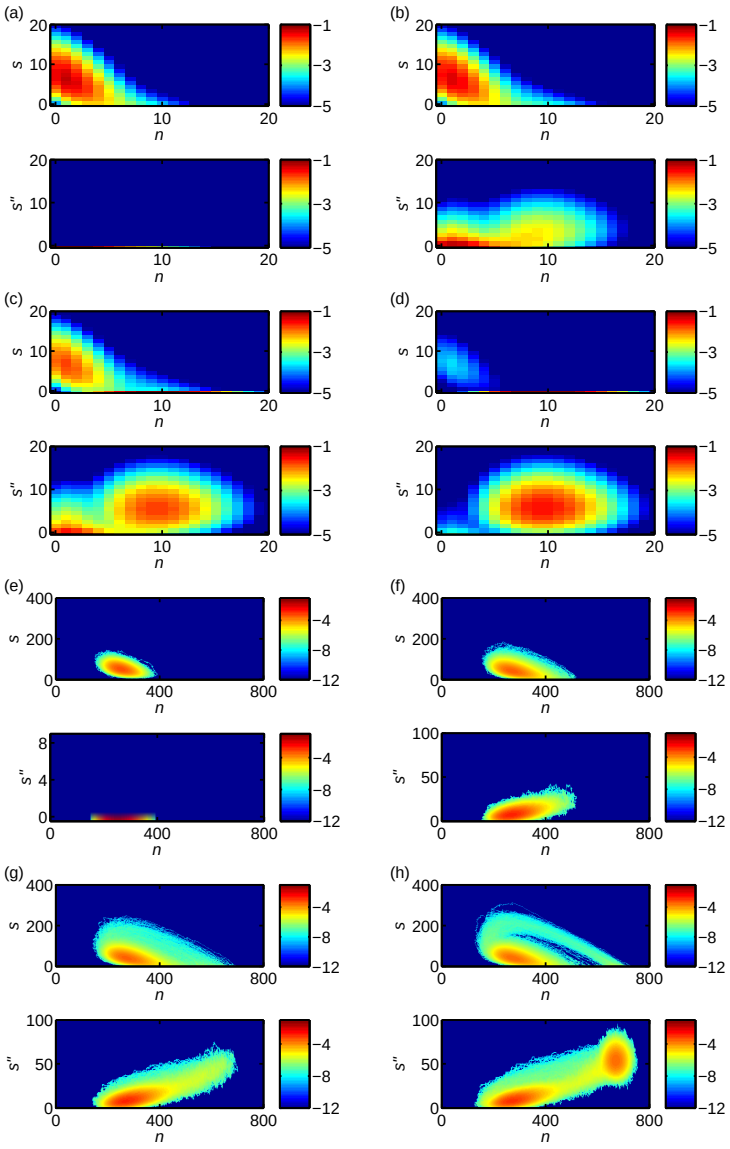

Figure 3.8: Steady-state probability distribution for electrons (n), photons (s), spontaneous emission (s'') for different values of β and a fixed current I = 10 electron/ns (= 1.6 nA) for (a), (b), (c), and (d) and 72 nA for (e), (f), (g), and (h). (a) and (e) $\beta = 1$. (b) and (f) $\beta = 10^{-1}$. (c) and (g) $\beta = 10^{-2}$. (d) and (h) $\beta = 10^{-4}$. Parameters for (a), (b), (c), and (d) are as in Fig. 5 but with $V = (1\ \mu\mathrm{m} \times 1\ \mathrm{nm} \times 1\ \mathrm{nm})$ and $\alpha_i = 0.19\ \mathrm{cm}^{-1}$. Parameters for (e), (f), (g), and (h) are as in Fig. 5. The color (gray) scale is $\log_{10}$.

3.4 Transient dynamics in small lasers

To solve the transient master equation the entire time-evolution is divided into equal time intervals, the duration of which is determined by the inverse of the pumping rate. This allows only a single electron to enter the active volume on average in a given time interval. If we start with an empty device, i.e. $P_{0,0}(t = 0) = 1$, the terms which will be important in the first time interval are $P_{0,0}, P_{0,1}, P_{1,0}$. This happens because a system of n electrons and s photons can only undergo processes and make single quantum transitions as described in Fig. 3.3. In matrix form, the process is described as follows: The coupled first order differential equations written in matrix form is

$$\begin{bmatrix} \dot{P_{00}} \\ \dot{P_{01}} \\ \dot{P_{10}} \end{bmatrix} = \begin{bmatrix} -\frac{I}{e} & \kappa(1) & (1-\beta)B1^2 \\ 0 & -\kappa(1) - A(1) & \beta B1^2 \\ \frac{I}{e} & A(1) & -B1^2 \end{bmatrix} \begin{bmatrix} P_{00} \\ P_{01} \\ P_{10} \end{bmatrix} \tag{3.4.1}$$

We integrate the set of master equations involving these terms using the fourth-order Runge-Kutta method for the first interval. Only one electron is introduced in this interval. It may be introduced uniformly over the period of this interval starting from the cold cavity initial condition $P_{00} = 1$ and under the influence of the pump as in the current case. It can also be introduced at a random particular instant in the interval. This method of injection does not alter the steady state finally attained by this technique and helps in truncating the infinite coupled set of differential equations into a finite set, containing variables which are important in the first interval. In the next interval the maximum

number of particles is 2. So terms such as $P_{1,1}, P_{0,2}, P_{2,0}$ will be important along with the terms of the previous interval. So in matrix form we have,

$$\begin{bmatrix} \dot{P_{00}} \\ \dot{P_{01}} \\ \dot{P_{10}} \\ \dot{P_{02}} \\ \dot{P_{11}} \\ \dot{P_{20}} \end{bmatrix} = \begin{bmatrix} -\frac{I}{e} & \kappa & (1-\beta)B & 0 & 0 & 0 \\ 0 & -\kappa - A - \frac{I}{e} & \beta B & 2\kappa & (1-\beta)B & 0 \\ \frac{I}{e} & A & -B - \frac{I}{e} & 0 & \kappa & 4(1-\beta)B \\ 0 & 0 & 0 & -2(\kappa - A) & G_1 + \beta B & 0 \\ 0 & \frac{I}{e} & 0 & 2A & -\kappa - G_1 - B & 4(1-\beta)B \\ 0 & 0 & \frac{I}{e} & 0 & A & 4(1-\beta)B \end{bmatrix} \begin{bmatrix} P_{00} \\ P_{01} \\ P_{10} \\ P_{02} \\ P_{11} \\ P_{20} \end{bmatrix} \tag{3.4.2}$$

At the time of inclusion in the matrix the new terms P_{02}, P_{11} and P_{20} have value zero. They evolve due to their coupling with the existing elements P_{00}, P_{01} and P_{10} in the next interval. Note that the probabilities with the maximum number of total particles, $N = n + s$ in a given interval, is not allowed to transition to a state with another extra excitation. With the addition of the n^{th} electron, $n + 1$ additional probability states are added and the coefficient matrix grows as D^2. In matrix form

$$
\begin{bmatrix} \dot{P_{00}} \\ \dot{P_{01}} \\ \dot{P_{10}} \\ \dot{P_{02}} \\ . \\ . \\ \dot{P_{n-1,1}} \\ \dot{P_{n0}} \end{bmatrix} =
$$

$$
\begin{bmatrix}
-\frac{I}{e} & \kappa.1 & (1-\beta)B.1^2 & 0 & .. & 0 & 0 \\
0 & -\kappa.1 - A.1 - \frac{I}{e} & \beta B.1^2 & \kappa.2 & .. & 0 & 0 \\
\frac{I}{e} & A.1 & -B.1^2 - \frac{I}{e} & 0 & .. & 0 & 0 \\
0 & 0 & 0 & -\kappa.2 - A.2 & .. & 0 & 0 \\
. & . & . & . & . & . & . \\
0 & 0 & 0 & 0 & .. & . & (1-\beta)Bn^2 \\
0 & 0 & 0 & 0 & .. & A.1 & -Bn^2
\end{bmatrix}
\begin{bmatrix} P_{00} \\ P_{01} \\ P_{10} \\ P_{02} \\ . \\ P_{n-1,1} \\ P_{n0} \end{bmatrix}
\tag{3.4.3}
$$

The system of equations is such that total probability is conserved in every step as more electrons enter the system. Iterations are continued by adding more particles until the system attains a steady-state probability distribution. The steady-state attained agrees with the one obtained from the truncated master equations solved under steady-state conditions. For a given interval the process is similar to a continuous-time Markov process where the allowed states are the states of continuous-time Markov chains. So in every step the size of the matrices grow. In MATLAB, construction of these matrices, specifically the coefficient matrix in the differential equations is time consuming. Comparison of the above matrix equations show that certain parts of the matrix remain

unchanged, few get modified (by addition of extra terms) and completely new terms are added in the new rows and columns introduced in every consecutive step to accommodate an extra particle. For example in Eqn (3.4.1) and Eqn (3.4.2), the term C_{11} of the coefficient matrix stays unchanged, C_{33} increases due to addition of the pump term and new coefficients are added for the new equations in row and column (4-6). Since we are only dealing single particle excitation or processes, equations of N particles are related to those of $N+1$ and $N-1$. So introduction of a new particle only influences the very last set of equations. This knowledge is used to make the algorithm faster. The unchanged part of the matrix or vector is kept the same, and new parts are appended. So only $n+1$ additional rows and columns are added to a matrix instead of constructing

the total matrix of size D^2. The state vectors containing the probability elements are arranged in the following order,

$$\begin{bmatrix} P_{00} \\ P_{01} \\ P_{10} \\ P_{02} \\ P_{11} \\ P_{20} \\ . \\ . \\ P_{0,n} \\ p_{1,n-1} \\ . \\ . \\ P_{n-2,2} \\ P_{n-1,1} \\ P_{n0} \end{bmatrix} \tag{3.4.4}$$

So we see for N total particles, there are $N + 1$ total states, for which $N = n + s$. The photon number is reduced from N to zero in steps of 1, and the excitation number is correspondingly increased, as the probability states P_{ns} are arranged vertically in a matrix. As mentioned, equations for a system of N particles only connects to the equation for $N + 1$ and $N - 1$ particles. The specific ordering of the vector elements, helps in allocating the coefficients in their equations. In allocating the coefficient matrix, each element P_{ns} is considered and the corresponding row is filled with the coefficients of its equation. The arrangement helps save time in building these matrices instead of

employing a search algorithm to find the position along the row where the coefficient should be placed. For example, due to the arrangement, the terms $P_{n-1,s+1}$, $P_{n,s}$ and $P_{n+1,s-1}$ are adjacent. Hence, the positions of the coefficients for stimulated absorption, stimulated emission and spontaneous emission into the lasing mode can be exactly determined, as the flow of probability in these processes are between the above mentioned states only. The cavity loss term, the non-lasing mode spontaneous emission term and the pump term, which reduces the total particle number N by 1, are located $N+1 = n+s+1$ elements away (left if decreasing, right if increasing) from the element with $n + s = N$ particles, P_{ns}. Look for example the allocation of the allowed coefficients of the equation for P_{11} in Eq.(3.4.2) when the second particle is introduced. The elements corresponding to the different physical processes influencing P_{11} are located in the coefficient matrix in the way stated above.

As mentioned earlier, the terms with the maximum particle number, N, in a given matrix is not allowed to be pumped any higher. So when the $N + 1$ particle is added the equations for the N particles are modified. The pump loss is included in the equations for the N particles, specifically in the self-term. If P_{ns} is located in the n^{th} row then this the coefficient, C_{nn} in the coefficient matrix. This term includes coefficients of loss terms from the state P_{ns} representing flow of probability out of the state. A specific example of this is the case of the 1 and 2 excitation particle case shown previously where the term C_{33} gets modified on adding the 2^{nd} particle after the 1^{st} one.

The technique for the steady state solution is similar. From Eqn (3.4.3), in steady state we have

$$\begin{bmatrix} 0 \\ 0 \\ 0 \\ 0 \\ 0 \\ 0 \\ 0 \end{bmatrix} =$$

$$\begin{bmatrix} -\frac{I}{e} & \kappa.1 & (1-\beta)B.1^2 & 0 & .. & 0 & 0 \\ 0 & -\kappa.1 - A.1 - \frac{I}{e} & \beta B.1^2 & \kappa.2 & .. & 0 & 0 \\ \frac{I}{e} & A.1 & -B.1^2 - \frac{I}{e} & 0 & .. & 0 & 0 \\ 0 & 0 & 0 & -\kappa.2 - A.2 & .. & 0 & 0 \\ . & . & . & . & . & . & . \\ 0 & 0 & 0 & 0 & .. & . & (1-\beta)Bn^2 \\ 0 & 0 & 0 & 0 & .. & A.1 & -Bn^2 \end{bmatrix} \begin{bmatrix} P_{00} \\ P_{01} \\ P_{10} \\ P_{02} \\ . \\ P_{n-1,1} \\ P_{n0} \end{bmatrix} \tag{3.4.5}$$

This is a set of linear homogenous algebraic equations in the steady-state probabilities. The non-triviality of the solution can be fixed by the conservation of probability. We know that if one equation is removed, the rest are independent. We remove the last equation and use the condition of probability conservation to calculate the steady-state

value. Of course the value of n for which the equations are truncated should be much greater than the steady-state rate equation predictions.

$$\begin{bmatrix} 0 \\ 0 \\ 0 \\ 0 \\ 0 \\ 0 \\ 1 \end{bmatrix} = \begin{bmatrix} -\frac{I}{e} & \kappa.1 & (1-\beta)B.1^2 & 0 & .. & 0 & 0 \\ 0 & -\kappa.1 - A.1 - \frac{I}{e} & \beta B.1^2 & \kappa.2 & .. & 0 & 0 \\ \frac{I}{e} & A.1 & -B.1^2 - \frac{I}{e} & 0 & .. & 0 & 0 \\ 0 & 0 & 0 & -\kappa.2 - A.2 & .. & 0 & 0 \\ . & . & . & . & . & . & . \\ 0 & 0 & 0 & 0 & .. & . & (1-\beta)Bn^2 \\ 1 & 1 & 1 & 1 & 1 & 1 & 1 \end{bmatrix} \begin{bmatrix} P_{00} \\ P_{01} \\ P_{10} \\ P_{02} \\ . \\ P_{n-1,1} \\ P_{n0} \end{bmatrix} \tag{3.4.6}$$

Note that the last equation states conservation of probabilities.

Figures 3.9 (a) and (b) show the time evolution of $\langle n \rangle$ and $\langle s \rangle$ for a small laser operating above threshold. Factorization of the correlation $\langle ns \rangle$ is not appropriate as reflected by the fact that the continuum mean-field rate equation results do not converge to the master equation solution. Figures 3.10 (b) and (c) show that at any point in time the instantaneous probability $P_{n,s}$ carries information about the path taken. In contrast, averaging in the continuum mean-field rate-equation calculation removes information about the system's history.

Strong correlations and fluctuations affect the average response of a small laser to a step change in injection current and slows down the system in general. Increasing the active volume, keeping other parameters fixed reduces the difference with the mean-field predictions (Fig. 3.9 (c) and (d)).

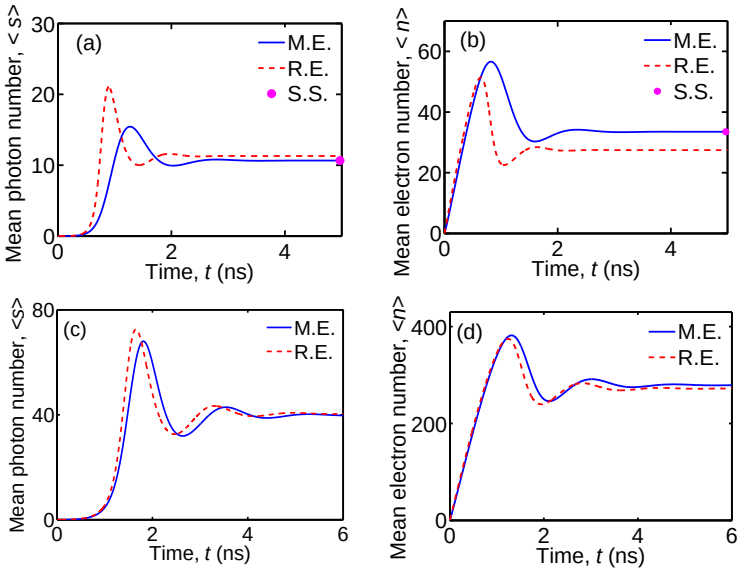

Figure 3.9: Transient behavior of mean electron number and photon number for a step change in current from $I(t<0)=0$ to $I(t\geq 0)$ = 100 electrons/ns (= 16 nA) for (a, b) and $I(t\geq 0)$ = 400 electrons/ns (= 64 nA) for (c, d). (a) Mean photon number as a function of time. (b) Mean electron number as a function of time. The dot at the last time point denotes the mean calculated from the probability distribution obtained by the steady-state technique. Parameters as in Fig. 5 but with $V=(0.1\ \mu\mathrm{m}\times 10\ \mathrm{nm}\times 10\ \mathrm{nm})$ and $\beta=10^{-1}$. (c) Mean photon number as a function of time. (d) Mean electron number as a function of time. Parameters as in Fig. 5 but with $\beta=10^{-1}$.

3.4.1 Large signal analysis

A large signal analysis may be performed by starting from the system ground-state and observing the response to a step change in injection current. The time delay, t_{d} may be calculated by starting from an empty device $(n,s=0)$ and noting the time taken to reach half the steady-state photon number. The mean time, $\langle t_{\mathrm{d}}\rangle^{\mathrm{MC}}$ calculated by

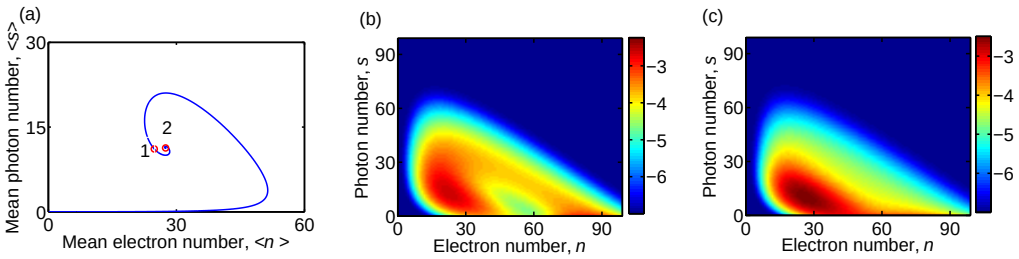

Figure 3.10: Transient behavior of mean electron number and photon number for a step change in current from $I(t<0)=0$ to $I(t\geq 0)$ = 100 electrons/ns (= 16 nA). (a) Evolution of mean photon number as a function of mean electron number, calculated from continuum mean-field rate equations. (b) $P_{n,s}$ calculated at time $t = 1.25$ ns and indicated by arrow labeled 1 in (a). (c) $P_{n,s}$ calculated at time $t = 5$ ns and indicated by arrow labeled 2 in (a). Parameters as in Fig. 5 but with $V = (0.1\ \mu\text{m} \times 10\ \text{nm} \times 10\ \text{nm})$ and $\beta = 10^{-1}$. The color (gray) scale is $\log_{10}$.

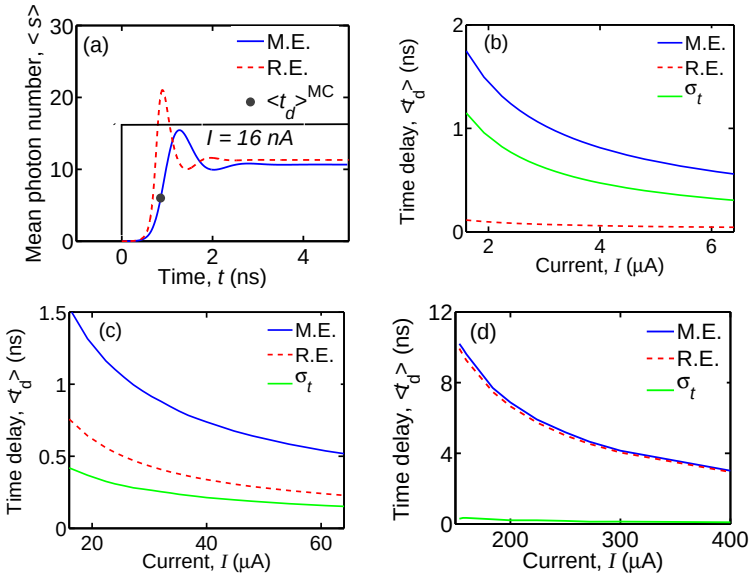

Figure 3.11: Comparison of time delay, $t_{\rm d}$ between continuum mean-field rate equations and random walk approach. (a) Transient behavior of mean photon number for a step change in current from $I(t<0)=0$ A to $I(t\geq 0)=16$ nA. Time delay $\langle t_{\rm d}\rangle$ comparison for (b) $V=5\times10^{-4}\ \mu\text{m}^3$, (c) $V=5\times10^{-2}\ \mu\text{m}^3$ (d) $V=5\ \mu\text{m}^3$. Parameters: (a) $V=(0.1\ \mu\text{m}\times10\ \text{nm}\times10\ \text{nm})$, $\Gamma=0.25$, $a=2.5\times10^{-18}\ \text{cm}^2\ \text{s}^{-1}$, $B'=10^{-10}\ \text{cm}^3\ \text{s}^{-1}$, $n_0=10^{18}\ \text{cm}^{-3}$, $\alpha_i=1\ \text{cm}^{-1}$, $n_{\rm r}=4$, $r=1-10^{-6}$, $\beta=10^{-1}$. (b) $V=(5\ \mu\text{m}\times0.01\ \mu\text{m}\times0.01\ \mu\text{m})$, $\Gamma=0.25$, $a=2.5\times10^{-16}\ \text{cm}^2\ \text{s}^{-1}$, $B'=10^{-10}\ \text{cm}^3\ \text{s}^{-1}$, $n_0=10^{18}\ \text{cm}^{-3}$, $\alpha_i=10\ \text{cm}^{-1}$, $n_{\rm r}=4$, $r=0.999$, $\beta=10^{-4}$. (c) $V=(5\ \mu\text{m}\times0.1\ \mu\text{m}\times0.1\ \mu\text{m})$, other parameters same as in (b). (d) $V=(5\ \mu\text{m}\times1\ \mu\text{m}\times1\ \mu\text{m})$, other parameters same as in (b).

averaging, $t_{\rm d}$, for multiple trajectories obtained using the trajectory method, is found to be in close agreement with that predicted by master equations. This is denoted by the dot in Fig. 3.11 (a) which shows the agreement and a mean time-delay $\langle t_{\rm d} \rangle^{\rm MC}$ that is greater than the predictions of the continuum mean-field rate equation theories, $\langle t_{\rm d} \rangle^{\rm RE}$. These calculations are carried out for injection currents which support continuous lasing and hence are far away from the fluctuation dominated regime (Fig. 3.5 (c)). The peak of the Fano-factor for the lasers considered in Fig. 3.11 (b), (c), and (d) occur around 0.6 μA, 8 μA, and 150 μA respectively and injection current chosen for this analysis is higher than that. The Fano-factor peak gives an estimate of the threshold for these small devices [Ref.[39]]. Figures 3.11 (b), (c), and (d) show a comparison of time delay for three different active volumes and convergence with continuum mean-field rate equations is achieved for the largest volume (d). The deviation from the mean-field calculations reduces with increase in active volume size.

3.4.2 Small-signal analysis

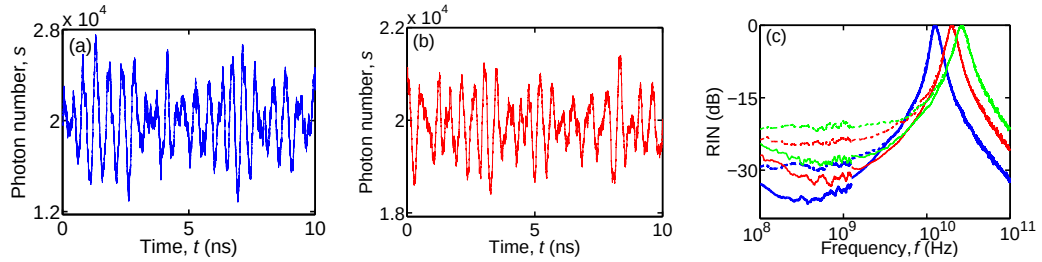

Figure 3.12: (a) Time trajectory calculated using the random walk technique. (b) Time trajectory from the Langevin equations using correlated noise sources. (c) Relative intensity noise (RIN) as a function of frequency. Calculation using Langevin equations (dashed line), random walk calculation (solid line). Calculations are normalized to peak in spectrum. Electron injection current = 400 μA (dark curve), 800 μA (gray curve), 1.32 mA (light gray curve). Parameters same as Fig. 3.11(d).

Above threshold the biased random walk trajectory in the time domain (Fig. 3.5 (d)) appears similar to the trajectories produced by Langevin equations as described in [Ref.[37]]. The Fourier transform of this data is computed to obtain small-signal relative intensity noise (RIN) data. Such time-domain analysis is not possible using master equations.

Figures 3.12 (a) and (b) show the time-trajectories calculated using our trajectory method and Langevin equations respectively. The fluctuations in photon number is noticeably larger in Fig. 3.12 (a) compared to (b). Our trajectory calculations show larger fluctuations and hence larger Fano-factors and this trend is observed in smaller active volume lasers as well.

The Langevin equations consider correlated noise terms which are artificially forced to be Gaussian in nature. This gives rise to considerably lower values of Fano-factor in the threshold region. The Langevin approach arbitrarily assumes near Poisson distributions which is physically unrealistic in the correlated system we consider. The distributions obtained from the trajectory technique are not biased to be Gaussian and are, in fact, super-Poissonian with a much larger Fano-factor even when the system is

lasing continuously. For example, for a current of 400 μA which is 2.7 times threshold current, Langevin equations give a Fano-factor of about 12 and our trajectory method gives a Fano-factor of near 270.

The response in the frequency domain was compared with the RIN data obtained from Langevin equations with cross-correlated noise sources [Ref.[37]]. The frequency response calculated using the two models agrees around the RIN peak and when the system is in the lasing state (Fig. 3.12 (c)). The peak in frequency increases with electron injection current. There are, however, differences at frequencies below the RIN peak. These can be brought into closer agreement by increasing the magnitude of the Langevin noise terms. The calculations involving large data sets of time trajectories required for the Fourier transforms can be conveniently handled by parallel computing, where each processor performs calculation on a section of the data set. It integrates that section of the data for all frequencies and in the end the processors can combine their data to get the Fourier transform for all frequencies.

3.5 Experimental Design

The behavior of lasers with very small active volumes can be studied using semiconductor nanowire [Ref.[40]], quantum pillar [Ref.[41]], or other geometries [Ref.[42, 43]]. The active medium may be confined inside a high-Q photonic crystal or other optical cavity. Reducing the size of the laser is generally accompanied by an increase in β. However, small β is an important factor leading to lasing suppression and might explain why suppression of lasing by quantum fluctuations has not been observed in experiments.

We have performed calculations to find experimentally accessible conditions where the impact of quantum fluctuations on laser performance may be observed. Figure 3.13

(a) and (b) shows calculations for a system of three nano-wires confined in a photonic crystal medium. Parameters chosen are similar to those considered by [Ref.[40]]. The lasing suppression is seen to disappear with the increase in β. The carrier de-pinning effect however persists longer and can be observed in spontaneous emission. So one of the key directions for design is to have strong confinement for the single lasing mode along with significant emission into the non-lasing modes. For a nano-wire system this would mean strong confinement in the axial direction for the laser mode with spontaneous emission in the lateral directions. Reduction in β by increasing the optical cavity length is also considered in Fig. 3.13 (c) and (d). Other than an overall change in the threshold value, these laser designs show a similar trend with change of β.

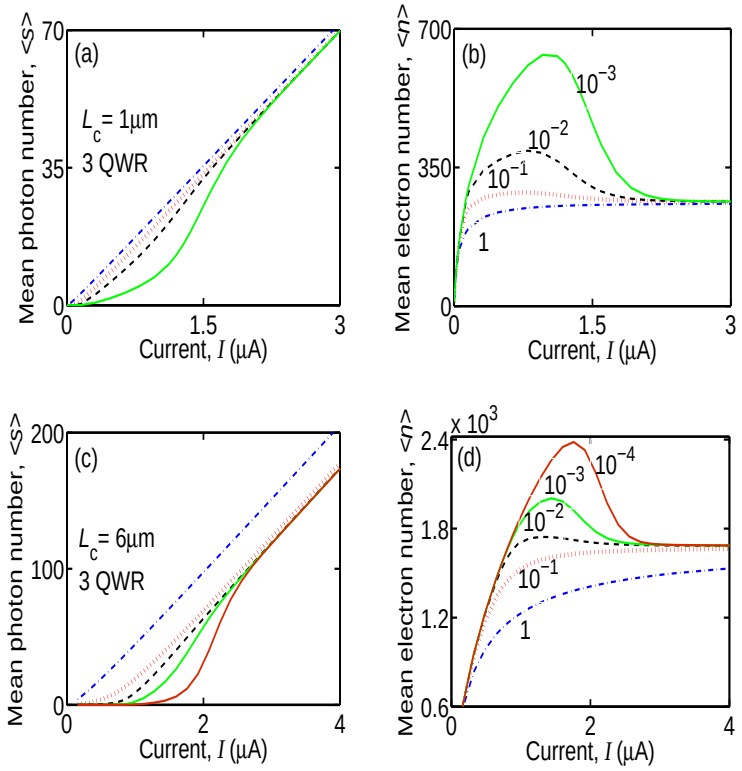

Figure 3.13: Comparison of steady-state characteristics for different β values. $\beta = 10^{-3}$ (solid), $\beta = 10^{-2}$ (dashed), $\beta = 10^{-1}$ (dot), $\beta = 1$ (dash-dot). $\beta = 10^{-4}$ (solid - dark line) is included in (c) and (d) for a larger size cavity. The graphs display random trajectory calculations. Parameters for (a) and (b) : $V = 3 \times (1\ \mu\text{m}\ \times 5\ \text{nm}\ \times 5\ \text{nm})$, $\Gamma = 0.01$, $a = 12.3 \times 10^{-16}\ \text{cm}^2\ \text{s}^{-1}$, $B' = 5.5 \times 10^{-10}\ \text{cm}^3\ \text{s}^{-1}$, $A_{\text{nr}} = 0.91 \times 10^9\ \text{s}^{-1}$, $C = 0.5 \times 10^{-29}\ \text{cm}^6\ \text{s}^{-1}$, $n_0 = 10^{18}\ \text{cm}^{-3}$, $\alpha_i = 0.0010\ \text{cm}^{-1}$, $n_{\text{r}} = 3.5$, $r = 0.997$, $\epsilon = 0.01 \times 10^{-18}\ \text{cm}^3$. Parameters for (c) and (d) : $V = 3 \times (6\ \mu\text{m}\ \times 5\ \text{nm}\ \times 5\ \text{nm})$, $\Gamma = 0.004$, $\alpha_i = 5\ \text{cm}^{-1}$, $r = 0.995$, others same as in (a) and (b). Net optical output power in μW at an operating wavelength of 1310 nm may be determined by multiplying the photon number by 0.039 for (a) and (b), 0.0109 for (c) and (d).

The threshold current, I_{th} for the laser considered in Fig. 3.13 (c) and (d) is shown in Fig. 3.14 as a function of cavity length, L_{c}. In this case, changing the cavity length alters the active volume. The rate equation data is compared with the random walk trajectory calculation. Only the case with $\beta = 10^{-4}$ is considered. The peak of the Fano-factor is used to locate the threshold current in the random trajectory calculations. Threshold current is larger than the predictions of continuum mean-field rate equations due to lasing

suppression. The light output characteristics of the laser with $L_c = 6$ μm is considered in the inset. This has a threshold current around 2 μA and optical output power is in the μW range. As expected, the pinned carrier number has a linear dependence on the cavity length, L_c.

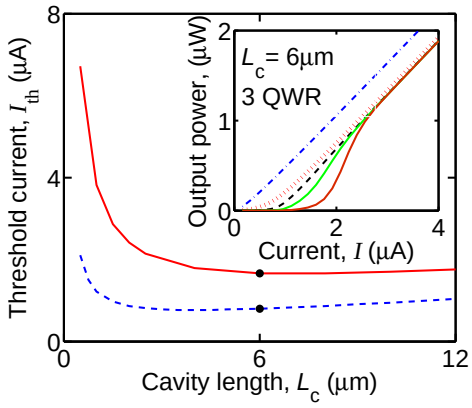

Figure 3.14: Variation of threshold current with cavity length. Upper curve (solid) are results of random trajectory calculations and lower curve (dashed) are results of continuum mean-field rate equation calculations. $\beta = 10^{-4}$ for main figure. Inset is comparison of steady-state characteristics for different β values. $\beta = 10^{-4}$ (solid - dark line), $\beta = 10^{-3}$ (solid), $\beta = 10^{-2}$ (dashed), $\beta = 10^{-1}$ (dot), $\beta = 1$ (dash-dot). This is the same plot as Fig. 3.13 (c) but in terms of output power for an operating wavelength of 1310 nm. Parameters same as in Fig. 3.13 (c).

Fig. 3.15 is a plot of steady-state characteristics using a $\log_{10}$ scale. These correspond to the linear plot of Fig. 3.13 (c). Strong quantum fluctuations around threshold smooth the non-lasing to lasing transition compared to a more abrupt cross-over predicted by the continuum mean-field theories. This is seen for the small β cases where the effects of lasing suppression becomes apparent.

3.6 Conclusion and outlook

In conclusion, our calculations illustrate the importance of quantum fluctuations in determining the steady-state and transient response of a laser when there are a small

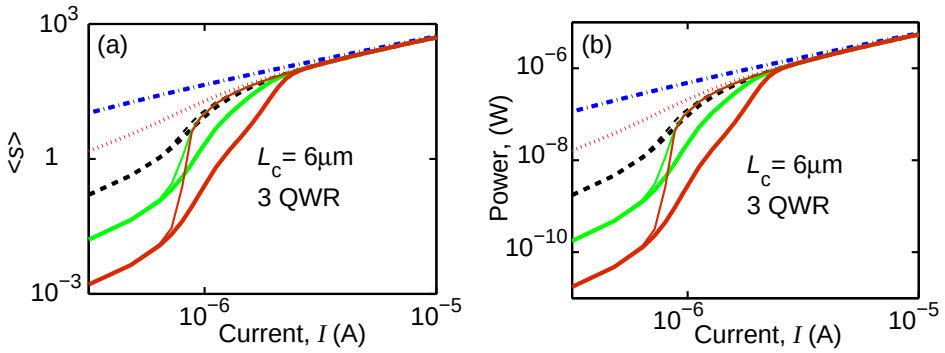

Figure 3.15: Comparison of steady-state characteristics for different β values. $\beta = 10^{-4}$ (solid - dark line), $\beta = 10^{-3}$ (solid), $\beta = 10^{-2}$ (dashed), $\beta = 10^{-1}$ (dot), $\beta = 1$ (dash-dot). Thicker lines are results of random walk calculation, thinner lines are from the continuum mean-field calculations. (a) Intra-cavity mean photon number, (b) output optical power versus injection current. Parameters same as in Fig. 3.13 (c) and (d).

number of particles in the system. Quantum fluctuations can suppress lasing threshold, enhance spontaneous emission, and create a non-Poisson probability distribution for n discrete excited electronic states and s discrete photons. Correlations between n and s are found to damp the average dynamic response of laser emission. Fluctuations in the finite sized quantum system behave differently from lasers in the thermodynamic limit. According to the conventional Landau-Ginzburg theory of phase transitions, fluctuations in the large particle number limit will enhance lasing below threshold. In meso-scale systems the opposite is true, quantum fluctuations suppress lasing.

The master equations and the random walk technique generate statistics of the photon field but do not include phase as they only quantize energy. Phase fluctuations contain information about line-width of the lasing mode. Inclusion of phase in a fully quantum mechanical model solved by brute-force methods is challenging due to the extremely large state-space for the system. A possible approach is to solve for a few atoms in the optical cavity and then attempt to develop techniques capable of solving the problem for larger numbers of particles based on the physical insight gained. This approach is adopted in making a connection with the semi-classical predictions, in the

next two chapters. The exact solution of the quantum mechanical problem of a few emitters and photons though cumbersome is manageable computationally. The solutions are compared with the semi-classical random walk calculations. The novel predictions of lasing suppression and carrier de-pinning from the semi-classical theory are recovered in presence of inhomogeneity. New understanding regarding the parameter β, which influences the existence of these new effects in the semi-classical theory is obtained from the full quantum picture. The following chapter consists of a review of the existing quantum theories of atom-field interaction and the useful Hamiltonians and formalisms required for the development of our model.

Chapter 4

Quantum theory of light-matter interaction - a review

4.1 Introduction

This chapter provides a brief review of light-matter interaction from a fully quantum perspective following the work of Sully and Zubairy [Ref. [15]]. Quantization of electromagnetic fields starting from the classical picture is discussed. The Jaynes-Cummings Hamiltonian, describing the interaction of matter with radiation field is derived under the dipole and rotating wave approximations. This Hamiltonian is analytically solvable and is widely used in quantum optics. The closed system of matter and radiation field is generalized to include interactions with external reservoirs in order to describe processes involving loss and pumping. The modification of the density matrix equations, under the inclusion of reservoir terms is discussed. Finally these elements are used to lay out the basic foundations for the quantum theory of lasers. The approximations made in this derivation and the final results of the full quantum theory are discussed and compared with the semi-classical case (see Chapter 1). This chapter explains in detail the approximations made in developing the theory of meso-lasers in Chapter 5 and helps us in distinguishing the meso-case from the ordinary large laser reviewed in this chapter. The notations used in the derivations are similar to the work of Scully and Zubairy [Ref. [15]].

4.2 Quantization of the electromagnetic field

The classical electric and magnetic fields in free space can expanded in terms of a plane wave basis as

$$\mathbf{E}(\mathbf{r},t) = \sum_{\mathbf{k}} \hat{\epsilon_{\mathbf{k}}} \mathcal{E}_{\mathbf{k}} \alpha_{\mathbf{k}} e^{-i\nu_k t + i\mathbf{k}.\mathbf{r}} + \sum_{\mathbf{k}} \hat{\epsilon_{\mathbf{k}}} \mathcal{E}_{\mathbf{k}} \alpha^*_{\mathbf{k}} e^{i\nu_k t - i\mathbf{k}.\mathbf{r}} \tag{4.2.1}$$

$$\mathbf{H}(\mathbf{r},t) = \frac{1}{\mu_0} \sum_{\mathbf{k}} \frac{\mathbf{k} \times \hat{\epsilon_{\mathbf{k}}}}{\nu_k} \mathcal{E}_{\mathbf{k}} \alpha_{\mathbf{k}} e^{-i\nu_k t + i\mathbf{k}.\mathbf{r}} + \frac{1}{\mu_0} \sum_{\mathbf{k}} \frac{\mathbf{k} \times \hat{\epsilon_{\mathbf{k}}}}{\nu_k} \mathcal{E}_{\mathbf{k}} \alpha^*_{\mathbf{k}} e^{i\nu_k t - i\mathbf{k}.\mathbf{r}} \tag{4.2.2}$$

where the summation is over the allowed values of wave vector $\mathbf{k} = (k_x, k_y, k_z)$. $\nu_{\mathbf{k}}$ is the frequency of mode $\mathbf{k}$, $\hat{\epsilon_{\mathbf{k}}}$ is a unit polarization vector, $\alpha_{\mathbf{k}}$ is a dimensionless amplitude and

$$\mathcal{E}_{\mathbf{k}} = (\frac{\hbar \nu_{\mathbf{k}}}{2\epsilon_0 V})^{1/2} \tag{4.2.3}$$

This form of the expansion is obtained by considering a cavity of side L. Periodic boundary conditions are used and so

$$k_x = \frac{2\pi n_x}{L}, k_y = \frac{2\pi n_y}{L}, k_z = \frac{2\pi n_z}{L}, \tag{4.2.4}$$

where n_x, n_y, n_z are integers $(0, \pm 1, \pm 2...)$. A set of numbers (n_x, n_y, n_z) defines a mode of the electromagnetic field. The transverse nature of the field requires

$$\mathbf{k}.\hat{\epsilon_{\mathbf{k}}} = 0 \tag{4.2.5}$$

The radiation field is quantized by replacing the scalar amplitudes, $\alpha_{\mathbf{k}}$ and $\alpha_{\mathbf{k}}^*$ with creation and annihilation operators $a_{\mathbf{k}}^\dagger$ and $a_{\mathbf{k}}$ with commutation relation $[a_{\mathbf{k}}, a_{\mathbf{k}}^\dagger] = 1$. The quantized electric and magnetic fields are of the form

$$\mathbf{E}(\mathbf{r},t) = \sum_{\mathbf{k}} \hat{\epsilon_{\mathbf{k}}} E_{\mathbf{k}} a_{\mathbf{k}} e^{-i\nu_k t + i\mathbf{k}.\mathbf{r}} + \sum_{\mathbf{k}} \hat{\epsilon_{\mathbf{k}}} E_{\mathbf{k}} a_{\mathbf{k}}^\dagger e^{i\nu_k t - i\mathbf{k}.\mathbf{r}} \tag{4.2.6}$$

$$\mathbf{H}(\mathbf{r},t) = \frac{1}{\mu_0} \sum_{\mathbf{k}} \frac{\mathbf{k} \times \hat{\epsilon_{\mathbf{k}}}}{\nu_{\mathbf{k}}} \hat{\epsilon_{\mathbf{k}}} E_{\mathbf{k}} a_{\mathbf{k}} e^{-i\nu_k t + i\mathbf{k}.\mathbf{r}} + \frac{1}{\mu_0} \sum_{\mathbf{k}} \frac{\mathbf{k} \times \hat{\epsilon_{\mathbf{k}}}}{\nu_{\mathbf{k}}} \hat{\epsilon_{\mathbf{k}}} E_{\mathbf{k}} a_{\mathbf{k}}^\dagger e^{i\nu_k t - i\mathbf{k}.\mathbf{r}} \tag{4.2.7}$$

The classical Hamiltonian for the field is

$$H_F = \frac{1}{2} \int_V d\tau (\epsilon_0 \mathbf{E}^2 + \mu_0 \mathbf{H}^2), \tag{4.2.8}$$

On substituting $\mathbf{E}$ and $\mathbf{H}$ in the Hamiltonian H_F, the total energy separates out into the energy of the individual modes. The energy of each mode defined by $\mathbf{k}$ resembles the energy of a classical simple harmonic oscillator. To quantize the problem in the oscillator case, the conjugate variables of position q_j and momentum p_j of the j^{th} oscillator is treated as operators and the Heisenberg uncertainty condition is imposed ($[q_j, p_{j'}] = i\hbar\delta_{j,j'}$). The operators a and $a^\dagger$ are obtained from canonical transformation of the variables q and p. The energy of the quantized electromagnetic field may now be written as

$$\mathcal{H} = \hbar \sum_{\mathbf{k}} \nu_{\mathbf{k}} (a_{\mathbf{k}}^\dagger a_{\mathbf{k}} + \frac{1}{2}) \tag{4.2.9}$$

The quantized electric field operator is generally separated into its positive and negative frequency parts as

$$\mathbf{E}(\mathbf{r},t) = \mathbf{E}^{(+)}(\mathbf{r},t) + \mathbf{E}^{(-)}(\mathbf{r},t) \tag{4.2.10}$$

where

$$\mathbf{E}^{(+)}(\mathbf{r},t) = \sum_{\mathbf{k}} \hat{\epsilon_{\mathbf{k}}} \mathcal{E}_{\mathbf{k}} a_{\mathbf{k}} e^{-i\nu_k t + i\mathbf{k}.\mathbf{r}} \tag{4.2.11}$$

$$\mathbf{E}^{(-)}(\mathbf{r},t) = \sum_{\mathbf{k}} \hat{\epsilon_{\mathbf{k}}} \mathcal{E}_{\mathbf{k}} a^{\dagger}_{\mathbf{k}} e^{i\nu_k t - i\mathbf{k}.\mathbf{r}} \tag{4.2.12}$$

so that $\mathbf{E}^{(+)}(\mathbf{r},t)$ contains only annihilation operators and $\mathbf{E}^{(-)}(\mathbf{r},t)$ conatins only creation operators.

4.3 Jaynes-Cummings Hamiltonian

The Hamiltonian for the problem of an atom interacting with an eletric field ($\mathbf{E}$) is

$$H = H_A + H_F - e\mathbf{r}.\mathbf{E} \tag{4.3.1}$$

where H_A and H_F are the Hamiltonians of the atom and the radiation field. $\mathbf{r}$ is the position vector of the electron. This is the mimimal-coupling Hamiltonian (Eqns.(1.2.6-1.2.9)) written for the fully quantum mechanical case where the energy of the field is included separately. The difference from the semi-classical case arises from the fact that

$\mathbf{E}$ is no longer a simple scalar field but a quantum operator and the energy of the field needs to be explicitly included. H_F is (as in Eq.(4.2.9)),

$$H_F = \sum_{\mathbf{k}} \hbar\nu_{\mathbf{k}}(a^\dagger_{\mathbf{k}} a_{\mathbf{k}} + \frac{1}{2}) \tag{4.3.2}$$

where $a^\dagger_{\mathbf{k}}$ and $a_{\mathbf{k}}$ are the creation and annihilation operators for mode $\mathbf{k}$ of the photon field.

The terms H_A and $e\mathbf{r}$ can be represented in terms of the atomic energy eigen states ($|i\rangle$) as

$$H_A = \sum_i E_i \left|i\right\rangle \left\langle i\right| = \sum_i E_i \sigma_{ii} \tag{4.3.3}$$

and

$$e\mathbf{r} = e \sum_{i,j} \left|i\right\rangle \left\langle i\right| \mathbf{r} \left|j\right\rangle \left\langle j\right| = \sum_{i,j} \mathcal{P}_{ij}\sigma_{ij} \tag{4.3.4}$$

where the completeness of the set of eigenstates is utilized ($\sum_i \left|i\right\rangle \left\langle i\right| = 1$).

σ_{ij} is the atom transition operator and $\mathcal{P}_{ij} = e \left\langle i\right| \mathbf{r} \left|j\right\rangle$ is the electric dipole transition matrix element. Under the dipole approximation, which assumes the field to be uniform over the entire atom, the electric field $\mathbf{E}$ at the position of the point atom located at the origin is,

$$\mathbf{E} = \sum_{\mathbf{k}} \hat{\epsilon}_{\mathbf{k}} \mathcal{E}_{\mathbf{k}} (a_{\mathbf{k}} + a^\dagger_{\mathbf{k}}) \tag{4.3.5}$$

where $\mathcal{E}_{\mathbf{k}} = (\hbar\nu_k/2\epsilon_0 V)^{\frac{1}{2}}$. For simplicity a linear polarization basis is considered and the polarization unit vectors, $\hat{\epsilon}_{\mathbf{k}}$ are taken to be real.

Substituting Eq.(4.3.2-4.3.5) into Eq.(4.3.1) we get

$$H = \sum_{\mathbf{k}} \hbar\nu_k a_{\mathbf{k}}^{\dagger} a_{\mathbf{k}} + \sum_i E_i \sigma_{ii} + \hbar \sum_{i,j} \sum_{\mathbf{k}} g_{\mathbf{k}}^{ij} \sigma_{ij} (a_{\mathbf{k}} + a_{\mathbf{k}}{}^{\dagger}) \tag{4.3.6}$$

where

$$g_{\mathbf{k}}^{ij} = -\frac{\mathcal{P}_{ij}.\hat{\epsilon}_{\mathbf{k}}\mathcal{E}_{\mathbf{k}}}{\hbar} \tag{4.3.7}$$

Eq.(4.3.6) does not include the zero point energy and $\mathcal{P}_{ij}$ is assumed real for simplicity. For the case of a two-level atom, since $\mathcal{P}_{ab} = \mathcal{P}_{ba}$, we have

$$g_{\mathbf{k}} = g_{\mathbf{k}}{}^{ab} = g_{\mathbf{k}}{}^{ba} \tag{4.3.8}$$

Under this simplification the complete Hamiltonian is

$$H = \sum_{\mathbf{k}} \hbar\nu_k a_{\mathbf{k}}^{\dagger} a_{\mathbf{k}} + (E_a\sigma_{aa} + E_b\sigma_{bb}) + \hbar \sum_{\mathbf{k}} g_{\mathbf{k}} (\sigma_{ab} + \sigma_{ba})(a_{\mathbf{k}} + a_{\mathbf{k}}^{\dagger}) \tag{4.3.9}$$

The second term in Eq.(4.3.9) can be written as

$$(E_a\sigma_{aa} + E_b\sigma_{bb}) = \frac{1}{2}\hbar\omega(\sigma_{aa} - \sigma_{bb}) + \frac{1}{2}(E_a + E_b) \tag{4.3.10}$$

where the substitutions $(E_a - E_b) = \hbar\omega$ and $\sigma_{aa} + \sigma_{bb} = 1$ have been made. The constant $(E_a + E_b)/2$ is dropped. To obtain the familiar form of the Jaynes-Cummming

Hamiltonian, Eq.(4.3.9) is rewritten in terms of the atomic creation and annihilation operators σ_+ and σ_-. These are given by

$$\begin{aligned} \sigma_z &= \sigma_{aa} - \sigma_{bb} = |a\rangle\langle a| - |b\rangle\langle b| \\ \sigma_+ &= \sigma_{ab} = |a\rangle\langle b| \\ \sigma_- &= \sigma_{ba} = |b\rangle\langle a| \end{aligned} \tag{4.3.11}$$

where σ_+, σ_- and σ_z satisfies the spin- 1/2 algebra of Pauli matrices. σ_z is the inversion operator.

The Hamiltonian (Eq.(4.3.9)) can now be rewritten as,

$$H = \sum_{\mathbf{k}} \hbar\nu_k a^\dagger_{\mathbf{k}} a_{\mathbf{k}} + \frac{1}{2}\hbar\omega\sigma_z + \hbar\sum_{\mathbf{k}} g_{\mathbf{k}}(\sigma_+ + \sigma_-)(a_{\mathbf{k}} + a^\dagger_{\mathbf{k}}) \tag{4.3.12}$$

The interaction energy (Eq.(4.3.12)) consists of four terms. The term, $\sigma_- a^\dagger_{\mathbf{k}}$ describes the process in which an atom looses its energy by making a transition and a photon in mode $\mathbf{k}$ is created. $\sigma_+ a_{\mathbf{k}}$ describes the reverse process. $\sigma_+ a^\dagger_{\mathbf{k}}$ describes a process in which an atom is excited and a photon is created resulting in an energy gain of $2\hbar\omega$. $\sigma_- a_{\mathbf{k}}$ similarly describes an energy loss of $2\hbar\omega$. The energy nonconserving terms are dropped to create what is called the rotating wave approximation. Semi-classically this corresponds to ignoring the high frequency terms. The resulting Hamiltonian is

$$\begin{aligned} H &= \sum_{\mathbf{k}} \hbar\nu_k a^\dagger_{\mathbf{k}} a_{\mathbf{k}} + \frac{1}{2}\hbar\omega\sigma_z + \hbar\sum_{\mathbf{k}} g_{\mathbf{k}}(\sigma_+ a_{\mathbf{k}} + \sigma_- a^\dagger_{\mathbf{k}}) \\ H &= H_0 + H_1 \end{aligned} \tag{4.3.13}$$

where H_0 represents the free Hamiltonian and H_1 represents the interaction term. This is the Jaynes-Cummings Hamiltonian describing the interaction of a two-level atom with a multi-mode field. The special case of the single mode field, considered next, is exactly solvable and is widely studied in quantum optics. This model is also used in our study of meso-scale lasers and saturable absorbers in Chapter 5.

4.3.1 Single mode Jaynes-Cummings Hamiltonian

The form of the Hamiltonian, (Eq.(4.3.13)) simplifies for a single-mode quantized field of frequency ν and the interaction H_1 to

$$H_1 = \hbar g(\sigma_+ a + \sigma_- a^\dagger) \tag{4.3.14}$$

Generally this problem is solved in the interaction picture and in that case the interaction V is given by

$$V = e^{iH_0 t/\hbar} H_1 e^{-iH_0 t/\hbar} \tag{4.3.15}$$

Using the Baker-Hausdoff relation

$$e^{\alpha A} B e^{-\alpha A} = B + \alpha[A, B] + \frac{\alpha^2}{2!}[A, [A, B]] \tag{4.3.16}$$

it can be seen that

$$e^{i\nu a^\dagger a t} a e^{-i\nu a^\dagger a t} = a e^{-i\nu t} \qquad e^{i\omega\sigma_z t/2}\sigma_+ e^{-i\omega\sigma_z t/2} = \sigma_+ e^{i\omega t} \tag{4.3.17}$$

And, using the above equations we have,

$$
\begin{aligned}
V &= \hbar g(\sigma_+ a e^{i\Delta t} + a^\dagger \sigma_- e^{-i\Delta t}) \\
\Delta &= \omega - \nu
\end{aligned} \tag{4.3.18}
$$

The Schrödinger equation in the interaction picture for the state $|\psi\rangle$ describing the atom-field system is

$$
i\hbar \frac{\partial |\psi\rangle}{\partial t} = \mathcal{V} |\psi\rangle \tag{4.3.19}
$$

This problem is analytically solvable and shows Rabi oscillations between the photon field and the atom. The nature of the oscillation is qualitatively different from semi-classical predictions and depends on initial conditions. For an initial coherent state of photons (Poisson distribution), the envelope of oscillation is not constant - it collapses and rebuilds. Also according to the semi-classical theory an atom in the excited state cannot make a transition to the lower level in the absence of a driving field, as frequency of the Rabi oscillation is proportional to the incident field amplitude. In the fully quantum-mechanical treatment, the transition becomes possible because of spontaneous emission caused by vacuum fluctuations.

Figure 4.1 shows Rabi oscillations in 1 and 4 emitter systems coupled to a single cavity mode. The calculations are performed using techniques discussed in Chapter 5 and the parameters chosen are similar to those of Figure 5.3. In general, emitter-field system is coupled to external reservoirs and the Rabi oscillations decay with time. The plots compare these oscillations for different values of the incoherent pump below and around lasing threshold. For the emitter initially in the excited state and an empty cavity, the frequency of Rabi oscillations is given by the emitter-cavity coupling g. As

shown in [Ref. [32]] adding emitters effectively makes the cavity coupling g stronger. It increases as $\sqrt{N_e}$, where N_e is the number of emitters. For 4 emitters the period of oscillations roughly doubles as shown by Figure 4.1. With the increase of incoherent pump, the coherent oscillation dies off. The pump values shown in Figure 4.1 (c) and (d) are normalized. The actual pump energy flowing is obtained by multiplying with N_e. Normalized pump denotes the energy flowing into individual emitters.

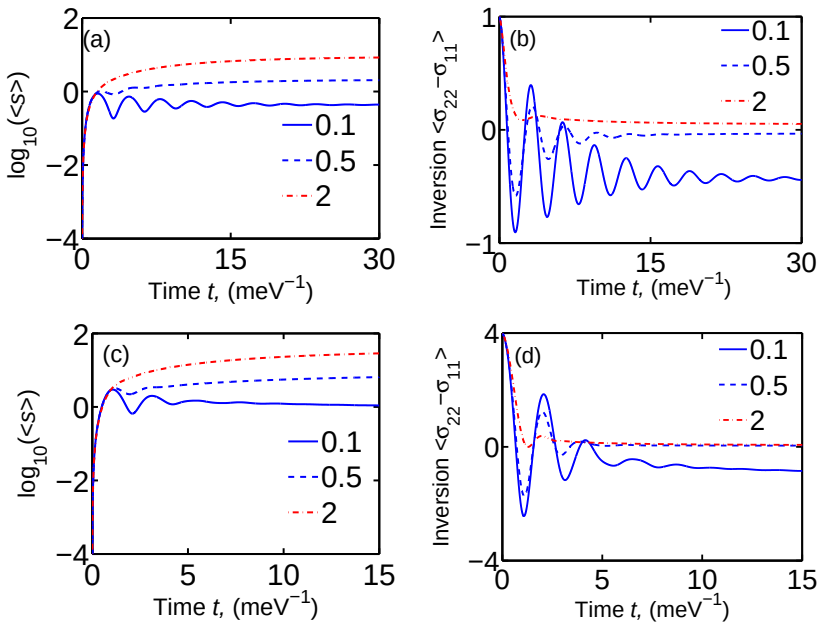

Figure 4.1: Scaling of Rabi oscillations for multi-emitter systems. Single emitter case. (a) Mean photon number in lasing mode in log_{10} scale. (b) Net inversion of emitters. 4 emitter case. (c) Mean photon number in lasing mode in log_{10} scale. (d) Net inversion of emitters. The legend shows the different normalized pump values. Dark solid line (P = 0.1 meV), dashed line (P = 0.5 meV), light dash-dotted line (P = 2 meV). Initial state of system consists of all emitters in excited state and zero cavity photons. Parameters: Emitter-cavity coupling, $g = 1$ meV, spontaneous emission into non-lasing modes, $\gamma = 0.1$ meV, photon energy, $\omega = 1000$ meV, cavity loss, $\kappa = 0.1$ meV.

4.4 General reservoir theory

The emitter-field system considered in the previous section is closed in the sense that energy remains conserved. This allows the system to perform Rabi oscillations. However realistic matter-field systems involve loss mechanisms to outside reservoirs. These reservoirs are treated as large systems of harmonic oscillators. We present here a brief review of the general reservoir theory. We consider in general a system denoted by S interacting with a reservoir denoted by R. The combined density operator is ρ_{SR}. The reduced density operator of the system is obtained by tracing over the reservoir variables, i.e.,

$$\rho_S = Tr_R(\rho_{SR}) \tag{4.4.1}$$

In presence of system-reservoir interaction $V(t)$ the equation of motion for ρ_{SR} is

$$i\hbar\dot{\rho}_{SR} = [V(t), \rho_{SR}(t)] \tag{4.4.2}$$

Integration of this equation gives

$$\rho_{SR}(t) = \rho_{SR}(t_i) - \frac{i}{\hbar}\int_{t_i}^{t}[V(t'), \rho_{SR}(t')]dt' \tag{4.4.3}$$

where t_i denotes time when the interaction starts. Substituting $\rho_{SR}(t)$ back into Eq.(4.4.2), gives

$$\dot{\rho}_{SR}(t) = -\frac{i}{\hbar}[\mathcal{V}(t), \rho_{SR}(t_i)] - \frac{1}{\hbar^2}\int_{t_i}^{t}[\mathcal{V}(t), [\mathcal{V}(t'), \rho_{SR}(t')]]dt' \tag{4.4.4}$$

The system and the reservoir are independent, when $V = 0$, and the density operator ρ_{SR} separates into a product $\rho_{SR}(t) = \rho_S(t) \otimes \rho_R(t_i)$. The reservoir is large and assumed to be in equilibrium. In the limit of weak interaction, we expect a solution of the form

$$\rho_{SR}(t) = \rho_S(t) \otimes \rho_R(t_i) + \rho_c(t) \tag{4.4.5}$$

where $\rho_c(t)$ is of higher order in V. Eq.(4.4.1), requires $Tr_R[\rho_c(t)] = 0$
Substituting $\rho_{SR}(t)$ from Eq.(4.4.5) into the integrand of Eq.(4.4.4) and retaining terms up to order V^2, we have

$$\dot{\rho}_S = -\frac{i}{\hbar} Tr_R[\mathcal{V}(t), \rho_S(t_i) \otimes \rho_R(t_i)] - \frac{1}{\hbar^2} Tr_R \int_{t_i}^{t} [\mathcal{V}(t), [\mathcal{V}(t'), \rho_S(t') \otimes \rho_R(t_i)]] dt' \tag{4.4.6}$$

The reduced density operator $\rho_S(t)$ determines the statistical properties of the system. The presence of $\rho_S(t')$ in the integrand of Eq.(4.4.6) states that $\rho_S(t)$ depends on its past history from $t = t_i$ to t'. Typically, the reservoir is an extended open system with a large number of degrees of freedom (modes, phonons, etc.) and this leads to a delta function $\delta(t - t')$ in the integral. Hence $\rho_S(t')$ can be replaced by $\rho_S(t)$ and the history independent process is called Markovian. The assumption is reasonable since damping destroys memory of the past. Eq.(4.4.6) now becomes

$$\dot{\rho}_S = -\frac{i}{\hbar} Tr_R[\mathcal{V}(t), \rho_S(t_i) \otimes \rho_R(t_i)] - \frac{1}{\hbar^2} Tr_R \int_{t_i}^{t} [\mathcal{V}(t), [\mathcal{V}(t'), \rho_S(t) \otimes \rho_R(t_i)]] dt' \tag{4.4.7}$$

This may now be applied to the description of spontaneous emission of an atom and decay of a cavity mode due to partially reflecting mirrors.

4.4.1 Spontaneous emission

The interaction of an atom with a single cavity mode in a closed environment leads to Rabi oscillations where the energy is transferred back and fourth between the emitter and the optical field. However, spontaneous decay of an atom is an irreversible process where it loses its energy to the field and this situation may be explained by a simple model in which the atom is coupled to a reservoir of simple harmonic oscillators. The two-level atom is the system ($\rho_S = \rho_{atom}$) in this case and it interacts with a reservoir, R, of simple harmonic oscillators. An oscillator of frequencies $\nu_k = ck$ is described by creation (annihilation) operators $b^\dagger_{\mathbf{k}}$ ($b_{\mathbf{k}}$) . In the interaction picture and rotating wave approximation the Hamiltonian is

$$\mathcal{V}(t) = \hbar \sum_{\mathbf{k}} g_{\mathbf{k}} [b^\dagger_{\mathbf{k}} \sigma_- e^{-i(\omega-\nu_k)t} + \sigma_+ b_{\mathbf{k}} e^{i(\omega-\nu_k)t}] \tag{4.4.8}$$

where $\sigma_- = |b\rangle\langle a|$ and $\sigma_+ = |a\rangle\langle b|$ are the creation and annihilation operators for the atom. Using interaction energy V, in Eq.(4.4.6), we obtain

$$\begin{aligned}
\dot{\rho}_{atom} = -i\sum_{\mathbf{k}} g_{\mathbf{k}}\langle b_{\mathbf{k}}^{\dagger}\rangle[\sigma_-, \rho_{atom}(t_i)]e^{-i(\omega-\nu_k)t} \\
-\int_{t_i}^{t} dt' \sum_{\mathbf{k},\mathbf{k}'} g_{\mathbf{k}} g_{\mathbf{k}'}([\sigma_-\sigma_-\rho_{atom}(t') - 2\sigma_-\rho_{atom}(t')\sigma_- + \rho_{atom}(t')\sigma_-\sigma_-] \\
\times e^{-i(\omega-\nu_k)t-i(\omega-\nu_{k'})t'}\langle b_{\mathbf{k}}^{\dagger} b_{\mathbf{k}'}^{\dagger}\rangle + [\sigma_-\sigma_+\rho_{atom}(t') - \sigma_+\rho_{atom}(t')\sigma_-] \\
\times e^{-i(\omega-\nu_k)t+i(\omega-\nu_{k'})t'}\langle b_{\mathbf{k}}^{\dagger} b_{\mathbf{k}'}\rangle + [\sigma_+\sigma_-\rho_{atom}(t') - \sigma_-\rho_{atom}(t')\sigma_+] \\
\times e^{i(\omega-\nu_k)t-i(\omega-\nu_{k'})t'}\langle b_{\mathbf{k}} b_{\mathbf{k}'}^{\dagger}\rangle) + \\
-i\sum_{\mathbf{k}} g_{\mathbf{k}}\langle b_{\mathbf{k}}\rangle[\rho_{atom}(t_i), \sigma_+]e^{i(\omega-\nu_k)t} \\
-\int_{t_i}^{t} dt' \sum_{\mathbf{k},\mathbf{k}'} g_{\mathbf{k}} g_{\mathbf{k}'}([\rho_{atom}(t')\sigma_+\sigma_+ - 2\sigma_+\rho_{atom}(t')\sigma_+ + \sigma_+\sigma_+\rho_{atom}(t')] \\
\times e^{i(\omega-\nu_k)t-i(\omega-\nu_{k'})t'}\langle b_{\mathbf{k}'} b_{\mathbf{k}}\rangle + [\rho_{atom}(t')\sigma_-\sigma_+ - \sigma_+\rho_{atom}(t')\sigma_-] \\
\times e^{i(\omega-\nu_k)t+i(\omega-\nu_{k'})t'}\langle b_{\mathbf{k}'}^{\dagger} b_{\mathbf{k}}\rangle + [\rho_{atom}(t')\sigma_+\sigma_- - \sigma_-\rho_{atom}(t')\sigma_+] \\
\times e^{-i(\omega-\nu_k)t-i(\omega-\nu_{k'})t'}\langle b_{\mathbf{k}'} b_{\mathbf{k}}^{\dagger}\rangle)
\end{aligned} \tag{4.4.9}$$

where the expectation values refer to the initial state of the reservoir. The thermal reservoir is considered in the problem, with the state of the reservoir described by,

$$\rho_R = \Pi_{\mathbf{k}}[1 - \exp(-\frac{\hbar\nu_k}{k_B T})]\exp(-\frac{\hbar\nu_k b_{\mathbf{k}}^{\dagger} b_{\mathbf{k}}}{k_B T}) \tag{4.4.10}$$

where k_B is the Boltzmann constant and T is the temperature. The expectation values required for Eq.(4.4.9), can be obtained using ρ_R. On substituting the expectation values, we obtain

$$\begin{aligned}\dot{\rho}_{atom} = -\int_{t_i}^{t} dt' \sum_{\mathbf{k}} g_{\mathbf{k}}^2 ([\sigma_-\sigma_+\rho_{atom}(t') - \sigma_+\rho_{atom}(t')\sigma_-]\bar{n}_{\mathbf{k}} e^{-i(\omega-\nu_k)(t-t')} \\ +[\sigma_+\sigma_-\rho_{atom}(t') - \sigma_-\rho_{atom}(t')\sigma_+](\bar{n}_k+1)e^{i(\omega-\nu_k)(t-t')} \\ +[\rho_{atom}(t')\sigma_-\sigma_+ - \sigma_+\rho_{atom}(t')\sigma_-]\bar{n}_{\mathbf{k}} e^{i(\omega-\nu_k)(t-t')} \\ +[\rho_{atom}(t')\sigma_+\sigma_- - \sigma_-\rho_{atom}(t')\sigma_+](\bar{n}_k+1)e^{-i(\omega-\nu_k)(t-t')}) \quad (4.4.11)\end{aligned}$$

where the thermal average boson number is

$$\bar{n}_{\mathbf{k}} = \frac{1}{\exp(\frac{\hbar\nu_k}{k_B T}) - 1} \quad (4.4.12)$$

The sum over $\mathbf{k}$ may be replaced by an integral for a continuum of reservoir modes,

$$\sum_{\mathbf{k}} \rightarrow 2\frac{V}{(2\pi)^3}\int_0^{2\pi} d\phi \int_0^{\pi} d\theta \int_0^{\infty} k^2 dk \quad (4.4.13)$$

where V is the quantization volume. The integrations in Eqn.(4.4.11) carried out using the Wieskopf-Wigner approximation [Ref.[15]] gives

$$\begin{aligned}\dot{\rho}_{atom} = -\bar{n}_{th}\frac{\Gamma}{2}[\sigma_-\sigma_+\rho_{atom}(t) - \sigma_+\rho_{atom}(t)\sigma_-] \\ -(\bar{n}_{th}+1)\frac{\Gamma}{2}[\sigma_+\sigma_-\rho_{atom}(t) - \sigma_-\rho_{atom}(t)\sigma_+] \\ -\bar{n}_{th}\frac{\Gamma}{2}[\rho_{atom}(t)\sigma_-\sigma_+ - \sigma_+\rho_{atom}(t)\sigma_-] \\ -(\bar{n}_{th}+1)\frac{\Gamma}{2}[\rho_{atom}(t)\sigma_+\sigma_- - \sigma_-\rho_{atom}(t)\sigma_+] \quad (4.4.14)\end{aligned}$$

where $\bar{n}_{th} = \bar{n}_{k_0}$, $(k_0 = \omega/c)$ and

$$\Gamma = \frac{1}{4\pi\epsilon_0}\frac{4\omega^3 \mathcal{P}^2{}_{ab}}{3\hbar c^3} \tag{4.4.15}$$

is the atomic decay rate. The value of $g_{\mathbf{k}}$ (Eq.(4.3.7)) is used in deriving the expression of Γ . The equation for the atomic density matrix elements derived from Eq.(4.4.14) for zero temperature $\bar{n}_{th} = 0$ is

$$\begin{aligned} \dot{\rho}_{aa} &= -\Gamma\rho_{aa} \\ \dot{\rho}_{ab} &= -\frac{\Gamma}{2}\rho_{ab} \\ \dot{\rho}_{bb} &= \Gamma\rho_{aa} \end{aligned} \tag{4.4.16}$$

$\dot{\rho}_{aa} + \dot{\rho}_{bb} = 0$ implies conservation of probability. Also spontaneous decay being an incoherent process decays the coherence between the two levels, ρ_{ab}.

4.4.2 Cavity-mode decay

Cavity-mode decay can be treated in a similar way. A radiation field of frequency ν inside a cavity described by operators a and $a^\dagger$ is in interaction with oscillator modes of a reservoir described by operators $b_{\mathbf{k}}$ and $b^\dagger_{\mathbf{k}}$. For transmission losses they actually represent the field outside the cavity. The interaction Hamiltonian for this problem is of the form,

$$V(t) = \hbar \sum_{\mathbf{k}} g_{\mathbf{k}}[b^\dagger_{\mathbf{k}} a e^{-i(\nu-\nu_k)t} + a^\dagger b_{\mathbf{k}} e^{i(\nu-\nu_k)t}] \tag{4.4.17}$$

and can be solved by assuming the reservoir to be at thermal equilibrium. The equation for the reduced density operator of the field is obtained by replacing the atomic operators σ_- with a.

$$\dot{\rho} = -\bar{n_{th}}\kappa[aa^\dagger\rho - 2a^\dagger\rho a + \rho aa^\dagger] - (\bar{n_{th}} + 1)\kappa[a^\dagger a\rho - 2a\rho a^\dagger + \rho a^\dagger a] \tag{4.4.18}$$

where $\bar{n}_{th} = \bar{n}_{\mathbf{k}_0}$ is the number of quanta at frequency ν in the thermal reservoir and κ is the decay constant. At zero temperature ($\bar{n}_{th} = 0$),

$$\dot{\rho} = -\kappa[a^\dagger a\rho - 2a\rho a^\dagger + \rho a^\dagger a] \tag{4.4.19}$$

Transmission loss, κ, is related to the Q factor of the cavity by $\kappa = \nu/Q$.

4.5 Laser theory

In contrast to the semi-classical theory of lasers the quantum nature of light is considered in developing a quantum theory. The density matrix of the coupled atom-field system is solved under interaction with external reservoirs. The model considered for a single mode laser is described as follows. Atoms are pumped randomly from the ground state $|g\rangle$ to the excited state $|a\rangle$ at rate λ_a. The state $|a\rangle$ also denotes the upper state lasing transition and it decays to state $|b\rangle$ emitting a lasing photon in the process. Both states $|a\rangle$ and $|b\rangle$ decay to states $|c\rangle$ and $|d\rangle$ at rates γ_a and γ_b which in turn decay to state $|g\rangle$ at rates γ_c and γ_d. The rates γ_c, $\gamma_d \gg \gamma_a$, γ_b. To simplify the problem, we set $\gamma_a = \gamma_b = \gamma$. The lasing mode is also tuned to resonance with the atomic transition. Damping of the cavity mode is considered through its interaction with the modes of an external reservoir. Physically it represents transmission losses through partially transmitting mirrors. The

pumping and other damping mechanisms are considered in a phenomenological way similar to the semi-classical theory.

The Hamiltonian describing interaction of the active atoms with the single-mode laser field is

$$\mathcal{V} = \sum_i \hbar g({\sigma_+}^i a + a^\dagger {\sigma_-}^i) = \sum_i V_i \tag{4.5.1}$$

where ${\sigma_+}^i = (|a\rangle \langle b|)^i$ is the creation operator for the i^{th} atom. The problem is solved in the interaction picture. The frequency dependent terms in the Hamiltonian dissapear in absence of detuning. The equation for laser field density matrix, obtained by tracing out the atomic variables is

$$\dot{\rho}_{nn'} = -\frac{i}{\hbar} Tr_{atoms}[V, \rho]_{n,n'} + (\mathcal{L}\rho)_{n,n'} \tag{4.5.2}$$

where from Eq.(4.4.19)

$$(\mathcal{L}\rho)_{n,n'} = -\frac{\kappa}{2}(n+n')\rho_{nn'} + \mathcal{C}\sqrt{(n+1)(n'+1)}\rho_{n+1,n'+1} \tag{4.5.3}$$

Damping of the lasing mode has been included in the above equation following the treatment in the previous section.

The equation for the lasing density matrix (Eq.(4.5.2)) contains terms like $\sum_i \rho^i_{an,bn+1}(t,t_i)$. t_i represents the time of injection of the i^{th} atom, as it starts interacting with the field. These elements are analogous to the elements of the population matrix introduced in Chapter 1. In the case of the quantum theory, the population matrix is defined as

$$\rho_{an,bn+1}(t) = \sum_i \rho^i_{an,bn+1}(t,t_i) \tag{4.5.4}$$

Elements $\rho_{\alpha n,\alpha' n+1}(t)$ with projections on to the atomic states, ($\alpha = a, b..g$) can be solved in the adiabatic approximation which assumes that the variation of the field in negligible in the atomic lifetimes ($1/\gamma$). Their values when substituted in Eq.(4.5.2) yields the equation of motion of the reduced density matrix of the field.

$$\dot{\rho}_{nn'} = -(\frac{\mathcal{N}'_{nn'}\mathcal{A}}{1+\mathcal{N}_{nn'}\mathcal{B}/\mathcal{A}})\rho_{nn'} + (\frac{\sqrt{nn'}\mathcal{A}}{1+\mathcal{N}_{n-1,n'-1}\mathcal{B}/\mathcal{A}})\rho_{n-1,n'-1} \\ -\frac{\mathcal{C}}{2}(n+n')\rho_{nn'} + \mathcal{C}\sqrt{(n+1)(n'+1)}\rho_{n+1,n'+1} \tag{4.5.5}$$

where $\mathcal{A}$ is the linear gain coefficient and is equal to $2r_a g^2/\gamma^2$, $\mathcal{B}$ is the self-saturation coefficient, $\mathcal{B} = 4g^2\mathcal{A}/\gamma^2$. r_a is the effective pumping rate given by $\gamma\lambda_a/(\gamma+\lambda_a)$. $\mathcal{N}'_{nn'}$ and $\mathcal{N}_{nn'}$ are dimensionless factors given by

$$\mathcal{N}'_{nn'} = \frac{1}{2}(n+1+n'+1) + \frac{(n-n')^2\mathcal{B}}{8\mathcal{A}} \\ \mathcal{N}_{nn'} = \frac{1}{2}(n+1+n'+1) + \frac{(n-n')\mathcal{B}}{16\mathcal{A}} \tag{4.5.6}$$

The linear gain and self-saturation coefficients are similar to the coefficients of the semi-classical theory considered in Chapter 1 for the case of zero detuning. Eq.(4.5.5) constitutes the basic equation of a laser. The diagonal density matrix elements ρ_{nn} represents the probability $p(n)$ of n photons in the field. The equation for the diagonal elements is,

$$\dot{p}(n) = -(\frac{(n+1)\mathcal{A}}{1+(n+1)\mathcal{B}/\mathcal{A}})p(n) + (\frac{n\mathcal{A}}{1+n\mathcal{B}/\mathcal{A}})p(n-1) \\ -\mathcal{C}np(n) + \mathcal{C}(n+1)p(n+1) \tag{4.5.7}$$

In these equations, diagonal elements couple to diagonal elements and in general only off-diagonal elements with the same difference $(n-n')$ are coupled.

To connect to the mean-field semiclassical result of Chapter 1 (Eq.(1.5.6)), we derive an equation for the mean number of photons, $< n >$. For near threshold operation, $\mathcal{B} < n > /\mathcal{A} \ll 1$, we obtain (after expanding the two denominators on the right hand side)

$$\langle \dot{n} \rangle = \sum_{n=0}^{\infty} n \frac{dp(n)}{dt} = (\mathcal{A} - \mathcal{C}) < n > -\mathcal{B} < (n+1)^2 > +\mathcal{A} \tag{4.5.8}$$

In the limit of $< n > \ll 1$ and $< n^2 > = < n >^2$, this equation reduces to Eq.(1.5.6). Thus, a semi-classical treatment is valid when a large number of photons are present. In such a situation one may describe the light field in terms of a scalar field and, in this large number limit, correlations factorize into product of means. The term $\mathcal{A}$, absent in the semiclassical equation, represents spontaneous emission into the lasing mode. As mentioned in Chapter 1 this is caused by vacuum fluctuations and allows the field to build up from an initial cold cavity state (n = 0).

The full quantum theory of meso-scale lasers is developed in the next chapter, which essentially uses the Jaynes-Cummings Hamiltonian as a starting point and uses the theory of reservoirs to couple the system to the outside world. However, solutions obtained are exact in the absence of any adiabatic and large particle-number approximation. This allows us to connect with the semi-classical predictions of Chapter 3. For example, adiabatic elimination only retains the information for the light field and hence no information on carrier-depinning can be obtained from this method.

Chapter 5

Quantum theory of meso-scale lasers and saturable absorbers

5.1 Introduction

Fluctuations due to quantization can dominate predicted behavior of meso-scale lasers. Using only semiclassical master equations and specific device parameters, it was shown in Chapter 3 that quantization of particle number, and the fact that a lowest energy state of the system exists, can suppress lasing and enhance spontaneous emission around threshold [Ref. [34, 35]]. The conditions under which this happens require treating β as a separate variable and giving it a small value $\beta \ll 1$. For this semiclassical system, dynamic switching between two characteristic system states can dominate fluctuations and correlations between n discrete excited electronic emitter states and s discrete photons and create a non-Poisson probability distribution.

However, to study the fundamental contribution of field quantization to noise and fluctuations in meso-scale lasers requires going beyond particle number quantization and semiclassical master equations. Here, we use a quantum mechanical description of a meso-scale laser containing s cavity photons and N_e emitters and find solutions by direct integration of the system's density matrix. Quantum fluctuations in this finite-sized dissipative system is found to be sensitive to the number of emitters and the presence of inhomogeneous saturable absorbtion. This result gives a physical interpretation to

the use of β as a free variable in the semi-classical master equation and the predicted behavior discussed in Chapter 3.

This chapter is organized as follows. In Section 5.2 a model is developed that includes N_e two-level (quantum dot or atom) emitters incoherently pumped by an external reservoir and a quantized photon field with s cavity photons that can decay into an external reservoir through finite reflectivity mirrors. The algorithm used in solving this problem computationally is explained in detail. Section 5.3 describes the calculated steady-state properties as the number of identical emitters in the cavity is increased. Section 5.4 considers the case of an inhomogeneous active system consisting of identical emitters and a saturable absorber. Under these conditions, the quantum model can predict lasing suppression, enhanced spontaneous emission and the associated emitter excitation number de-pinning, and bi-modal probability distributions. These results allow interpretation of previously reported predictions found by solving the semiclassical master equations [Ref. [34, 35]].

Section 5.5 describes the predictions of the quantum model correlation functions for the production of non-classical light.

5.2 THE MODEL

Figure 5.1(a) is a schematic diagram of a prototype meso-scale laser consisting of multiple two-level emitters such as quantum dots or atoms coupled to a single cavity mode in a high-Q optical cavity formed by two partially transmitting mirrors. In our model of this system, both light and emitters are treated quantum mechanically. The number of emitters is N_e and, for simplicity, they are assumed to be in resonance with the single cavity mode and so detuning is ignored.

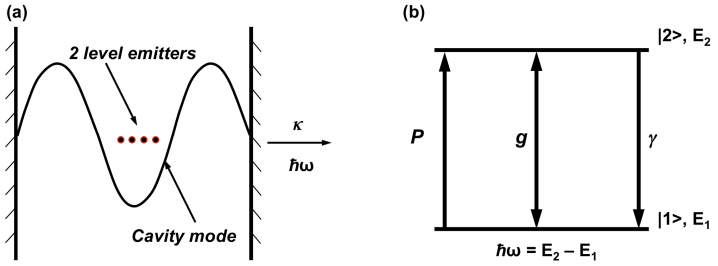

Figure 5.1: (a) Schematic diagram of multiple emitters coupled to a single optical cavity mode with total mirror loss rate, κ. (b) Processes in a single emitter showing incoherent pump transition rate P, stimulated and spontaneous coefficient g, and loss rate γ. Separation in emitter eigenenergy is $E_2 - E_1 = \hbar\omega$, where ω is the angular frequency of the high-Q optical cavity resonance.

As illustrated in Fig. 5.1(b), emitter electronic states are continuously incoherently pumped at rate P by an external reservoir. The stimulated and spontaneous emission coefficient coupling the ground $|1\rangle$ and excited $|2\rangle$ electronic states of each emitter is g. The separation in emitter eigenenergy is $E_2 - E_1 = \hbar\omega$, where ω is the angular frequency of the high-Q optical cavity resonance. The emitters are damped at rate γ by a reservoir of oscillators representing incoherent decay via spontaneous emission into non-lasing leaky modes. Decay of the laser photon field in the single cavity mode is by coupling to another external reservoir through partially transmitting mirrors with total loss rate κ.

The Hamiltonian describing two-level emitters coupled to a single cavity mode and interacting with external reservoirs is

$$H = H_S + H_{RS} + H_R \tag{5.2.1}$$

where H_S is the Hamiltonian of the system of emitters and photons, H_R is the Hamiltonian for the reservoirs, and H_{RS} couples the system to the reservoirs. H_S is the Jaynes-Cummings Hamiltonian [Ref. [15]] coupling a single cavity mode with the emitters (see Chapter 4). For a homogeneous system, in which emitter properties are identical,

$$H_S = \omega a^\dagger a + \sum_{k=1}^{N_e} \omega \left|2_k\right\rangle \left\langle 2_k\right| + g(\sigma_k a^\dagger + a {\sigma_k}^\dagger) \tag{5.2.2}$$

where $\hbar = 1$, and the operators ${\sigma_k}^\dagger = \left|2_k\right\rangle \left\langle 1_k\right|$ and $\sigma_k = \left|1_k\right\rangle \left\langle 2_k\right|$ couple the ground $\left|1_k\right\rangle$ and excited $\left|2_k\right\rangle$ electronic states of the emitter k with energies $E_1 = 0$ and $E_2 = \omega$ respectively. The operator $a^\dagger$ creates a photon of energy ω. The coupling terms are evaluated within the dipole and rotating wave approximation [Ref. [15]]. The summation runs from $k = 1$ to the total number of emitters, N_e.

The Hamiltonian coupling the system to the reservoirs is

$$H_{RS} = \sum_{R''} \mu_{R''}[a b_{R''}^\dagger + b_{R''} a^\dagger] + \sum_{R} \lambda_R[\sigma_k {b_R}^\dagger + b_R {\sigma_k}^\dagger] + \sum_{R'} \lambda'_{R'}[\sigma_k {b_{R'}}^\dagger + b_{R'} {\sigma_k}^\dagger] \tag{5.2.3}$$

The first term causes direct dissipation of cavity mode photons due to incomplete reflectance of the mirrors and thereby coupling it to the continuum of photonic modes outside the micro-cavity. The second term is dissipation by direct coupling of the emitter to harmonic oscillator photonic modes different from the cavity mode. This describes dissipation of the emitter by spontaneous emission to an external reservoir of photons created by $b_R^\dagger$. The last term is due to the incoherent pump that is modeled as an inverse spontaneous decay process. The pump is a process that couples the emitter with a reservoir of inverted harmonic oscillators [Ref. [26, 44]]. The pumping and emission mechanisms in H_{RS} introduce decoherence affecting the quantum properties of the system.

The term H_R describes the external reservoirs of harmonic oscillators with bosonic commutation rules. The coupling constants μ_R and λ_R depend on the particular mode of the reservoir. Detailed derivation of these interactions with reservoirs may be found in Refs.[[12, 15, 26, 27]]. (See Chapter 4 for details)

To describe the different pumping and loss mechanisms for a single emitter it is convenient to work in the basis $(|1s\rangle\,;|2s\rangle)$ where s is the number of cavity photons and $(1,\,2)$ are the states of the emitter. These are product states between the emitter states and the Fock states of the cavity mode. Although the theory may include the effects of finite temperature reservoirs, we consider the special case of zero temperature (T = 0 K) to emphasize the quantum origin of the fluctuations. The reduced density matrix ρ for the coupled emitter-photon system is obtained from the total density matrix ρ_T by tracing out the reservoir degrees of freedom. In the interaction picture for multiple emitters ρ satisfies the master equation

$$\begin{aligned}\frac{d\rho}{dt} = \frac{i}{\hbar}[\rho, H_S] + \frac{\kappa}{2}(2a\rho a^\dagger - a^\dagger a\rho - \rho a^\dagger a) \quad &+ \quad \sum_k \frac{\gamma_k}{2}(2\sigma_k\rho{\sigma_k}^\dagger - {\sigma_k}^\dagger\sigma_k\rho - \rho{\sigma_k}^\dagger\sigma) \\ &+ \quad \sum_k \frac{P_k}{2}(2{\sigma_k}^\dagger\rho\sigma_k - \sigma_k{\sigma_k}^\dagger\rho - \rho\sigma_k{\sigma_k}^\dagger)\end{aligned} \tag{5.2.4}$$

or

$$\frac{d\rho}{dt} = \hat{\mathbf{L}}\rho \tag{5.2.5}$$

where $\hat{\mathbf{L}}$ is the time propagator for the density matrix. The master equation is obtained under the Born-Markov approximation [Ref. [15]] for the interaction between the system and the reservoirs. In the chosen basis the matrix elements of the reduced density operator ρ are

$$\rho_{kn,jm} = \langle kn| \, \rho \, |jm\rangle \tag{5.2.6}$$

The diagonal matrix elements describe populations of the emitter-photon levels and the off-diagonal terms quantify the coherence between these levels. Eq.(5.2.4) may be used to obtain the time evolution of the system. For a single emitter at time $t = 0$ the evolution of the density matrix is

$$\frac{d\rho}{dt} = \begin{bmatrix} \partial_t \rho_{1s,1s} & \partial_t \rho_{1s,2s-1} \\ \partial_t \rho^*_{1s,2s-1} & \partial_t \rho_{2s,2s} \end{bmatrix} \tag{5.2.7}$$

where

$$\partial_t \rho_{1s,1s} = ig\sqrt{s}(\rho_{1s,2s-1} - \rho_{1s-1,2s}) + \gamma\rho_{2s,2s} - \kappa(s\rho_{1s,1s} - (s+1)\rho_{1s+1,1s+1}) - P\rho_{1s,1s}, \tag{5.2.8}$$

$$\partial_t \rho_{2s,2s} = ig\sqrt{s+1}(\rho_{1s,2s+1} - \rho_{1s+1,2s}) - \gamma\rho_{2s,2s} - \kappa(s\rho_{2s,2s} - (s+1)\rho_{2s+1,2s+1}) + P\rho_{1s,1s}, \tag{5.2.9}$$

$$\partial_t \rho_{1s,2s-1} = ig\sqrt{s}(\rho_{1s,1s} - \rho_{2s-1,2s-1}) - ((\gamma + \kappa(2s-1) + P)/2)\rho_{2s,1s-1} + \kappa\sqrt{s(s+1)}\rho_{1s+1,2s} \tag{5.2.10}$$

The interaction parameterized by κ, γ, and P couple matrix elements with different photon occupation number s. This leads to an infinite set of differential equations which are truncated for numerical integration at a high value of s. The initial state is an empty cavity ($s = 0$) with the emitter in its ground state $|1\rangle$, i.e. $\rho_{10,10} = 1$. As mentioned previously, the basis states used for expansion is the product of the Fock states for photons and the $|1\rangle$ (ground) , $|2\rangle$ (excited) states for the two-level emitter. In this basis the density matrix ρ for the single emitter is of the form,

$$\rho = \begin{bmatrix} & |10\rangle & |20\rangle & |11\rangle & |21\rangle & |12\rangle & |22\rangle & . & . & |1s+1\rangle & |2s+1\rangle \\ \langle 10| & \rho_{10,10} & 0 & 0 & 0 & 0 & 0 & 0 & 0 & 0 & 0 \\ \langle 20| & 0 & \rho_{20,20} & \rho_{20,11} & 0 & 0 & 0 & 0 & 0 & 0 & 0 \\ \langle 11| & 0 & 0 & \rho_{11,20} & \rho_{11,11} & 0 & 0 & 0 & 0 & 0 & 0 \\ \langle 21| & 0 & 0 & 0 & \rho_{21,21} & \rho_{21,12} & 0 & 0 & 0 & 0 & 0 \\ \langle 12| & 0 & 0 & 0 & \rho_{12,21} & \rho_{12,12} & 0 & 0 & 0 & 0 & 0 \\ \langle 22| & 0 & 0 & 0 & 0 & 0 & \rho_{22,22} & . & 0 & 0 & 0 \\ . & . & . & . & . & . & . & . & . & . & . \\ . & . & . & . & . & . & . & . & . & . & . \\ \langle 1s+1| & 0 & 0 & 0 & 0 & 0 & 0 & 0 & 0 & \rho_{1s+1,1s+1} & 0 \\ \langle 2s+1| & 0 & 0 & 0 & 0 & 0 & 0 & 0 & 0 & 0 & \rho_{2s+1,2s+1} \end{bmatrix} \tag{5.2.11}$$

The first-order equations derived from the density matrix couples terms in a systematic way. Since there is no detuning, energy units of photons and emitters are the same. The terms $\rho_{1s,1s}$, $\rho_{2s-1,2s-1}$, $\rho_{1s,2s-1}$ and $\rho_{1s-1,2s}$ all have the same units of energy, i.e. s. More importantly the corresponding bra and ket component of an element has the same

energy. For example, $\rho_{1s-1,2s}$ has the same energy of s units for its $\langle 1s-1|$ and $|2s\rangle$. This principle holds for multiple emitters. An example of a density matrix element of a $N_e = 4$ two-level emitter system is $\langle 2121s|\,\rho\,|2221s-1\rangle$, where the first four numbers represent the states of the four emitters. This element is similar to the simple one emitter element, as it has equal energy in its bra and ket components and also couples with similar equal energy elements. The number of independent terms with equal energy in its bra and ket grows as 4^{N_e}. The equations (5.2.8-5.2.10) can be written in the matrix format and solved using Euler or RK4 integration. In matrix format

$$\begin{bmatrix} \dot{\rho}_{10,10} \\ \dot{\rho}_{20,20} \\ \dot{\rho}_{11,20} \\ \dot{\rho}_{20,11} \\ . \\ \dot{\rho}_{1s+1,1s+1} \\ \dot{\rho}_{2s+1,2s+1} \end{bmatrix} =$$

$$\begin{bmatrix} -P & \gamma & 0 & 0 & .. & 0 & 0 \\ P & -\gamma(1) & -ig & ig & .. & 0 & 0 \\ 0 & -ig\sqrt{1} & -\frac{1}{2}(\gamma+\kappa(2.1-1)+P) & 0 & .. & 0 & 0 \\ 0 & ig\sqrt{1} & 0 & -\frac{1}{2}(\gamma+\kappa(2.1-1)+P) & .. & 0 & 0 \\ . & . & . & . & . & . & . \\ 0 & 0 & 0 & 0 & 0 & 0 & 0 \\ 0 & 0 & 0 & 0 & 0 & 0 & 0 \end{bmatrix} \begin{bmatrix} \rho_{10,10} \\ \rho_{20,20} \\ \rho_{11,20} \\ \rho_{20,21} \\ . \\ \rho_{1s+1,1s+1} \\ \rho_{2s+1,2s+1} \end{bmatrix} \tag{5.2.12}$$

The matrix form of $\hat{\mathbf{L}}$ is shown explicitly for the equations that relate equal energy terms (equal energy in bra and ket). Note the arrangements of the terms in the vectors

containing the diagonal and off-diagonal density matrix elements. They are arranged in the sequence,

$$\begin{bmatrix} \rho_{10,10} \\ \rho_{20,20} \\ \rho_{11,20} \\ \rho_{20,11} \\ \rho_{11,11} \\ \rho_{21,21} \\ . \\ . \\ \rho_{1s+1,1s+1} \\ \rho_{2s+1,2s+1} \end{bmatrix} \tag{5.2.13}$$

So the four independent elements for the single two level emitter, 4^1 are $\rho_{1s,2s-1}$, $\rho_{2s-1,1s}$, $\rho_{1s,1s}$ and $\rho_{2s,2s}$, and this is exactly the sequence in which they are arranged in the vector. Note the first two terms are not allowed for $s = 0$ and hence not included. The set for $s = 1$ is however complete. If we treat this set of 4 elements as a unit cell, then the unit cell gets repeated for values of s from 0 to $s_{trunc} + 1$. The terms for the extra photon $s_{trunc} + 1$ after s_{trunc} is required for the boundary conditions. The equations for the unit cell of s photons is connected to the equations for the neighboring unit cells of $s + 1$ and $s - 1$ photons because of the nature of the actual transitions. Hence the elements of the last unit $s_{trunc} + 1$ is required, and their derivatives and initial values are set to zero, so that their values do not evolve and they truncate the problem. Now the fact that the unit cell of s photons connect to the unit cells of the neighboring photon numbers is used in allocating the coefficient matrix $\hat{\mathbf{L}}$. An element ρ_{1s2s-1}, has its allowed set of processes and the elements it connects to can be obtained from the original Master

equation, Eq.(5.2.4). This problem can be generalized for the multi-emitter case. For simplicity, lets consider equal energy elements or elements which have equal energy in their bra and ket. This set of independent equal energy elements form the basic unit cell, as was written out explicitly for the one-emitter case and their number for the general case is given by 4^{N_e}. So in this case, the vectors (Eq.(5.2.13)) are populated by repeating these basic units for increasing photon numbers ($s = 0, 1, 2, ..., s_{trunc}$). For example, for the two atom case there are 16 independent elements of the form, $\rho_{11s11s}, \rho_{22s,22s}$..... Now equations for individual elements in a unit connects to terms within its own unit and its nearest neighbors. So when an element is allowed a process via a stimulated emission or absorption, which conserves the total number of excitations, then it connects to elements within its own unit. However when the total excitation number changes by one unit, for processes such as pump, P, cavity decay, κ, and spontaneous emission, γ, then they connect with elements in the neighboring units. So for every allowed process we can set up a search space of three units $s-1$, s and $s+1$ to locate all the elements to which it connects. For example, in the one-emitter case if $s_{trunc} = 100$, then there are a total of $4 \times (100 + 1) + 2$ elements. So instead of trying to search in a space of 406 elements for the connecting element, the total search space is reduced to 4×3 = 12. This makes allocation of the coefficient matrix $\hat{\mathbf{L}}$ more efficient numerically. The location of the pump and the cavity loss elements are returned by the function, *operators3* allocating the coefficient matrix, so that for different pump values, only the particular locations of the matrix can be updated instead of constructing the whole thing all over. Such an approach is useful in computing steady state characteristics for multiple pump values. Also lower pump values have lower photon numbers for s_{trunc}. For a given set of pump values and for a fixed s_{trunc}, the entire matrix, $\hat{\mathbf{L}}$, is constructed only once for the first pump value and then the matrix is updated for the other pump values in the series.

Recognizing the independent elements in the unit cell of the density matrix for the

one emitter case is simple. However expanding this to the multi-emitter case requires a small algorithm. By using this we build the elements that make each unit cell for a given number of photons. Lets consider equal energy elements for the two emitter case. In the code we call this unit cell, *state-vector-frame*. This frame is a matrix containing the excitations and the photon numbers for a particular density matrix element in its rows. For example $\rho_{11s,12s-1}$, for a two emitter system is allocated a particular row in the unit cell as [1 1 s 1 2 $s-1$], where the excitations and photon numbers are arranged in the same order as the subscript of the element. In a particular row, for a general N_e emitter system, the first 1 to N_e elements denote excitations in the bra. The $(N_e+1)^{th}$ element denotes the photon number, the next N_e+2 to $2N_e+1$ elements are excitations of the ket and the $(2N_e+2)^{th}$ element denoting the photon number in the ket. The first two rows of the unit cell are [0 0 s 0 0 s] and [1 1 s 1 1 s] which are the all empty and all filled states. The maximum total emitter excitation, N_{ex} in a N_e emitter state is (0,1, 2,....N_e). Now the $N_{ex}=0$ ([0 0]) and the $N_{ex}=2$ ([1 1]) states are already accounted. The other possibility is 1 excitation, which gives possible states [0 1] and [1 0]. So, in general, to obtain k excitations in N_e available positions the number of choices are $\binom{N}{k}$ and MATLAB prints out the configuration of these individual choices using the command *nchoosek*. In the 2-emitter case the choices are [0 1 s 0 1 s] and [1 0 s 1 0 s]. So we have a set of elements with same bra and ket and they form the diagonal elements which in general is of number 2^{N_e}. We also save the emitter parts of these kets $|11\rangle, |22\rangle, |12\rangle$ and $|21\rangle$ for further mixing in a matrix called *vector-store*. Now we construct the elements of the unit cell which are asymmetric, but of equal energy ($\rho_{21s,12s}$). This is obtained by combining the elements of *vector-store* amongst each other. If the number of elements in *vector-store* is given by D, then the possible choices is given by $2\binom{D}{2}$ since you combine two different elements (bra and ket) to get a full element and the 2 takes care of the complex conjugate that arises in

the asymmetric terms. The command $nchoosek(1:1:\mathrm{D},2)$ prints out the possible combinations between the different rows of *vector-store*, for example an output [1 2] means row 1 would make the bra and row 2 would make the ket for an element i.e. $\langle 00s|\,\rho\,|11s'\rangle$ for the two-emitter case. These possible combination indices are stored in rows of the matrix *photon-diff-states-mat*. Each combination row gives rise to two elements which are complex conjugates of each other. Now we should remember that the equal energy condition should not be violated in creating these independent density matrix elements. However for the 2-emitter example considered, $\langle 00s|\,\rho\,|11s'\rangle$, the net emitter excitation in the bra is 0 and in the ket is 2. This is now made equal in energy

with the help of the photons s and s'. To compensate in this case s' is set to $s-2$. Thus by collecting all the elements we can write the unit cell in the two-emitter case as

$$\begin{bmatrix} \rho_{11s,11s} \\ \rho_{11s,22s} \\ \rho_{12s,12s} \\ \rho_{21s,21s} \\ \rho_{11s,22s-2} \\ \rho_{22s-2,11s} \\ \rho_{11s,12s-1} \\ \rho_{12s-1,11s} \\ \rho_{11s,21s-1} \\ \rho_{21s-1,11s} \\ \rho_{22s,12s-1} \\ \rho_{12s-1,22s} \\ \rho_{22s,21s-1} \\ \rho_{21s-1,22s} \\ \rho_{21s,12s} \\ \rho_{12s,21s} \end{bmatrix} = \begin{bmatrix} 1 & 1 & s & 1 & 1 & s \\ 2 & 2 & s & 2 & 2 & s \\ 2 & 1 & s & 2 & 1 & s \\ 1 & 2 & s & 1 & 2 & s \\ 1 & 1 & s & 2 & 2 & s-2 \\ 2 & 2 & s-2 & 1 & 1 & s \\ 1 & 1 & s & 1 & 2 & s-1 \\ 1 & 2 & s-1 & 1 & 1 & s \\ 1 & 1 & s & 2 & 1 & s-1 \\ 2 & 1 & s-1 & 1 & 1 & s \\ 2 & 2 & s & 1 & 2 & s-1 \\ 1 & 2 & s-1 & 2 & 2 & s \\ 2 & 2 & s & 2 & 1 & s-1 \\ 2 & 1 & s & 1 & 2 & s \\ 1 & 2 & s & 2 & 1 & s \end{bmatrix} \tag{5.2.14}$$

This unit cell is stored as $state-vector-frame$ (Right hand side of Eq.(5.2.14)) and is repeated for photon numbers s equal to 0 to $s_{trunc}+1$, in order to get the total $state-vector$. After constructing this, rows containing negative photon numbers in their bra ($(N_e+1)^{th}$) or ket ($2(N_e+1)^{th}$) are eliminated. Locating the diagonal elements, such as ρ_{11s11s}, is essential for calculating expectation values. This can be done easily. Just subtract the first N_e+1 elements (bra) from the second N_e+1 elements, take the absolute values and sum the arrays (row-wise). Only diagonal elements give

zero. The master equations may be used to compute the dynamics of expectation values of any system operators. The evaluation of the diagonal elements allows calculation of steady-state properties and single time averages of operators. The important photon field-field and intensity-intensity correlation are

$$g^1(t,\tau) = \langle a^\dagger(t)a(t+\tau)\rangle \tag{5.2.15}$$

$$g^2(t,\tau) = \langle a^\dagger(t)a^\dagger(t+\tau)a(t+\tau)a(t)\rangle \tag{5.2.16}$$

In steady-state these correlations do not depend on time t and can be evaluated using

$$\langle a^\dagger(t)a(t+\tau)\rangle = \mathrm{Tr}[ae^{\hat{\mathbf{L}}\tau}[\rho_s a^\dagger]] \tag{5.2.17}$$

$$\langle a^\dagger(t)a^\dagger(t+\tau)a(t+\tau)a(t)\rangle = \mathrm{Tr}[a^\dagger ae^{\hat{\mathbf{L}}\tau}[a\rho_s a^\dagger]] \tag{5.2.18}$$

which is valid for Markovian systems [Ref. [26]] (See Appendix A for details). Here, ρ_s is the steady-state solution of the master equation Eq.(5.2.5) and $\hat{\mathbf{L}}$ is the time-evolution operator of the density matrix.

The coupled density matrix equations, for the single-emitter case, used to obtain the first-order correlation function $g^1(t,\tau)$ are

$$\begin{aligned}\partial_t\rho_{1s+1,1s} &= ig(\sqrt{s}\rho_{1s+1,2s-1} - \sqrt{s+1}\rho_{2s,1s}) + \gamma\rho_{2s+1,2s} - P\rho_{1s+1,1s} \\ &+ \frac{\kappa}{2}(2\sqrt{(s+1)(s+2)}\rho_{1s+2,1s+1} - (2s+1)\rho_{1s+1,1s}),\end{aligned} \tag{5.2.19}$$

$$\begin{aligned}\partial_t\rho_{2s+1,2s} &= ig(\sqrt{s+1}\rho_{2s+1,1s+1} - \sqrt{s+2}\rho_{1s+2,2s}) - \gamma\rho_{2s+1,2s} + P\rho_{1s+1,1s} \\ &+ \frac{\kappa}{2}(2\sqrt{(s+1)(s+2)}\rho_{2s+2,2s+1} - (2s+1)\rho_{2s+1,2s}), \end{aligned} \tag{5.2.20}$$

$$\begin{aligned}\partial_t\rho_{2s,1s} &= ig(\sqrt{s}\rho_{2s,2s-1} - \sqrt{s+1}\rho_{1s+1,1s}) - ((\gamma + 2s\kappa + P)/2)\rho_{2s,1s} \\ &+ \kappa(s+1)\rho_{2s+1,1s+1} \end{aligned} \tag{5.2.21}$$

and

$$\begin{aligned}\partial_t\rho_{1s+1,2s-1} &= ig(\sqrt{s}\rho_{1s+1,1s} - \sqrt{s+1}\rho_{2s,2s-1}) - ((\gamma + 2s\kappa + P)/2)\rho_{1s+1,2s-1} \\ &+ \kappa\sqrt{s(s+2)}\rho_{1s+2,2s} \end{aligned} \tag{5.2.22}$$

The terms $\rho_{1s+1,1s}$, $\rho_{2s+1,2s}$, $\rho_{2s,1s}$ and $\rho_{1s+1,2s-1}$ all have the same units of energy, s and $s+1$ in their bra and ket components respectively. Similar terms are coupled to each other and the same principle is obeyed when more emitters are added. The location of these elements in the density matrix is shown in Eq. (5.2.23),

$$\rho = \begin{bmatrix} 0 & 0 & 0 & 0 & 0 & 0 & 0 & 0 & 0 & 0 \\ \rho_{20,10} & 0 & 0 & 0 & 0 & 0 & 0 & 0 & 0 & 0 \\ \rho_{11,10} & 0 & 0 & 0 & 0 & 0 & 0 & 0 & 0 & 0 \\ 0 & \rho_{21,20} & \rho_{21,11} & 0 & 0 & 0 & 0 & 0 & 0 & 0 \\ 0 & \rho_{12,20} & \rho_{12,11} & 0 & 0 & 0 & 0 & 0 & 0 & 0 \\ 0 & 0 & 0 & \rho_{22,21} & \rho_{22,12} & 0 & 0 & 0 & 0 & 0 \\ . & . & . & . & . & . & . & . & . & . \\ . & . & . & . & . & . & . & . & . & . \\ 0 & 0 & 0 & 0 & 0 & 0 & . & . & 0 & 0 \\ 0 & 0 & 0 & 0 & 0 & . & . & 0 & \rho_{2s+1,1s+1} & 0 \end{bmatrix} \tag{5.2.23}$$

These terms are different from the terms that we solved using Eqs.(5.2.8-5.2.9). The current terms are not equal energy elements. Since these terms are initially equal to zero, their time-evolution should not evolve their values. Eqn 5.2.17, shows the operator $a^\dagger$ acting on ρ, from the left and the product matrix $\rho a^\dagger$ is time evolved by $\hat{\mathbf{L}}$. Now the form of the a and $a^\dagger$ operator, in the given basis is

$$a = \begin{bmatrix} 0 & 0 & \sqrt{1} & 0 & 0 & 0 & 0 & 0 & 0 & 0 \\ 0 & 0 & 0 & \sqrt{1} & 0 & 0 & 0 & 0 & 0 & 0 \\ 0 & 0 & 0 & 0 & \sqrt{2} & 0 & 0 & 0 & 0 & 0 \\ 0 & 0 & 0 & 0 & 0 & \sqrt{2} & 0 & 0 & 0 & 0 \\ 0 & 0 & 0 & 0 & 0 & 0 & 0 & 0 & 0 & 0 \\ 0 & 0 & 0 & 0 & 0 & 0 & 0 & 0 & 0 & 0 \\ . & . & . & . & . & . & . & . & . & . \\ . & . & . & . & . & . & . & . & . & . \\ 0 & 0 & 0 & 0 & 0 & 0 & . & . & 0 & 0 \\ 0 & 0 & 0 & 0 & 0 & 0 & . & . & 0 & 0 \end{bmatrix} \tag{5.2.24}$$

$$a^\dagger = \begin{bmatrix} 0 & 0 & 0 & 0 & 0 & 0 & 0 & 0 & 0 & 0 \\ 0 & 0 & 0 & 0 & 0 & 0 & 0 & 0 & 0 & 0 \\ \sqrt{1} & 0 & 0 & 0 & 0 & 0 & 0 & 0 & 0 & 0 \\ 0 & \sqrt{1} & 0 & 0 & 0 & 0 & 0 & 0 & 0 & 0 \\ 0 & 0 & \sqrt{2} & 0 & 0 & 0 & 0 & 0 & 0 & 0 \\ 0 & 0 & 0 & \sqrt{2} & 0 & 0 & 0 & 0 & 0 & 0 \\ . & . & . & . & . & . & . & . & . & . \\ . & . & . & . & . & . & . & . & . & . \\ 0 & 0 & 0 & 0 & 0 & 0 & . & . & 0 & 0 \\ 0 & 0 & 0 & 0 & 0 & 0 & . & . & 0 & 0 \end{bmatrix} \tag{5.2.25}$$

The density matrix in steady-state is given by Eq.(5.2.11) in the matrix form. This ρ when acted upon by $a^\dagger$ from the right reaches the form

$$(\rho a^\dagger) = \begin{bmatrix} 0 & 0 & 0 & 0 & 0 & 0 & 0 & 0 & 0 & 0 \\ 0 & 0 & 0 & 0 & 0 & 0 & 0 & 0 & 0 & 0 \\ \sqrt{1}\rho_{11,01} & 0 & 0 & 0 & 0 & 0 & 0 & 0 & 0 & 0 \\ 0 & \sqrt{1}\rho_{21,21} & \sqrt{2}\rho_{21,12} & 0 & 0 & 0 & 0 & 0 & 0 & 0 \\ 0 & \sqrt{1}\rho_{12,21} & \sqrt{2}\rho_{12,12} & 0 & 0 & 0 & 0 & 0 & 0 & 0 \\ 0 & 0 & 0 & \sqrt{2}\rho_{22,22} & 0 & 0 & 0 & 0 & 0 & 0 \\ . & . & . & . & . & . & . & . & . & . \\ . & . & . & . & . & . & . & . & . & . \\ 0 & 0 & 0 & 0 & 0 & 0 & . & . & 0 & 0 \\ 0 & 0 & 0 & 0 & 0 & . & . & 0 & 0 & 0 \end{bmatrix} \tag{5.2.26}$$

which is very similar to the form ρ given by Eq.(5.2.23). Thus after solving Eq.5.2.11 to the steady state, we multiply it with $a^\dagger$ and that gives us Eq.(5.2.26) which populates the same elements present in ρ (Eq.(5.2.23)), and hence the initial value of these elements from which it can be time evolved using Eqs.(5.2.19-5.2.22). These equations, similar to Eqs.(5.2.8-5.2.10), can be written in the matrix form as

$$\begin{bmatrix} \dot{\rho}_{11,10} \\ \dot{\rho}_{21,20} \\ \dot{\rho}_{21,11} \\ . \\ . \\ \dot{\rho}_{1s+2,1s+1} \\ \dot{\rho}_{2s+2,2s+1} \end{bmatrix} = \begin{bmatrix} -\frac{\kappa}{2} - P & \gamma & -ig\sqrt{1} & . & . & 0 & 0 \\ P & -\frac{\kappa}{2} - \gamma & 0 & . & . & 0 & 0 \\ -ig\sqrt{1} & 0 & -\frac{1}{2}(\gamma + \kappa(2.0-1) + P) & . & . & 0 & 0 \\ . & . & . & . & . & . & . \\ . & . & . & . & . & . & . \\ 0 & 0 & 0 & 0 & 0 & 0 & 0 \\ 0 & 0 & 0 & 0 & 0 & 0 & 0 \end{bmatrix} \begin{bmatrix} \rho_{11,10} \\ \rho_{21,20} \\ \rho_{21,11} \\ . \\ . \\ \rho_{1s+2,1s+1} \\ \rho_{2s+2,2s+1} \end{bmatrix} \tag{5.2.27}$$

Note that the matrix form of $\hat{\mathbf{L}}$ has changed as it is coupling this new set of elements. Now these elements are also arranged in the same way as before for the elements in Eqs.(5.2.8-5.2.10). These elements have one unit of energy more in their bra as compared to their ket. The independent elements for the one emitter case are $\rho_{1s+1,1s}$, $\rho_{2s+1,2s}$, $\rho_{2s,1s}$, and $\rho_{1s+1,2s-1}$. These set of elements form a unit cell and the number of elements in the unit cell is given by 4^{N_e} for the general N_e emitter case. Now if this unit is repeated by increasing the photon number s by 1 each time, then we can arrange the elements in a vector in the same way. This arrangement, and the nature of the physical processes, ensures that the elements of each unit cell connects to the elements of its own cell and its nearest neighbors. Hence the search space for allocating the coefficients of a matrix element ($\rho_{1s+1,1s}$) obtained from Eq.5.2.4 is reduced to a great extent. The state vector of these unequal energy elements can be created from the previous state vector

by adding a single photon or incrementing the energy by one unit in every element of the bra, i.e

$$\begin{bmatrix} \rho_{10,10} \\ \rho_{20,20} \\ \rho_{11,20} \\ \rho_{20,11} \\ . \\ . \\ \rho_{1s+1,1s+1} \\ \rho_{2s+1,2s+1} \end{bmatrix} \rightarrow \begin{bmatrix} \rho_{11,10} \\ \rho_{21,20} \\ \rho_{12,20} \\ \rho_{21,11} \\ . \\ . \\ \rho_{1s+2,1s+1} \\ \rho_{2s+2,2s+1} \end{bmatrix} \tag{5.2.28}$$

After the time evolution of the product, $\rho a^\dagger$ for time τ, the a operator acting on the product of $\rho a^\dagger$ brings back the diagonal which is then summed to obtain $g^1(t,\tau)$. In matrix form, $a\rho a^\dagger$ is

$$\begin{bmatrix} \sqrt{1^2}\rho_{11,11} & 0 & 0 & 0 & 0 & 0 & 0 & 0 & 0 & 0 \\ 0 & \sqrt{1^2}\rho_{21,21} & \sqrt{1.2}\rho_{21,12} & 0 & 0 & 0 & 0 & 0 & 0 & 0 \\ 0 & \sqrt{1.2}\rho_{12,21} & \sqrt{2^2}\rho_{12,12} & 0 & 0 & 0 & 0 & 0 & 0 & 0 \\ 0 & 0 & 0 & \sqrt{2^2}\rho_{22,22} & \sqrt{2.3}\rho_{22,13} & 0 & 0 & 0 & 0 & 0 \\ 0 & 0 & 0 & \sqrt{2.3}\rho_{13,22} & \sqrt{3^2}\rho_{13,13} & 0 & 0 & 0 & 0 & 0 \\ 0 & 0 & 0 & 0 & 0 & \sqrt{3^2}\rho_{23,23} & . & . & 0 & 0 \\ . & . & . & . & . & . & . & . & . & . \\ . & . & . & . & . & . & . & . & . & . \\ 0 & 0 & 0 & 0 & 0 & 0 & 0 & 0 & 0 & 0 \\ 0 & 0 & 0 & 0 & 0 & 0 & 0 & 0 & 0 & 0 \end{bmatrix} \tag{5.2.29}$$

Likewise, the operation $a\rho a^{\dagger}$ produces equations coupling terms similar to Eqs.(5.2.8 - 5.2.10) because of the two operations on the density matrix, ρ (Eq.(5.2.11)) produces a similar matrix form (Eq.(5.2.29)). This product matrix is time evolved by $\hat{\mathbf{L}}$, which is of the same form as Eq.5.2.12. Eq.5.2.29 produces the initial value starting from Eq.(5.2.11). The operator $a^{\dagger}a$ is diagonal and affects only the diagonal elements which are summed over after the product. There is another non-triviality which arises in allocating the initial values in the matrix ρ used in line-width calculations. While constructing the *state-vector* the 2^N independent basis vectors ($|00s\rangle$, $|11s\rangle$, $|01s\rangle$, $|00s\rangle$, for the two emitter case), is stored in a matrix called $basis - vector - frame$. This is a matrix in which each row represents a basis state. Since ρ, a and $a^{\dagger}$ are all represented in this basis, we can create an entire basis set by filling out a matrix (*basis-states*) with the unit

basis-vector-frame, repeated sequentially for increasing photon numbers. In the matrix form,

$$basis-states = \begin{bmatrix} 1 & 1 & 0 & 1 & 1 & 0 \\ 2 & 2 & 0 & 2 & 2 & 0 \\ 2 & 1 & 0 & 2 & 1 & 0 \\ 1 & 2 & 0 & 1 & 2 & 0 \\ 1 & 1 & 1 & 1 & 1 & 1 \\ 2 & 2 & 1 & 2 & 2 & 1 \\ 2 & 1 & 1 & 2 & 1 & 1 \\ 1 & 2 & 1 & 1 & 2 & 1 \\ . & & & & & \\ . & & & & & \\ 1 & 1 & s & 1 & 1 & s \\ 2 & 2 & s & 2 & 2 & s \\ 2 & 1 & s & 2 & 1 & s \\ 1 & 2 & s & 1 & 2 & s \end{bmatrix} \tag{5.2.30}$$

Now since each row of the *state-vector* contains the bra and ket component of the elements of the density matrix that we are solving for, they can be allocated easily in the matrix form of ρ which is required for performing the product, $\rho a^{\dagger}$. The photon number in the bra and the ket component of every element of the $state - vector$ is known and is given by the $N+1$ and the $2(N+1)$ columns of a particular row. For example, in the 2 emitter case, the coordinates of the element $\rho_{001,100}$ is stored in a *state-vector* row as [0 0 1 1 0 0]. As the basis states in the matrix *basis-states* are also arranged in order of increasing photon number, the search space for finding the location of the element $\rho_{001,100}$ in the ρ matrix form can be confined to the section of basis states from 0 to 1 photons. Once the location is determined, the row information and column information

of the matrix is stored in the two vectors *row-rho* and *col-rho* respectively. An inverse process is required for allocating the matrix elements of the product matrix $\rho a^\dagger$ in a vector form for time propagation using Eq.(5.2.27). This is done in the same way. The new *state-vector*, shown in Eq.(5.2.28) however contains unequal energy elements. But since the bra and ket components are similarly given by every row, their values can be located using the same technique in the product matrix $\rho a^\dagger$. The row and the column information of these elements in the product matrix $\rho a^\dagger$ is stored in vectors *row-rho1* and *col-rho1* respectively and can be recalled for future allocations as the element order in the *state-vector* is unchanged for a given truncation photon number.

The photon field-field correlation gives information on phase fluctuations and the frequency spectrum of emitted light, $S(\nu)$, may be obtained from Fourier transform

$$S(\nu) = \frac{1}{\pi}\mathrm{Re}\int_0^\infty \mathrm{d}\tau \mathrm{e}^{\mathrm{i}\nu\tau} g^1(t,\tau) \tag{5.2.31}$$

The intensity-intensity correlation gives information on photon number statistics. Phenomena such as non-classical states or anti-bunching may be investigated using this correlation. For zero delay ($\tau = 0$) the normalized second-order correlation obtained from Eq.(5.2.16) is

$$G^2(\tau = 0) = \frac{\left\langle \mathrm{a}^\dagger \mathrm{a}^\dagger \mathrm{a}\mathrm{a} \right\rangle}{\left\langle \mathrm{a}^\dagger \mathrm{a} \right\rangle^2} = \frac{\sum_\mathrm{s} \mathrm{s}(\mathrm{s}-1)(\rho_{2\mathrm{s},2\mathrm{s}} + \rho_{1\mathrm{s},1\mathrm{s}})}{(\sum_\mathrm{s} \mathrm{s}(\rho_{2\mathrm{s},2\mathrm{s}} + \rho_{1\mathrm{s},1\mathrm{s}}))^2} \tag{5.2.32}$$

The Fano-factor, or normalized variance, may also be used as a measure of photon number fluctuations and is given by

$$F = \frac{\langle s^2 \rangle - \langle s \rangle^2}{\langle s \rangle} \tag{5.2.33}$$

where s is the cavity photon number.

5.3 Scaling of lasers

5.3.1 Single emitter

We begin by analyzing the case of a single two-level emitter in a lasing cavity. Figure 5.2 illustrates the steady-state behavior of a single emitter for different cavity losses as a function of the incoherent pump rate. Parameters used scale within a range corresponding to very recent experiments on single quantum dot [Ref. [28]] and single ion [[Ref. [29]] lasers. The cavity with the highest optical Q stores the maximum number of photons and two distinct peaks in the Fano-factor are predicted [Ref. [31]]. As shown in Fig. 5.2(c), the strong photon number fluctuations experienced by the system near lasing threshold pump rates gives rise to the first Fano-factor peak at low pump rates. The second peak appears due to self-quenching [Ref. [31, 32]] at larger pump rates. This occurs when correlations required for lasing are destroyed by a strong incoherent pump and the effective gain is insufficient to overcome the cavity losses [Ref. [31]]. Thus, as the system undergoes self-quenching, the cavity fails to store lasing photons due to the presence of a strong incoherent pump and the photon field experiences strong fluctuations. Increasing cavity loss reduces the number of cavity photons and the two peaks in the Fano-factor collapse to a single peak. A value of Fano-factor or normalized second-order correlation $G^2(\tau = 0)$ less than unity signifies amplitude non-classical light which may exist when there is high cavity loss and low pump rate [Ref. [30]].

The inversion of the single emitter shown in Fig. 5.2(b) has a region of low slope in the presence of large photon number before it saturates completely. This is a signature of the carrier-pinning process that occurs in large conventional laser diodes when driven above threshold. However, in a single emitter laser, the onset of self-quenching due to incoherent pumping destroys the coherence and reduces the effective gain. The

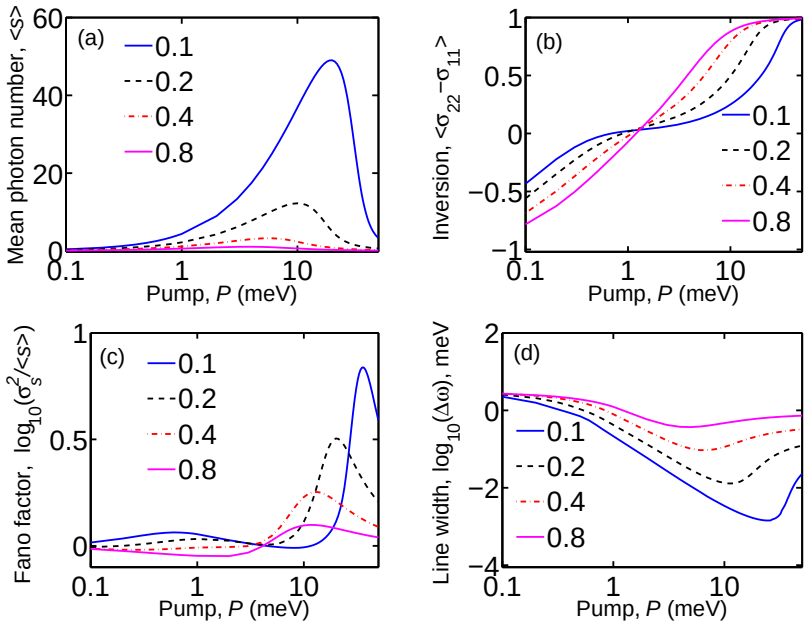

Figure 5.2: Variation of steady-state properties of a single two-level emitter coupled to a cavity field with incoherent pump rate, P, for the indicated values of cavity loss rate κ (meV). (a) Mean photon number in lasing mode. (b) Inversion of emitter showing significant signature of inversion pinning for low optical loss $\kappa = 0.1$ meV. (c) Fano-factor for photon number, s. Laser threshold corresponds to broad peak near $P = 1$ meV for $\kappa < 0.8$ meV. Peak due to self-quenching occurs for $P > 10$ meV. (d) Spectral line width. The pump axis is in $\log_{10}$ scale. Dark solid line (κ = 0.1 meV), dotted line (κ = 0.2 meV), dash-dotted line (κ = 0.4 meV), light solid line (κ = 0.8 meV). Parameters : $g = 1$ meV, $\gamma = 0.1$ meV, $\omega = 1000$ meV.

system tries to compensate by increasing its inversion, fails, and dissipates energy by spontaneously emitting into modes other than the lasing mode.

As is characteristic of lasing behavior, the spectral line width of the photon field reduces with increasing number of cavity photons. The cavity with the lowest loss can attain the smallest line width. Far below threshold the line width is large because of the presence of a non-inverted absorbing medium [Ref. [31]]. As shown in (Fig. 5.2(d)) the line width decreases with increasing number of cavity photons. As the system starts self-quenching the line width increases, asymptotically approaching the empty cavity line width.

5.3.2 Multiple emitters

Results of our calculations shown in Fig. 5.3 confirm a previous suggestion [Ref. [32]] that adding emitters that act as independent sources coupled by the photon field is equivalent to making the cavity-emitter coupling, g, stronger. Enhanced coupling provides more emission into the lasing mode and self-quenching occurs at larger values of pump. As more emitters are added the position of the two peaks in the Fano-factor become more widely separated in pump rate. In presence of a large number of photons and as more emitters are added, self-quenching occurs and the position of the two peaks in the Fano-factor become more widely separated in pump rate. In Fig. 5.3 the steady-state behavior is plotted against the normalized pump rate (the actual pump energy flowing into the system is obtained by multiplying the normalized value, P, by the number of emitters, N_e).

Due to a stronger effective coupling the peak that occurs at a smaller pump rate shifts to lower pump rate with increasing number of emitters. Also, with increasing number of emitters, self-quenching occurs at higher values of normalized pump rate because photons generated by a given emitter induce transitions in other emitters. Similarly for inversion, the device with the largest number of emitters has the strongest pinning.

5.3.3 Semiclassical rate equations derived from quantum master equations

We now compare the full quantum calculations with the steady-state values predicted by semiclassical rate equations. Here, the $semiclassical\ \ rate\ \ equations$ are derived from the quantum master equations under an approximation in which correlations between emitter and photon operators are factorized. This factorization approximation is valid in the presence of large photon numbers.

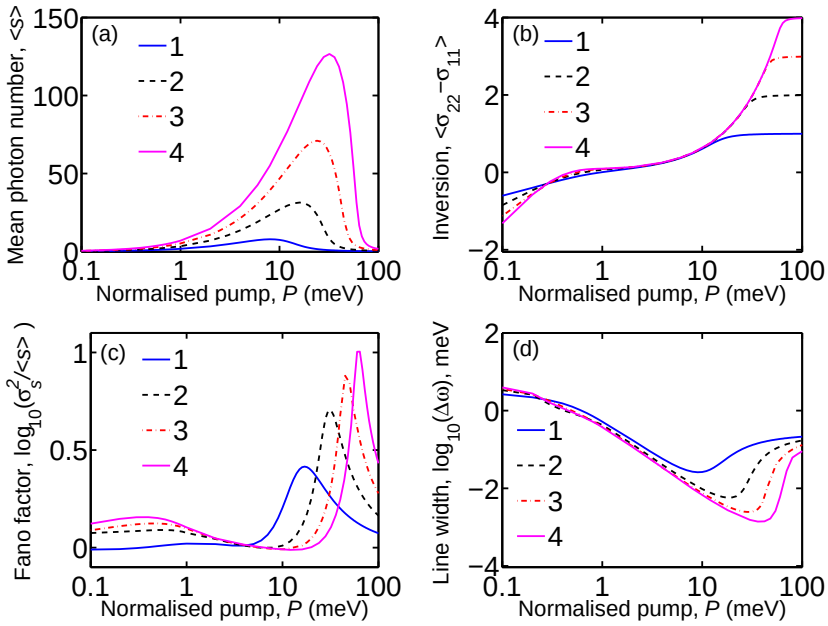

Figure 5.3: Variation of steady-state properties of multiple two-level emitters coupled to a cavity field with incoherent pump P. (a) Mean photon number in lasing mode. (b) Net inversion of emitters. (c) Fano-factor. (d) Spectral line width. Laser threshold corresponds to broad peak with $P < 1$ meV. Peak due to self-quenching occurs when $P > 10$ meV. (d) Spectral linewidth. The pump axis is in $\log_{10}$ scale. Behavior for different number of emitters is compared. Dark solid line (N_e = 1), dotted line (N_e = 2), dash-dotted line (N_e = 3), light solid line (N_e = 4). Parameters are as in Fig. 5.2 : $g = 1$ meV, $\gamma = 0.1$ meV, $\omega = 1000$ meV, $\kappa = 0.25$ meV.

For any system operator O, the equation governing its expectation value can be derived from the quantum master equation, [Ref. [32]]

$$\frac{d\langle O\rangle}{dt} = -\frac{i}{\hbar}\langle[O,H]\rangle + Tr(OL\rho) \tag{5.3.1}$$

For system operators $s = a^\dagger a$, a, ${\sigma_k}^\dagger$ and σ_{zk}, the equations are as follows,

$$\frac{d\langle s\rangle}{dt} = -\frac{i}{\hbar}\sum_k g_k[\langle\sigma_k a^\dagger\rangle - \langle a{\sigma_k}^\dagger\rangle] - \kappa\langle s\rangle, \tag{5.3.2}$$

$$\frac{d\langle\sum_i \sigma_{zk}\rangle}{dt} = \frac{k}{\hbar}\sum_k 2g_k[\langle\sigma_k a^\dagger\rangle - \langle a{\sigma_k}^\dagger\rangle] - (\gamma+P)\sum_k\langle\sigma_{zk}\rangle + N_a(P-\gamma), \tag{5.3.3}$$

$$\frac{d\langle a\rangle}{dt} = -\frac{k}{\hbar}\sum_i g_k\langle\sigma_k\rangle - \frac{\kappa}{2}\langle a\rangle, \tag{5.3.4}$$

$$\frac{d\langle{\sigma_k}^\dagger\rangle}{dt} = -\frac{k}{\hbar}g_k\langle\sigma_{zk}a^\dagger\rangle - \frac{\gamma+P}{2}\langle{\sigma_k}^\dagger\rangle \tag{5.3.5}$$

where σ_{zk} is the inversion of the k^{th} emitter. These equations and its complex conjugates on being solved in steady-state yield mean cavity photon number $\langle s\rangle$ and net inversion above threshold $\langle\sum_k \sigma_{zk}\rangle$

$$\langle s\rangle = \frac{1}{2\kappa}(N_a(P-\gamma) - \kappa(\frac{\hbar(\gamma+P)}{2g})^2), \tag{5.3.6}$$

$$\langle\sum_k \sigma_{zk}\rangle = \frac{\hbar^2\kappa(\gamma+P)}{4g^2} \tag{5.3.7}$$

As shown in the previous section, more emitters lead to more photons in the cavity and hence a better agreement is observed with the semiclassical predictions. This is similar to increasing the cavity-emitter coupling, g, which also leads to more photons in the cavity.

The parameters in Fig. 5.4 are modified to produce a larger laser threshold compared to Fig. 5.3. This is done by enhancing the spontaneous emission rate γ into non-lasing modes. The cavity with a single emitter supports a single peak in the Fano-factor. Increasing γ reduces the effective gain [Ref. [31]], which leads to a smaller number of photons in the lasing cavity.

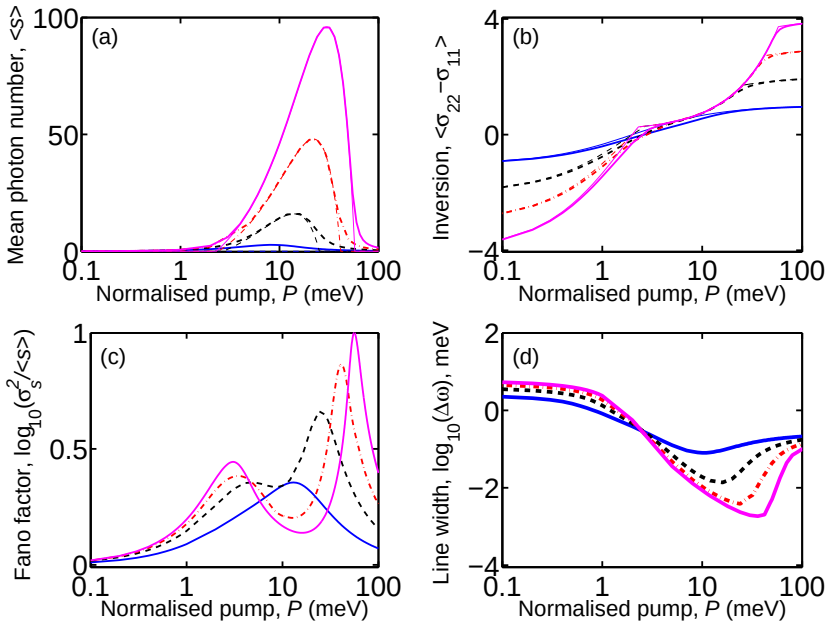

Figure 5.4: Comparison of steady-state properties derived from semiclassical rate equations and the full quantum theory. (a) Mean photon number in lasing mode. (b) Net inversion of emitters. (c) Fano-factor. Threshold for $N_e \geq 2$ corresponds to peak near $P = 3$ meV and peak due to self-quenching occurs for $P > 20$ meV. (d) Spectral line width. The pump axis is in $\log_{10}$ scale. Behavior for different number of emitters is compared. Dark solid line (N_e = 1), dotted line (N_e = 2), dash-dotted line (N_e = 3), light solid line (N_e = 4). The thicker lines denote quantum calculations and the corresponding thinner lines denote semiclassical calculations. Parameters : $g = 1$ meV, $\gamma = 2$ meV, $\omega = 1000$ meV, $\kappa = 0.25$ meV.

There is good agreement between the predictions of the full quantum theory and the semi-classical rate equations in regions of large photon numbers as shown by Fig. 5.4(a) and (b). Disagreement is found near lasing threshold and self-quenching because the factorization approximation fails when average photon numbers are small.

5.3.4 Semiclassical master equations

It is interesting to compare the predictions of the full quantum calculations with those of the *semiclassical master equations* developed in [Ref. [34, 35]]. Figure 5.5 shows transitions out of (n, s) in the $n-s$ state-space where n is the discrete number of excited

electronic states in the cavity and s denotes the number of photons. Trajectories of a biased random walk in $n-s$ state-space are used to sample solutions to the semiclassical master equations.

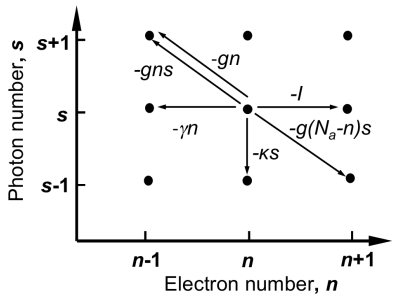

Figure 5.5: Transition rates out of state (n, s). g is the dipole coupling constant, $-gns$ is the stimulated emission rate in the system at photon energy $\hbar\omega$, $-g(N_e - n)s$ is the stimulated absorption rate where N_e is the maximum number of emitters, γ is the spontaneous emission rate into modes other than the cavity mode and κ is the total optical loss rate from the cavity. I is the excited state injection (pump) rate.

The random walk calculations are modified in the sense that the number of emitters or excited states in the cavity is limited. So current can only pump the system if emitter excitation is possible. The semiclassical master equations account for energy and particle number conservation but they do not include phase fluctuations and hence cannot reproduce the effects of self-quenching which occurs due to suppression of coherence. However, the method predicts enhanced photon fluctuations around threshold quantified by the Fano-factor after which, with increasing pump rate, the excitation gets pinned and the cavity photon number increases. Figure 5.6 compares semiclassical master equation behavior with the full quantum model and shows good agreement near the threshold region before onset of quenching. The net excitation is partially pinned at similar values of pump rate predicted by the semiclassical calculations (Fig. 5.6(b)). The location of the lasing threshold pump rate, as determined by the first peak in the Fano-factor, is also

in close agreement with the semiclassical calculations (Fig. 5.6(c)). These results validate the assumption that particle number quantization captures much of the full quantum model of multi-emitter meso-lasers [Ref. [34, 35]] for pump rates below the onset of self-quenching. There is somewhat less agreement for the case of a single emitter indicating that it is more sensitive to complete field quantization compared to the multi-emitter case.

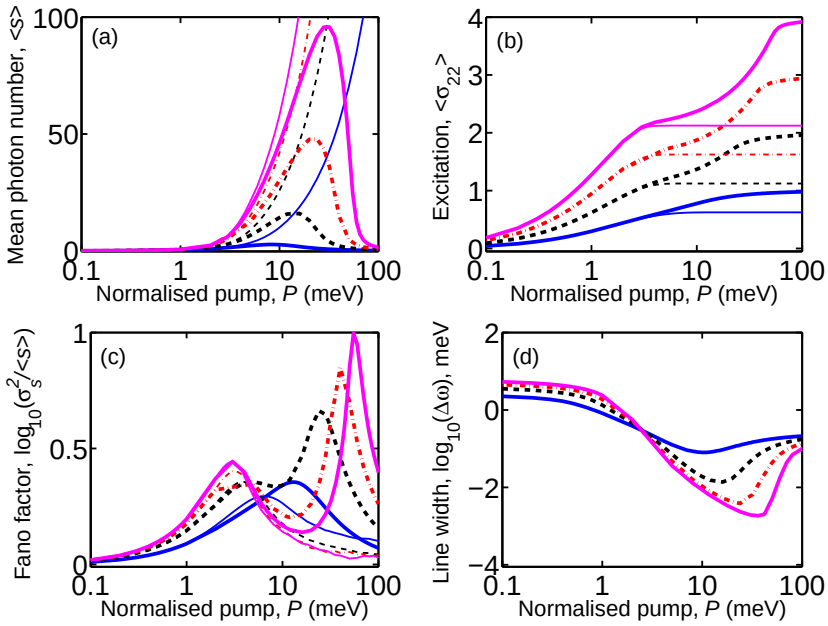

Figure 5.6: Comparison of steady-state properties derived from semiclassical master equations and the full quantum theory for different numbers of emitters. (a) Mean photon number in lasing mode. (b) Net inversion of emitters. (c) Fano-factor. Laser threshold for $N_e \geq 2$ corresponds to broad peak near $P = 3$ meV and self-quenching, which is a pure quantum effect, occurs for $P > 20$ meV. (d) Spectral line width. The pump axis is in $\log_{10}$ scale. Dark solid line (N_e = 1), dotted line (N_e = 2), dash-dotted line (N_e = 3), light solid line (N_e = 4). The thicker lines denote quantum calculations and the corresponding thinner lines denote semi-classical master equation calculations. Parameters are as in Fig. 5.4 : $g = 1$ meV, $\gamma = 2$ meV, $\omega = 1000$ meV, $\kappa = 0.25$ meV.

The semiclassical master equation predictions of lasing suppression around threshold and the associated excited electronic state depinning around threshold found in Ref. [[34, 35]] is however absent in the full quantum model for N_e identical emitters. This is

because, in a homogeneous quantum system, spontaneous emission into the lasing mode has the same coefficient as the net stimulated gain term in the presence of one photon [Ref. [45, 46, 47, 48]]. The semiclassical master equation is not constrained in this way and the stimulated gain and spontaneous emission into the lasing mode are taken as independent phenomenological parameters [Ref. [24, 44, 49]]. The effects of lasing suppression and bimodal probability distributions may be captured in the full quantum model by including a saturable absorber in the system. This inhomogeneity provides an explanation of the origin of the phenomenological parameters used in the semiclassical master equation.

5.4 Saturable absorber

Inhomogeneity is incorporated in the quantum model of the laser by including a saturable absorber. As illustrated in Fig. 5.7, this is achieved by introducing N_a saturable absorber material elements, each coupled to the photon field by a coupling constant g' and decay rate γ'. This material is not incoherently pumped and it absorbs photons created in the cavity by emitters. Once saturated, the system may lase. The Hamiltonian is

$$\begin{aligned} H_S = \omega a^\dagger a \quad &+ \quad \sum_{k=1}^{N_e} \omega \left|2_k\right\rangle \left\langle 2_k\right| + g(\sigma_k a^\dagger + a {\sigma_k}^\dagger) \\ &+ \quad \sum_{k'=1}^{N_a} \omega \left|2_{k'}\right\rangle \left\langle 2_{k'}\right| + g'(\sigma_{k'} a^\dagger + a {\sigma_{k'}}^\dagger) \end{aligned} \tag{5.4.1}$$

Including the interaction with reservoirs, the master equation is

$$\frac{d\rho}{dt} = \frac{i}{\hbar}[\rho, H_S] + \frac{\kappa}{2}(2a\rho a^\dagger - a^\dagger a\rho - \rho a^\dagger a) + \sum_{k=1}^{N_e} \frac{\gamma_k}{2}(2\sigma_k \rho {\sigma_k}^\dagger - {\sigma_k}^\dagger \sigma_k \rho - \rho {\sigma_k}^\dagger \sigma_k)$$
$$+ \sum_{k=1}^{N_e} \frac{P_k}{2}(2{\sigma_k}^\dagger \rho \sigma_k - \sigma_k {\sigma_k}^\dagger \rho - \rho \sigma_k {\sigma_k}^\dagger) + \sum_{k'=1}^{N_a} \frac{\gamma'_{k'}}{2}(2\sigma_{k'} \rho {\sigma_{k'}}^\dagger - {\sigma_{k'}}^\dagger \sigma_{k'} \rho - \rho {\sigma_{k'}}^\dagger \sigma_{k'}) \tag{5.4.2}$$

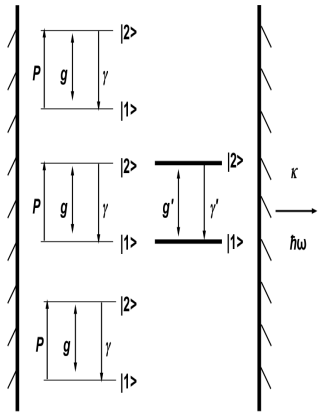

Figure 5.7: System of multiple emitters coupled to a single optical cavity mode in the presence of a saturable absorber. Illustration is for $N_e = 3$ and $N_a = 1$. It is assumed $g < g'$ and $\gamma < \gamma'$.

As shown in Figs. 5.8 and 5.9, with appropriate choice of parameters, results of the quantum model are similar to the predictions of semiclassical master equations. A linear scale is chosen in Fig. 5.8 for easy comparison with our previous results in Ref [34, 35]. The horizontal scale is limited to values of pump less than the onset of self-quenching. The behavior of a meso-laser with a saturable absorber for pump rates that include self-quenching is shown in Fig. 5.9.

Figs. 5.8 and 5.9 show bi-modal photon distributions (Fig. 5.8(g)) and excited state depinning around threshold (Figs. 5.8(b) and 5.9(b)). Emitter inversion (or excitation) de-pins around the lasing threshold to produce the extra photons required to saturate the absorber before the system can start lasing continuously at which point the excitation gets pinned. Photon distribution near the depinned region is bi-modal with a strong peak at zero photon number indicating strong switching (or blinking) between the lasing and zero photon states of the system.

The Fano-factor shows a peak around the onset of lasing (Figs. 5.8(c) and 5.9(c)) and the linewidth reduces with increasing photon number (Figs. 5.8(d) and 5.9(d)) both of which are signatures of threshold behavior. With further increase of pump the system enters its self-quenching behavior and the number of photons in the cavity reduces, the absorber loses its inversion and the lasing emitters are pinned at the saturation value. The probability distributions in Fig. 5.8(g) from the quantum model shows that the peak at $s = 0$ reduces as the pump is increased. It reaches its smallest value at a pump rate near the linear region of lasing after which it again starts increasing because of the onset of quenching. The semiclassical behavior however, loses this peak (at $s = 0$) and a single peaked distribution remains and the system does not quench. The normalized second-order correlation $G^2(\tau = 0)$ increases in this region of bi-modal distribution before it reaches a value of 1, showing a Poisson distribution as the system starts lasing.

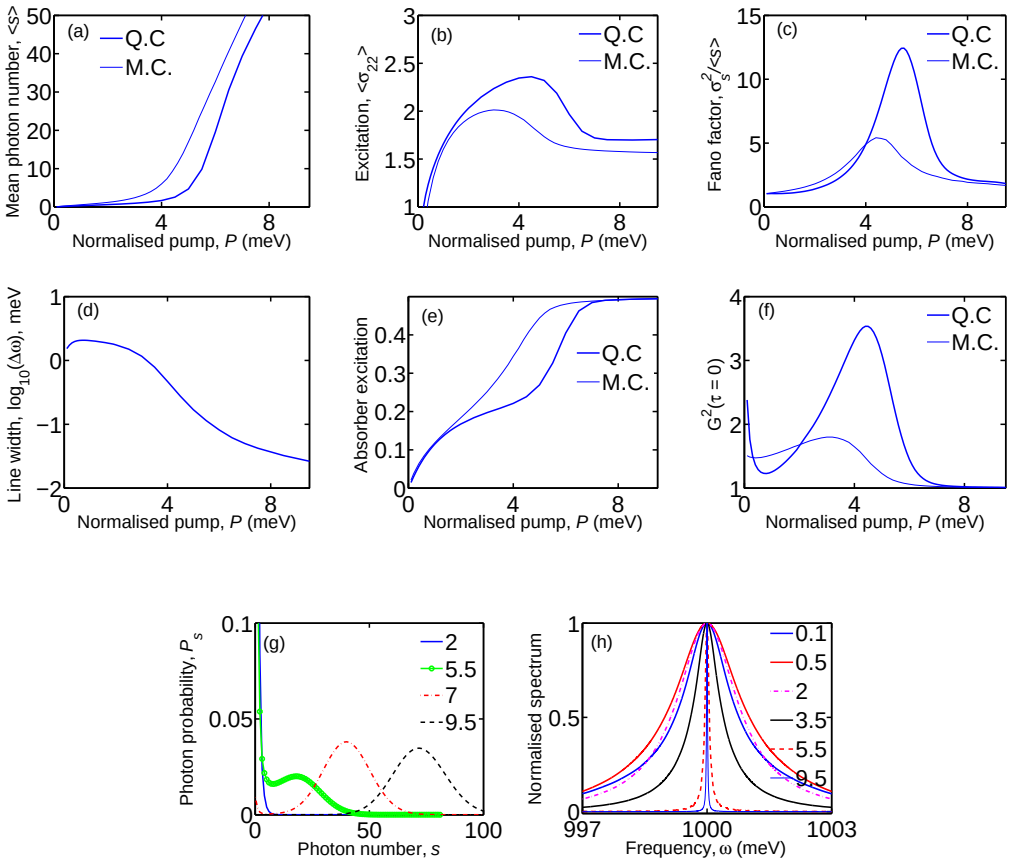

Figure 5.8: Steady-state properties of emitter-photon system in presence of a saturable absorber. Semiclassical master equation calculations (thin lines) and the full quantum theory calculations (thick lines). (a) Mean photon number in lasing mode. (b) Net excitation of emitters. (c) Fano-factor. (d) Spectral line width. (e) Excitation of absorbing element. (f) Second-order coherence at zero delay, $G^2(\tau = 0)$. (g) Probability distributions across threshold from full quantum theory. (h) Spectrum at different normalized pump rates (meV). Emitter elements $N_e = 3$, absorbing element $N_a = 1$. Parameters: $g = 1$ meV, $\gamma = 0.1$ meV, $\omega = 1000$ meV, $\kappa = 0.1$ meV, $g' = 4 \times g$, $\gamma' = 100 \times \gamma$.

With increase in photon number the spectral linewidth shown in Fig. 5.8 (d) initially *increases* before it starts decreasing. This is due to the presence of the absorber. Experiments with semiconductor quantum wire and quantum dot lasers whose active region is likely inhomogeneous also show an increase in spectral linewidth before a decrease with increasing pump around threshold [28, 40]. At values of pump rate sufficiently

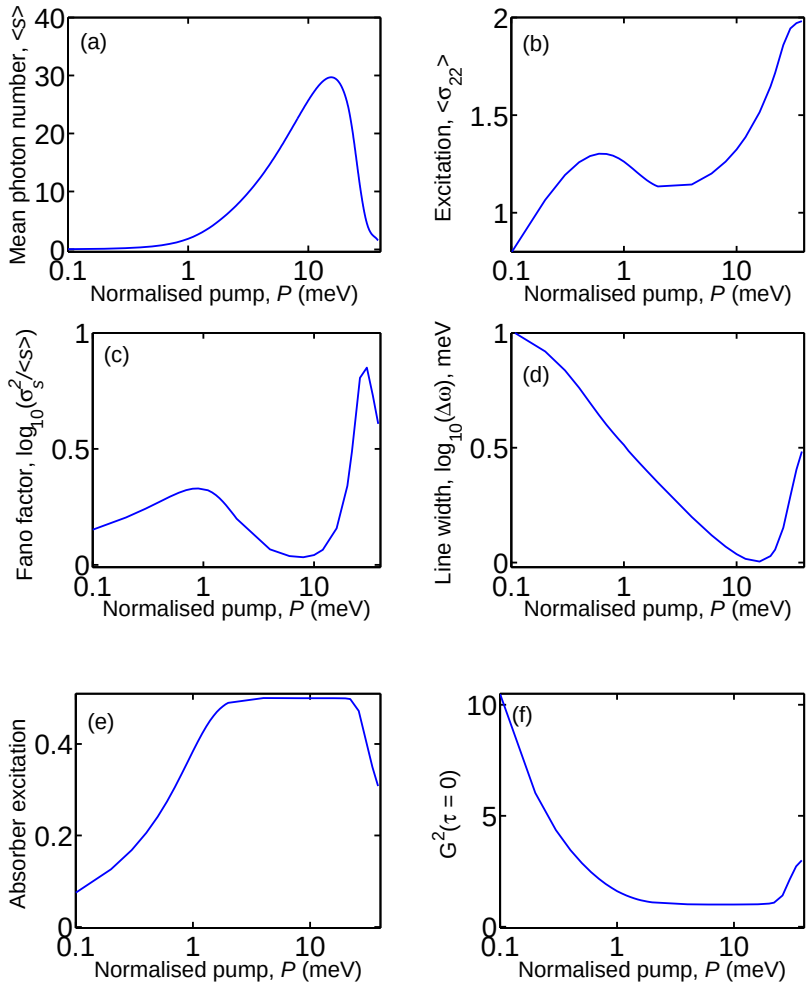

Figure 5.9: Steady-state properties of two-emitter system in presence of a saturable absorber. (b) Net excitation of emitters. (c) Fano-factor. Laser threshold corresponds to broad peak near $P = 1$ meV and self-quenching corresponds to the peak near $P = 20$ meV. (d) Line-width. (e) Excitation of absorbing element. (f) Second-order coherence at zero delay, $G^2(\tau = 0)$. The pump axis is in $\log_{10}$ scale. Number of emitter elements $N_e = 2$ and number of absorbing elements $N_a = 1$. Parameters: $g = 1$ meV, $\gamma = 0.1$ meV, $\omega = 1000$ meV, $\kappa = 0.25$ meV, $g' = 4 \times g$, $\gamma' = 4 \times \gamma$.

large that the system quenches calculations show that the linewidth is greater than that of the empty cavity. This occurs because absorber occupation is no longer inverted.

Figure 5.10 shows linewidth behavior with increasing pump rate below and near threshold for different absorber coupling strength, g'. The case with the smallest coupling $g' = 1$ behaves similar to a conventional laser. Figure 5.10(d) shows that increasing g' produces a greater broadening of linewidth or enhanced phase fluctuations in the region below threshold. The photon probability distributions are not bi-modal in this region. However, at greater pump rates large values of g' create bi-modal distributions and excitation-depinning. This gives rise to a region of enhanced phase fluctuations and hence increased linewidth before, with increased pump rate, experiencing enhanced amplitude fluctuations quantified by the Fano-factor around threshold. Decreasing the value of γ' reduces the range of pump values over which linewidth increases.

Previous studies of lasers incorporating a saturable absorber, such as [Ref. [52, 53, 54]], make use of the large particle number approximation and/or adiabatic elimination. This previous work contains some features common to our results including lasing suppression and bimodal photon distribution near threshold. However, the previous work has no results for meso-scale laser excitation depinning or meso-scale laser spectral line width, and is unable to predict quenching due to quantum decoherence.

Finally random walk calculations can be performed on larger systems, which show the novel features predicted by our quantum model. The time trajectories clearly show the existence of bistable behavior around the threshold region. The enhancement of spontaneous emission with carrier de-pinning is also observed. The effect gets enhanced for stronger absorber coupling g'.

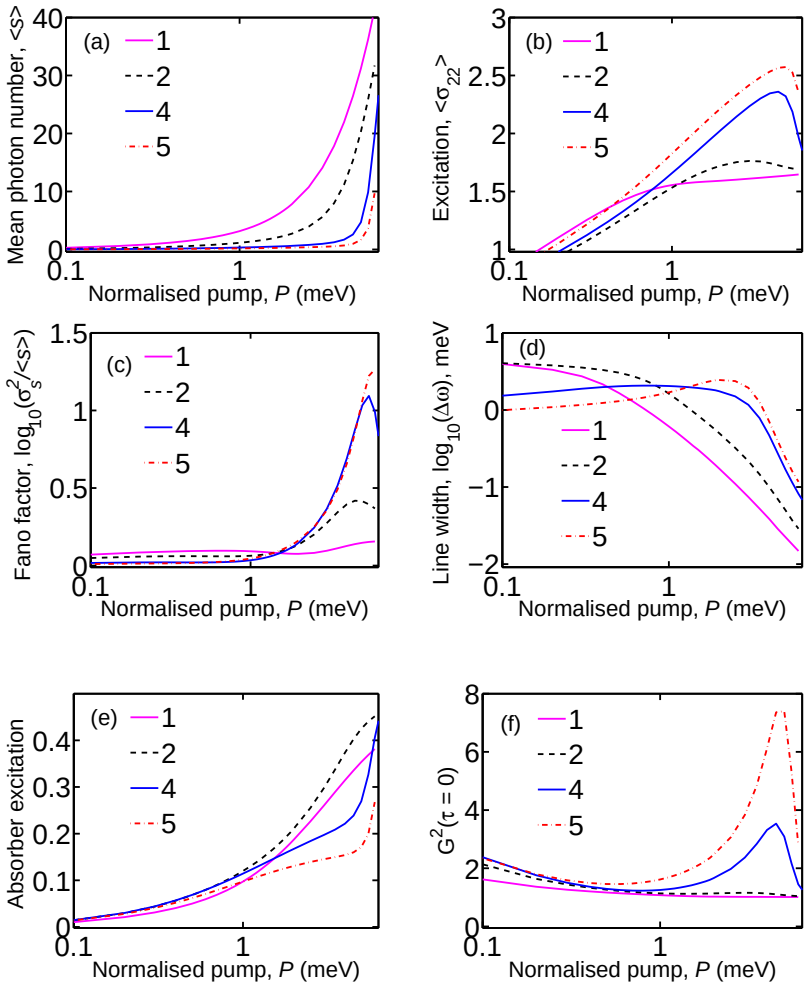

Figure 5.10: Comparison of steady-state properties of emitter-photon system in presence of a saturable absorber for indicated absorber coupling g' in meV. Normalized pump power shown from low vales up to values around threshold. (a) Mean photon number in the lasing mode. (b) Net excitation of emitters. (c) Fano-factor. (d) Spectral line width. (e) Excitation of absorbing element. (f) Second-order coherence at zero delay, $G^2(\tau = 0)$. Number of emitter elements $N_e = 3$ and number of absorbing elements $N_a = 1$. Parameters: $g = 1$ meV, $\gamma = 0.1$ meV, $\omega = 1000$ meV, $\kappa = 0.05$ meV, $\gamma' = 100 \times \gamma$. The curves correspond to different magnitudes of the absorber coupling g'.

5.5 Non-classical light

As described in Ref. [30], low pumping and high cavity losses leads to non-classical states of light. The second-order correlation, $G^2(\tau = 0)$ at zero delay is used to identify

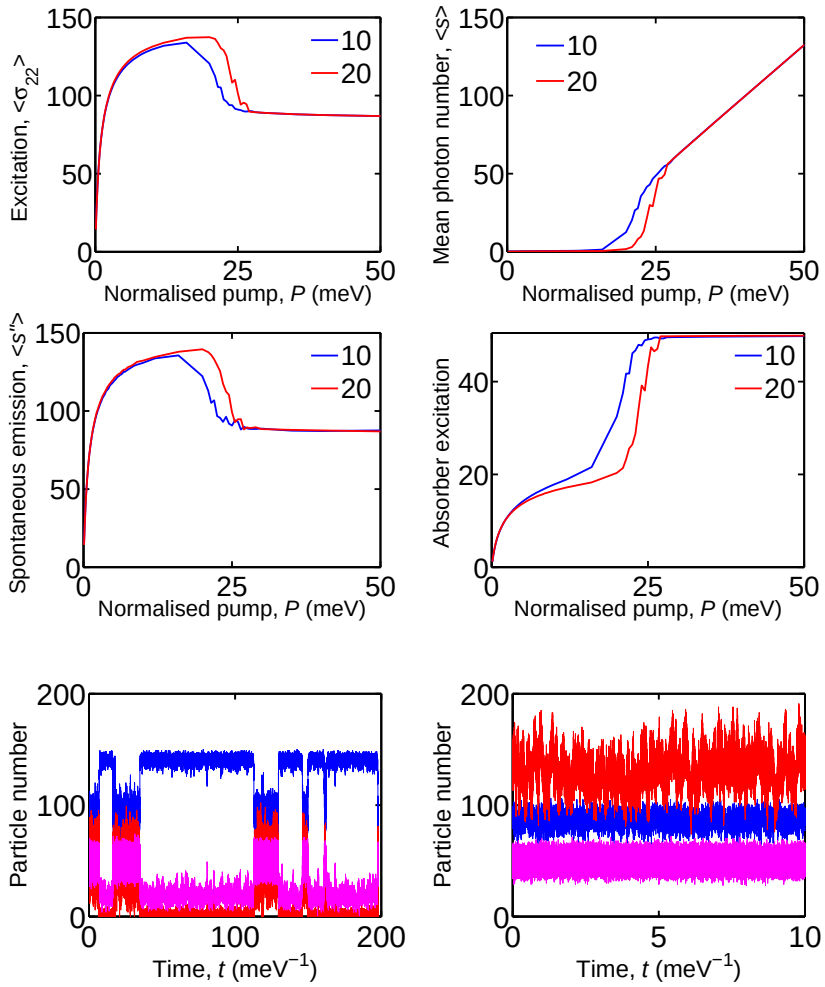

Figure 5.11: Behavior of large systems in presence of saturable absorbers (a) Net excitation of emitters versus pump. (b) Mean photon number versus pump. (c) Spontaneous emission versus pump. (d) Net excitation of absorbers versus pump. (e) Random walk trajectory around threshold (P = 24 meV). (f) Random walk trajectroy at lasing (P = 50 meV). (red (photons), blue (electrons), magenta (absorbers). Number of emitter elements $N_e = 150$ and number of absorbing elements $N_a = 100$. Parameters: $g = 1\,\text{meV}$, $\gamma = 0.1\,\text{meV}$, $\omega = 1000\,\text{meV}$, $\kappa = 20\,\text{meV}$, $g' = 10\times g$ $(blue)$, $g' = 20\times g$ (red), $\gamma' = 4\times\gamma$.

non-classical states. Figure 5.12 plots the variation of normalized second order correlation, $G^2(\tau)$ at $(\tau > 0)$ for 1, 2 and 3 emitters for high values of photon damping and low pumps using Eq.(5.2.16). The one atom case shows non-classical behavior as predicted because, $G^2(\tau = 0)$ is less than 1. The time variation also violates Schwartz's

inequality, $G^2(\tau) > \mathrm{G}^2(\tau = 0)$ [Ref. [15]] and is a signature of anti-bunched behavior. Increasing the number of emitters however removes this non-classical behavior. For multiple emitters the correlation values at zero delay, identifies them as light sources of thermal behavior, and the time variation identifies bunched behavior of classical sources [Ref. [31, 32, 50, 51]].

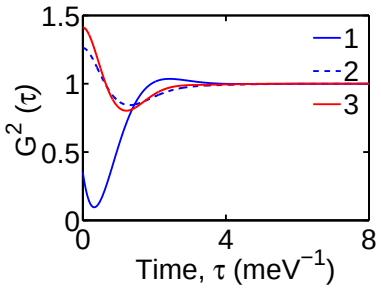

Figure 5.12: Time evolution of normalized second order correlation $G^2(\tau)$ for the indicated number of emitters in the cavity. Parameters: $g = 1$ meV, $\gamma = 0.1$ meV, $\omega = 1000$ meV, $\kappa = 2.5$ meV, Normalised pump, $P = 0.5$ meV.

5.6 Conclusion

The fundamental contribution of field quantization to noise and fluctuations in meso-scale lasers that include inhomogeneity in the form of a saturable absorber has been investigated theoretically. Quantum fluctuations in this finite-sized dissipative system can influence spectral emission line width, suppress lasing, increase particle number fluctuations, and enhance spontaneous emission near threshold. We have presented the first numerical simulations of static and dynamic properties of meso-scale semiconductor lasers using a quantum model with no special approximations (such as weak coupling between the field and reservoir or a single atom emitter approximation). We have applied this model to an inhomogeneous meso-scale laser containing N emitters and a saturable

absorber and demonstrated existence of carrier (excitation) depinning which has previously either been ignored or adiabatically eliminated. Our results provide an interpretation of empirically determined values of β used in semi-classical meso-scale laser models [Ref. [49]] as being due to the presence of an inhomogeneous medium and we have successfully established the connection between the semi-classical [Ref. [34, 35]] and full quantum description of meso-scale lasers. Our work also provides insight into the role of phase and particle number fluctuations in determining the experimentally observed spectral and particle correlation behavior of small lasers [40, 28, 29].

Future work might explore the impact of quantum fluctuations in determining the temperature sensitivity of very small lasers and compare with its known role in determining temperature dependence of conventional laser diodes [Ref. [55, 56, 57]].

Chapter 6

Conclusions

6.1 Conclusions

This chapter summarizes significant contributions of this work and discusses possible directions for future research.

In this thesis we have investigated various aspects of different laser theories and modified them to explain the behavior of meso-scale lasers. Lasing is just one aspect of the more general problem of radiation interacting with matter. Other aspects include bistability, resonance florescence, etc. The general Hamiltonian of matter interacting with an electromagnetic field is treated under various approximations which leads to theories ranging from semi-classical to fully quantum mechanical. In this work we have mostly focused on the lasing problem keeping the broader picture in mind. Just setting up the Hamiltonian or deriving the governing equations is not sufficient. Various approximations are required to solve these equations. The approximations made from physical intuition about large systems leads to meaningful solutions to the problem in most cases. The other limit of a single atom is also completely solvable. It is the intermediate regime of few atoms and few photons that we are set out to address in this work. General analytical theories developed to address this meso-regime is constrained by approximations. In order to avoid this, we have chosen methods of numerical computation to solve the problem. This thesis summarizes the previous work and discusses new results for the meso-scale, such that a comparison can be made between the two. The key contributions of this work are the following:

1. To address lasing in meso-scale systems we have developed a probabilistic theory based on semi-classical master equations which quantizes particle number. This is required to go beyond continnum mean-field calculations and describe systems strongly influenced by fluctuations and correlations. Three different techniques are used to solve the master equation. One is numerical integration using an $Euler$ or $RK4$ method, which gives information about time evolution. The steady-state solution to this problem may be obtained by a matrix inversion technique. Both of these approaches involve solutions to coupled first-order differential equations and is numerically cumbersome. Thus a different method based on a random walk approach is developed to extend calculation to larger systems. Agreement between solutions obtained by the different techniques is shown for the meso-scale case.

2. Results of calculations using the semi-classical master equations are compared with continnum mean-field theories and the differences are explained as being due to the presence of strong fluctuations and correlations incorporated into the more general theory. Certain values of the parameter β lead to novel predictions of lasing suppression, carrier de-pinning and bi-modal probability distributions in meso-scale systems around threshold as compared to the standard phase-transition behavior shown by a bulk laser. The de-pinning of carriers is directly related to enhancement of spontaneous emission in non-lasing modes shown by including another mode for spontaneous emission.

3. Calculation of expectation values in the time-domain show relative slowing as compared to mean-field predictions and is explained by the influence of particle correlations. The data from the random-walk trajectories show strong bi-stable behavior around threshold as the system switches between a lasing and a non-lasing state. Above threshold these trajectories look similar to the ones obtained from mean-field rate equations by adding random Gaussian noise. The RIN or frequency domain response predicted by these two theories are compared and agreement is obtained at higher frequencies.

The agreement can be explained as due to the same choice of rates as we go from rate equations to the semi-classical master equations.

4. The semi-classical theory quantizes energy and has a ground-state for the system ($n = s = 0$). The theory is an improvement from the continuum mean-field theories in the sense that it can account for fluctuations through probabilities. However the line-width information due to phase fluctuation of the light field is missing. Phase of the light field is an important quantity and is the order parameter for lasing light emission. Thus, to verify the predictions of the semi-classical theory and to account for phase behavior a full quantum mechanical theory of N emitters and s photons is required. The basic starting point is the Jaynes-Cummings Hamiltonian with coupling to reservoirs. This is the standard approach for conventional quantum statistical theories of lasers. However, the equations are solved by direct numerical integration without any special approximation on the choice of parameters.

5. Comparison of results with semi-classical master equation theories shows nice agreement around lasing threshold. The standard predictions of laser theories such as threshold and line-width behavior are recovered in the meso-scale case. Predictions of lasing suppression and bi-stable behavior are obtained by inclusion of inhomogeneity in the model in the form of a saturable absorber. This sheds light on our choice of β in the semi-classical theory which was responsible for similar predicted behavior. Semi-classical theories and experiments treat the parameter β as an independent parameter [Ref.[44, 49]]. However, quantum mechanically the choice of β is strongly constrained. Thus, small values of β in a meso-scale system correspond to an inhomogeneous quantum system containing a saturable absorber. In contrast with the treatments of bulk systems with saturable absorbers where the emitter excitation information is eliminated by an adiabatic approximation, our quantum theory accounts for particle excitation directly

and shows emitter de-pinning around threshold. Semi-classical random walk calculations show strong switching behavior around threshold and enhancement of net spontaneous emission in non-lasing modes. Line-width enhancement below threshold is also predicted in inhomogeneous meso-scale laser systems. This is in direct contrast with bulk inhomogeneous calculation which shows only line-width narrowing with increase of cavity photons.

6. Calculations of non-classical effects such as sub-Poisson behavior and antibunching of the light field is performed in the presence of multiple atoms using the second-order correlation function, $G^2(\tau)$. Addition of emitters removes the non-classical effects seen in the case of a single emitter.

6.2 Future directions

The semi-classical model may be used to describe meso-scale systems when the phase-information is not important. However, the quantum model is more complete in this sense. The only approximations are the rotating wave approximation - which conserves energy, Markovian approximation - which is valid for systems in contact with large reservoirs, dipole approximation - which assumes the field is constant over the emitter and independent emitter. The dipole approximation can be modified in the multi-emitter case by choosing different coupling constants for each emitter, thus accounting for spatial inhomogeneity. This is a possible degree of freedom and is utilized in our saturable absorber model. Other than that, the computational technique allows independent control over all parameters influencing each emitter. The influence of these parameters in homogenous multi-emitter system is similar to the one emitter case. However the independent choice of parameters in an inhomogeneous system can be utilized in searching for systems exhibiting non-classical phenomena. The model may be modified to study

the effects of decoherence of the emitter levels. More complicated systems of multi-level emitters (> 2) and multi-mode field can be studied by extending the current formalism. Finite temperature effects can be investigated by using finite temperature reservoirs.

Our current work involves utilizing this quantum model to study an optical link consisting of an emitter, light guide and an absorbing detector. This is the ultimate microscopic limit of an analog optical link. The work is to focus on studying noise properties of these systems. Another technique using feedback could be utilized in modifying the phase and intensity correlation behavior of single mode light fields. This is analogous to the homodyne detection schemes used in recovering phase-modulated signals. The classically equivalent problem may be solved using scalar light fields. But the quantum case involving quantum fields with few photons poses a challenge because of statistical averaging using density matrix. One might also investigate the effect of feedback on a quantum field and try to control it to produce non-classical behavior.

Also the techniques employed involve time-evolution to steady-state. Thus, temporal data for this problem is available and can be controlled to produce non-classical behavior, such as anti-bunching, by time-varying different parameters of the model [Ref. [31]].

Bibliography

[1] J. P. Gordon, H. J. Zieger and C. H. Townes, Phys. Rev. **95**, 282 (1954).

[2] A. L. Schawlow and C. H. Townes, Phys Rev. **112**, 1940 (1958).

[3] T. H. Maiman, *Nature* **187**, 493 (1960).

[4] A. Javan, W. R. Bennet Jr. and D. R. Herriot, Phys. Rev. Lett. **6**, 106 (1961).

[5] E. Purcell, Phys. Rev. **69**, 681 (1946).

[6] K. Drexhage in Progress in Optics, edited by E. Wolf (North Holland, Amsterdam,1974), Vol. XII, pp. 163-232.

[7] S. L. McCall, A. F. J. Levi, R. E. Slusher, S. J. Pearton, and R. A. Logan, Appl. Phys. Lett **60**, 289 (1992).

[8] D. Meschede, H. Walther, and G. Müller, Phys. Rev. Lett. **54**, 551, 1985

[9] K. An, J.J. Childs, R.R. Dasari, and M.S. Feld, Phys. Rev. Lett. **73**, 3375, 1994

[10] W. E. Lamb, Jr. Phys. Rev. **134**, A1429 (1964)

[11] M. Lax, in *Physics of Quantum Electronics*, ed. P. L. Kelley, B. Lax and P. E. Tannenwald (McGraw Hill, New York 1966), p. 735

[12] H. Haken, Handbuch der Physik,Vol. XXV/2c, ed. L. Genzel, Springer: Berlin, 1970.

[13] M. O. Scully, W. E. Lamb, Phys. Rev. Lett. **16**, 853 (1966).

[14] M. O. Scully, W. E. Lamb, Phys. Rev. **159**, 208 (1967).

[15] M. O. Scully and M. Suhail Zubairy, *Quantum Optics.* Cambridge University Press (1997).

[16] H. J. Carmichael, in Lasers and Quantum Optics, Proceedings of the International School on Lasers and Quantum Optics, Mar del Plata, Argentina, 22-31 August, 1988 (World Scientific, Singapore, 1990), pp. 52-85.

[17] M. Elk, Phys. Rev. A **54**, 4351 (1996).

[18] A. M. Smith and C. W. Gardiner, Phys. Rev. A **38**, 4073 (1988).

[19] R Hall, G. E. Fenner, J Kingsley, T. J. Soltys and R. O. Carlson, Phys. Rev. Lett. **9**, 366 (1962).

[20] H. Soda, K. Iga, C. Kitahara, Y. Suematsu, Jap. J. Appl. Phys., **18** 2329 (1977).

[21] G. Bjork and Y. Yamamoto, IEEE J. Quantum Electron. **72**, 2386 (1991).

[22] H. Yokoyama and S. D. Bronson, J. Appl. Phys. **66**, 4801 (1989).

[23] F. De Martini, F. Cairo, P Mataloni, and F. Verzegnassi, Phys. Rev. A **46**, 4220 (1992)

[24] A. F. J. Levi, *Applied Quantum Mechanics.* Cambridge University Press (2003).

[25] A. F. J. Levi, S. L. McCall, S. J. Pearton, and R. A. Logan, Electron. Lett. **29**, 1666 (1993).

[26] G. W. Gardiner, *Handbook of Stochastic methods.* Springer-Verlag, Berlin (1983).

[27] W. H. Louisell, *Quantum Statistical Properties of Radiation.* Wiley, New York (1973).

[28] M. Nomura, N. Kumagai, S. Iwamoto, Y. Ota, and Y. Arakawa, Nature Phys. Lett. **6**, 279 (2010).

[29] F. Dubin, C. Russo, H. G. Barros, A. Stute, C. Becher, P. O. Schmidt, and R. Blatt, Nature Phys. Lett. **6**, 350 (2010).

[30] J. I. Perea, D. Porras, and C. Tejedor, Phys. Rev. B **70**, 115304 (2004).

[31] Oliver Benson and Yoshihisa Yamamoto, Phys. Rev. A **59**, 4756 (1999).

[32] Yi Mu and C. M. Savage, Phys. Rev. A **46**, 5944 (1992).

[33] G. M. D'Ariano, N. Sterpi, and A. Zucchetti, Phys. Rev. Lett. **74**, 900 (1995).

[34] K. Roy-Choudhury, S. Haas, and A. F. J. Levi, Phys. Rev. Lett. **102**, 053902 (2009).

[35] K. Roy-Choudhury and A. F. J. Levi, Phys. Rev. A **81**, 13827 (2010).

[36] P. R. Rice and H. J. Carmichael, Phys. Rev. A, **50**, 4318 (1994).

[37] M. Ahmed, M. Yamada, and M. Saito IEEE Journal of Quantum Electronics **37**, 1600 (2001).

[38] L. Florescu and S. John, Phys. Rev. E **69**, 046603 (2004).

[39] R. Jin, D. Boggavarapu, M. Sargent, P. Meystre, H.M. Gibbs, and G. Khitrova, Phys. Rev. A **49**, 4038 (1994).

[40] K. Atlasov, M. Calic, F. Karlsson, P. Gallo, A. Rudra, B. Dwir, and E. Kapon, Optics Express **17**, 18178 (2009).

[41] H. Kim, M. T. Rakher, D. Bouwmeester, and P. M. Petroff, Appl. Phys. Lett. **94**, 131104 (2009).

[42] S. Reitzenstein, C. Boeckler, A. Bazhenov, A. Gorbunov, S. Muench, A. Loeffler, M. Kamp, V. D. Kulakovskii, and A. Forchel, Physica Status Solidi (b)**246**, 277 (2009).

[43] S. Reitzenstein, T. Heindel, C. Kistner, A. Rahimi-Iman, C. Schneider and A. Forchel, Appl. Phys. Lett. **93**, 061104 (2008).

[44] W. W. Chow and S. W. Koch, *Semiconductor - Laser Fundamentals.* Springer-Verlag, Berlin, Heidelberg, New York (1999).

[45] H. S. Ashour, M. Sokol, L. M. Pedrotti, P. R. Rice, J. Opt. Soc. Am. B **24**, 8 (2007).

[46] C. W. Gardiner and A. Eschmann, Phys. Rev. A **51**, 4982 (1995).

[47] H. Haug and H. Haken, Z. Phys. **204**, 262 (1967), H. Haug, Z. Phys. **200**, 57 (1967), H. Haug, Z. Phys. **206**, 163 (1967),

[48] H. Haug, Phys. Rev. **184**, 338 (1969).

[49] M. T. Hill, et al., Lasing in metallic-coated nanocavities, *Nature Photonics* **1**, 589-594 (2007).

[50] Y. M. Golubev and I. V. Sokolov, Zh. Eksp. Teor. Fiz. **87**, 408 (1984) [Sov. Phys.-JETP **60**, 234 (1984)].

[51] H. Ritsch, P. Zoller, C. W. Gardiner and D. F. Walls, Phys. Rev. A **44**, 3361 (1991).

[52] R. Roy, Phys. Rev. A **20**, 2093 (1979)

[53] L. A. Lugiato, P. Mandel, S. T. Dembinski and A. Kossakowski, Phys Rev A **18**, 238 (1978)

[54] R. B. Schaefer and C.R. Willis, Phys. Rev. A **13**, 1874 (1976)

[55] J. O'Gorman, A. F. J. Levi, S. Schmitt-Rink, T. Tanbun-Ek, D. L. Coblentz, and R. A. Logan, Appl. Phys. Lett. **60**, 157 (1992).

[56] J. O'Gorman, S. L. Chuang, and A. F. J. Levi, Appl. Phys. Lett. **62**, 1454 (1993).

[57] S. L. Chuang, J. O'Gorman, and A. F. J. Levi, IEEE J. Quantum Electron. **29**, 1631 (1993).

Appendix A

Evaluation of multi-time correlation functions

The technique for calculating multi-time correlation function for Markovian systems is reviewed following the work of C. W. Gardiner [Ref.[26]]. Calculation of line-width (field-field), intensity-intensity correlation require statistical averages of two-time correlation functions of light field operators. In general the correlation function is of the form

$$\langle A(t+\tau)B(t)\rangle = Tr_{\rm S}[Tr_{\rm R}[A(t+\tau)B(t)\rho_S \otimes \rho_R]] \tag{A.0.1}$$

The system operators A and B are evaluated in the Heisenberg picture. Showing explicit time dependence Eq.(A.0.1) can be written as,

$$\langle A(t+\tau)B(t)\rangle = Tr_{\rm S}[Tr_{\rm R}[e^{iH(t+\tau)/\hbar}Ae^{-iH(t+\tau)/\hbar}e^{iHt/\hbar}Be^{-iHt/\hbar}\rho_S \otimes \rho_R]] \tag{A.0.2}$$

The equation includes reservoir variables and we would prefer to express this in terms of system variables only. This is done by writing Eq.(A.0.2) as,

$$\langle A(t+\tau)B(t)\rangle = Tr_{\rm S}[ATr_{\rm R}[e^{-iH\tau/\hbar}B\rho_{total}(t)e^{iH\tau/\hbar}]] \tag{A.0.3}$$

A is unaffected by the trace operation over reservoir variables and we have used the cyclic property of trace in the derivation. The equation of motion for a term

$$X(\tau,t) = e^{-iH\tau/\hbar} B\rho_{total}(t) e^{iH\tau/\hbar} \tag{A.0.4}$$

in terms of τ is

$$i\hbar \frac{\partial X(\tau,t)}{\partial \tau} = [H, X(\tau,t)] \tag{A.0.5}$$

Following the derivation of master equations for system density matrix ρ_S, it can be shown that $Tr_R[X(\tau,t)]$ also obeys the Master equation (Eq.(5.2.5)) as a function of τ. The time evolution operator $\hat{\mathbf{L}}$ for the master equations can now be used to write,

$$\begin{aligned} Tr_{\mathrm{R}}[X(\tau,t)] &= \hat{\mathbf{L}}(t+\tau,t) Tr_{\mathrm{R}}[X(0,t)] \\ &= \hat{\mathbf{L}}(t+\tau,t)[B\rho_S(t)] \end{aligned} \tag{A.0.6}$$

where in this case $\rho(t)$ is in the Schrödinger picture. The final form of the correlation function is given by,

$$\langle A(t+\tau)B(t)\rangle = Tr_{\mathrm{S}}[A\hat{\mathbf{L}}(t+\tau,t)[B\rho_S(t)]] \tag{A.0.7}$$

The evolution operator acts on everything to its right. As we use the evolution operator in the interaction picture an additional time dependence due to the free Hamiltonian of the system should be included. In the case of resonance, this adds an extra time dependence of $e^{-i\omega\tau}$ in the field-field correlation as the two operators $a(t)$ and $a^\dagger(t+\tau)$ are seperated in time by amount τ. ω is the frequency of the field. However in the intensity-intensity correlation, this dependence cancels out, as in this case we have the

product of operator $a\rho a^{\dagger}$ and time dependent terms from a and $a^{\dagger}$ cancel due to opposite signs.

The formula for calculation of multi-time correlation of this type is given by [Ref. [26]]

$$\langle A_0(s_0)A_1(s_1).....A_m(s_m)B_n(t_n)B_{n-1}(t_{n-1}.....B(t_0)\rangle = \\ Tr_{\rm S}[f_r\hat{\mathbf{L}}(\tau_r,\tau_{r-1})f_{r-1}\hat{\mathbf{L}}(\tau_{r-1},\tau_{r-2}).....\hat{\mathbf{L}}(\tau_1,\tau_0)f_0\rho(t_0)] \tag{A.0.8}$$

where $f_i\rho = F_i\rho$ if F_i is one of the $B's$ and $f_i\rho = \rho F_i$ if F_i is one of the $A's$, and

$$\tau_0 < \tau_1 < \tau_2 < ..... < \tau_r \tag{A.0.9}$$

Here ρ is the density matrix of the system (emitter-field).

Appendix B

Runge-Kutta method

The RK4 treatment is reviewed following the treatment in [Ref.[24]]. Most of the problems studied in this work require solution of coupled first order differential equations of the form

$$\frac{d}{dt}y_j(t) = f_j(t, y_1, y_2, ...y_N) \tag{B.0.1}$$

where j runs from 1 to N. The equations are time-evolved by numerical integration from a given initial condition. The formula for time evolution using single step Euler method is,

$$y_{n+1} = y_n + h_0 f(t_n, y_n) + O(h_0^2) \tag{B.0.2}$$

where h_0 is a single step. The derivative information $f(t, y)$ at the begining of the interval is used to make an estimate of the solution. The error $O(h_0^2)$ made in each step is only one power of h_0 smaller than the net change $h_0 f(t_n, y_n)$.

A better estimate of the derivative can reduce this error. This is done by estimating the derivative at different points in the interval. The method becomes accurate if the final estimate of the derivative, $f(t, y)$ leads to cancellation of first order and some higher order terms. This is achieved using the fourth order Runge-Kutta method which makes

four estimates of the dervative for each step. The time evolution formula using fourth order RK4 method is

$$y_{n+1} = y_n + \frac{k_1}{6} + \frac{k_2}{3} + \frac{k_3}{3} + \frac{k_4}{6} + O(h_0^5) \tag{B.0.3}$$

where

$$k_1 = h_0 f(t_n, y_n) \tag{B.0.4}$$

is used to make an estimate of the change using derivative at the first point.

$$k_2 = h_0 f(t_n + \frac{h_0}{2}, y_n + \frac{k_1}{2}) \tag{B.0.5}$$

is used to make an estimate of the change using the derivative at midpoint determined by k_1/2 and h_0/2.

$$k_3 = h_0 f(t_n + \frac{h_0}{2}, y_n + \frac{k_2}{2}) \tag{B.0.6}$$

is used to make a better estimate of the derivative at midpoint using k_2/2 and h_0/2.

$$k_4 = h_0 f(t_n + h_0, y_n + k_3) \tag{B.0.7}$$

is used to evaluate the derivative information at the end point using k_3.